



Engineered wavefronts for imaging applications: From conventional to metasurface optics.

Engay, Einstom

Publication date:
2021

Document Version
Publisher's PDF, also known as Version of record

[Link back to DTU Orbit](#)

Citation (APA):
Engay, E. (2021). *Engineered wavefronts for imaging applications: From conventional to metasurface optics*. Technical University of Denmark.

General rights

Copyright and moral rights for the publications made accessible in the public portal are retained by the authors and/or other copyright owners and it is a condition of accessing publications that users recognise and abide by the legal requirements associated with these rights.

- Users may download and print one copy of any publication from the public portal for the purpose of private study or research.
- You may not further distribute the material or use it for any profit-making activity or commercial gain
- You may freely distribute the URL identifying the publication in the public portal

If you believe that this document breaches copyright please contact us providing details, and we will remove access to the work immediately and investigate your claim.



Engineered wavefronts for imaging applications: From conventional to metasurface optics

Einstom Engay

A dissertation submitted in partial fulfillment of the requirements
for the degree of Doctor of Philosophy

PhD Supervisors: Assoc. Prof. Andrei Lavrinenko, Senior Researcher Peter John
Rodrigo and Dr. Ada-Ioana Bunea

Department of Photonics Engineering
Technical University of Denmark
Kongens Lyngby, Denmark
31 December 2020

Abstract

Wavefront modulation has found use in many applications including optical manipulation in the micro-regime, optical communications, photolithography and imaging, among others. Traditionally, wavefront engineering is implemented by conventional optical components that are based on refraction or diffraction, as light propagates through these components. With the advent of computing, and micro and nanofabrication technologies, a new class of optical components has started to emerge. Metasurface optics rely on nanoscale light-matter interactions to control the wavefront of an incident light, promising new capabilities that could only be achieved previously with a combination of bulky conventional optics.

This thesis explores imaging applications of engineered wavefronts, modulated using both conventional and metasurface optics. For the first application, a refractive element is employed to construct a common-path interferometer for use in determining the topological charge of beams with orbital angular momentum. Secondly, a commercial optical vortex produced using birefringent liquid crystals is utilized for high-contrast non-linear imaging. Finally, a multifunctional metasurface device is exploited to facilitate single-shot quantitative phase imaging and is applied for wavefront sensing.

Resumé

Modulation af bølgefronter anvendes i flere applikationer, blandt andet optisk manipulation af mikrobølger, optisk kommunikation, fotolitografi og billeddannelse, blandt andre. Traditionelt bliver bølgefronterne formet af konventionelle optiske elementer, ved brydning eller diffraktion af lyset, der passerer gennem elementerne. På baggrund af den teknologiske udvikling, i databehandling og micro- og nanoteknologi, er der dukket en ny type af optiske komponenter op. Metaoverflade optik er baseret på lysstof vekselvirkning i nanoskala, til at kontrollere bølgefronterne af det indfaldende lys. Dette muliggør lysmanipulation, der traditionelt set, ville kræve flere konventionelle voluminøse komponenter.

Denne afhandling udforsker billeddannelsens applikationer af konstruerede bølgefronter, moduleret af konventionel- og metaoverflade optik. I den første applikation, bruges et brydningselement til at konstruere et fællesinterferometer, som bruges til at bestemme den topologiske ladning af lysstråler med orbitalt impulsmoment. I den anden applikation, bruges en kommerciel optisk vortex, frembragt af dobbeltbrydning af flydende krystaller, til at danne højkontrast ikke-lineære billeder. Afslutningsvist bruges en multifunktionel metaoverflade til at muliggøre et enkelt skud kvantitativ fase rekonstruktion, hvilket bruges til måling af bølgefronter.

Acknowledgments

I would like to thank all my supervisors for guiding me throughout my PhD studies. To Prof. Andrei Lavrinenko, for accepting me into the Metamaterials group, for his guidance, and encouragement. To Senior Researcher Peter John Rodrigo, for all the practical suggestions and discussions on experimental techniques. To Dr. Ada-Ioana Bunea, for the fruitful discussions and all the support, on and off university.

I would also like to express my thanks to the people who helped complete this work, in one way or another: Dewang Huo for the full-wave calculations, Radu Malureanu for the metasurface fabrication, Osamu Takayama and Evgeniy Shkondin for the guidance in the metasurface characterization. To the rest of the Metamaterials group: Leonid, Larissa, and Rasmus, for all the stimulating discussions that go beyond our common curiosities about light. To my previous groupmates in the Programmable Phase Optics group, Prof. Jesper Glückstad and Andrew, for introducing me to wavefront engineering and its applications in light robotics, imaging and optical manipulation. To Alex, for all the insights as a colleague and as a friend. Long hours in the lab were endurable with his company and with his great taste in music.

Rarely do we encounter friendships that we truly cherish. For this, my huge thanks to Jadze and Carl.

My biggest thanks to my greatest support - my family. They've let me fly but kept me grounded at the same time.

Lastly, to Anjelou, my inspiration and my joy, who has kept me sane through the years. Thanks for being with me in all of these.

List of Publications

Articles included in the thesis

Published in scientific journals

1. E. Engay and P. J. Rodrigo, “Nonlinear optical vortex coronagraphy,” *Optics Letters*, **45** (6), 2020.
2. E. Engay, A.R. Bañas, A.I. Bunea, S.D. Separa, and J Glückstad, “Interferometric detection of OAM-carrying Helico-conical beams,” *Optics Communications*, **433**, 2019.

Articles in preparation

1. E. Engay, D. Huo, Radu Malureanu, Ada-Ioana Bunea and A. Lavrinenko, “Single-shot quantitative phase imaging assisted by a polarization-dependent all-dielectric metasurface,”.

Other journal publications

1. A-I. Bunea, M. Chouliara, S. Harloff-Helleberg, A.R. Bañas, E. Engay and J. Glückstad, “Optical catapulting of microspheres in mucus models— toward overcoming the mucus bio-barrier,” *Journal of Biomedical Optics*, **24** (3), 2019.
2. A-I. Bunea, M.H. Jakobsen, E. Engay, A.R. Bañas, and J. Glückstad, “Optimization of 3D-printed microstructures for investigating the properties of the mucus biobarrier,” *Micro and Nano Engineering*, **2**, 2019.
3. A.R. Bañas, E. Engay, A.I Bunea, S.D. Separa and J. Glückstad, “Three-dimensional light sculpting using a geometric analysis”, *Optics Communications*, **431**, 2019.
4. E. Engay, A.I Bunea, M. Chouliara, A.R. Bañas and J. Glückstad, “Natural convection induced by an optically fabricated and actuated microtool with a thermoplasmonic disk,” *Optics Letters*, **43**(17), 2018.
5. A.R. Bañas, S.D. Separa, E. Engay and J. Glückstad, “Point spread function shaping using geometric analysis,” *Optics Communications*, **427**, 2018.

Conference proceedings

1. * E. Engay, D. Huo, R. Malureanu, A. Wetzel, A. Bunea, P. J. Rodrigo and A. Lavrinenko, “Single-shot quantitative phase microscopy assisted by an all-dielectric metasurface”, CLEO 2020, FW4Q.3, San Jose, California, USA, (2020) (oral).
2. * A-I. Bunea, E. Engay, Alexandre Wetzel and Rafael Taboryski, “BioBots: 3D-printed microrobots manipulated by light as potential biomedical ‘surgeons’”, CLEO 2020, ATh4K.4, San Jose, California, USA, (2020) (oral).
3. E. Engay, L. Vertchenko, D. Huo, A.Wetzel, A-I. Bunea, and A. Lavrinenko, “Subwavelength transmissive surface-relief gratings for spiral phase-contrast microscopy”, in 45th International conference on Micro and Nano Engineering, Rhodes Island, Greece (2019) (poster).
4. * E. Engay, A.Wetzel, A-I. Bunea, J. Glückstad, “Disk-tip microtools for light robotics”, in 41st Photonics and Electromagnetics Research Symposium, Rome, Italy (2019) (oral).
5. * E. Engay, A-I. Bunea, M. Chouliara, A. R. Bañas and J. Glückstad, “Optically fabricated and controlled microtool as a mobile heat source in microfluidics”, in Proc. SPIE 10804, Advanced Manufacturing Technologies for Micro- and Nanosystems in Security and Defence, Berlin, Germany (2018) (oral).

6. A-I. Bunea, E. Engay, M. Chouliara, A. R. Bañas and J. Glückstad, “Rational design of light-controlled microrobots”, in Proc. SPIE 10804, Advanced Manufacturing Technologies for Micro- and Nanosystems in Security and Defence, Berlin, Germany (2018) (oral).
7. E. Engay, M. Chouliara, A. R. Bañas, S. D. Separa and J. Glückstad, “Light robotics: a new field of research”, in Proc. SPIE 10549, Complex Light and Optical Forces XII (2018).
8. M. Chouliara, E. Engay, A. R. Bañas, S. D. Separa and J. Glückstad, “Cell growth regulation studies on our Biophotonics Work Station”, in Proc. SPIE 10549, Complex Light and Optical Forces XII (2018).

* Attended as presenting author

List of contributions to the works included in the thesis

Chapter 3: I participated in the formulation of the experimental design, performed the analytic and numerical modeling, and acquired and analyzed the data. I wrote the first draft of the manuscript, and did subsequent revisions after several internal reviews, and peer-review.

Chapter 4: I participated in the formulation of the experimental design, performed the analytic and numerical modeling, built the optical setup, and acquired and analyzed the data. I prepared the first draft of the manuscript, and did subsequent revisions after several internal reviews, and peer-review.

Chapter 5: I participated in the formulation of the experimental design, performed the analytic modeling and the FFT-based calculations for imaging simulations, built the optical setups and subsequently characterized the properties and performance of metasurfaces, and acquired and analyzed the data. I prepared the first draft of a manuscript to be submitted for journal publication.

Acronyms

RS: Rayleigh-Sommerfeld

PSF: point spread function

SLM: spatial light modulator

LC: liquid crystal

OAM: orbital angular momentum

HCB: Helico-conical beams

CPI: common-path interferometer

PCF: phase-contrast filter

SRW: synthetic reference wave

OVC: optical vortex coronagraph

VM: vortex mask

n-OVC: nonlinear optical vortex coronagraph

SFG: sum-frequency generation

PPLN: periodically poled lithium niobate

IWA: inner working angle

OV: optical vortex

PTP: peak-to-peak

FDTD: finite-difference time domain

GS: Gerchberg-Saxton

QPI: quantitative phase imaging

TIE: transport-of-intensity equation

MS: metasurface

FFT: fast Fourier transform

C-TIE: conventional transport-of-intensity equation

MS-TIE: metasurface-based transport-of-intensity equation

a-MS-TIE: analytic metasurface-based transport-of-intensity equation

MPPR: multiple-plane phase retrieval

RMSE: root-mean-square error

Contents

Abstract	iii
Acknowledgments	v
List of Publications	vii
Acronyms	xi
List of figures	xv
1 Introduction	1
2 Optical wave diffraction: definitions and some mathematical preliminaries	5
2.1 From Maxwell's equations to scalar wave equation	5
2.2 Fourier optics	7
2.2.1 Analytic Fourier theory	7
2.2.2 Rayleigh-Sommerfeld diffraction formula	9
2.3 A review of beam engineering techniques	12
2.3.1 Conventional optics	12
2.3.2 Metasurface optics	14
2.4 Summary	17
3 Topological charge measurement using a common-path interferometer	19
3.1 Introduction	19
3.2 Helico-conical beams	20
3.3 Common-path interferometer	22
3.4 OAM characterization of optical twisters	26
3.5 Summary	32
4 High-contrast nonlinear imaging using an optical vortex	33
4.1 Introduction	33
4.2 Mathematical model	35
4.3 Laboratory demonstration of a nonlinear optical vortex coronagraph	39
4.3.1 Optical setup	39
4.3.2 Numerical simulation and experimental verification	40
4.3.3 Wavelength tunability and broadband operation	40
4.3.4 n-OVC performance	42
4.4 Summary	46
5 Quantitative phase imaging using a polarization-dependent all-dielectric metasurface	47
5.1 Introduction	47
5.2 All-dielectric metasurfaces	49
5.2.1 Metasurface design and fabrication process	53
5.2.2 Wavefront engineering using metasurfaces	54
5.3 Metaholograms	54
5.4 Polarization beam splitters	57
5.5 Quantitative phase measurement using a polarization-dependent metasurface	62
5.5.1 The transport-of-intensity equation	62
5.5.2 Optical design of the metasurface-based TIE	63
5.5.3 Experimental demonstration of metasurface-based QPI	69
5.6 Summary	77

6	Conclusions	79
	References	81
A	Appendix A: Multiple-plane phase retrieval	89
A.1	Multiple-plane phase retrieval	89

List of Figures

2.1	Scalar wave propagation. Schematic diagram of complex field profile at a source plane being observed at a parallel observation plane, a distance z away.	9
2.2	A $4f$ optical configuration. P1, input plane; P2, Fourier plane; P3, output plane; L1-L2, lenses; f , focal length.	11
2.3	Wavefront engineering mechanisms. Wavefront shaping using (a) refractive element, (b) diffractive element and (c) a metasurface. Image is adapted from [20].	14
3.1	Helico-conical beams phase profiles. Wrapped phase profiles of helico-conical beams for $K = 0, 1$ and $l = 1, 2$, showing the radial and azimuthal dependence of the phase.	21
3.2	Helico-conical beams far-field intensity profiles. Spiral far-field intensities of helico-conical beams with $K = 0$ and $l = 1, 3, 5, 7$ and 9	21
3.3	Common path interferometer for topological charge detection. Schematic diagram of the common-path interferometer built from a $4f$ optical setup. The phase-contrast filter (PCF) introduces θ -phase shift to the low-frequency components of the incident HCB that serve as the synthetic reference wave.	22
3.4	Schematic of the PCF relative to the Airy profile incident on it at the Fourier plane. A, B are transmittance used to adjust the relative strength of the SRW relative to the scattered field. θ is the amount of phase shift introduced to the zero-order, R_1 is the PCF radius and R_2 is the Airy radius. The Airy profile is generated at the Fourier plane by the input circular aperture with $R_2 = 0.61\lambda f/r_0$	23
3.5	SRW spatial profile over the output aperture normalized to the input aperture radius for $\eta = 0.2, 0.4$ and 0.627	25
3.6	Normalized zero-order of HCBs ($K = 0$) for different topological charges obtained from Equation 3.12 and from numerical simulations.	27
3.7	Analytic CPI intensity output for HCBs ($K = 0$) with positive topological charges.	28
3.8	Analytic CPI intensity output for HCBs ($K = 0$) with negative topological charges.	28
3.9	Fringe contrast. Visibility of the interference fringes from the CPI output as the topological charge is increased obtained by calculating the contrast of the CPI output (dashed line) and by plotting the analytic expression (solid line).	29
3.10	Experimental setup for HCB detection. The Gaussian output of a 532-nm diode laser is first expanded and then imprinted with the HCB phase profile using an LCOS-SLM (Hamamatsu). The outgoing beam carries the helico-conical phase and is then incident on the CPI for topological charge detection. The output of the CPI is imaged using a CCD camera. The focal length of the lenses is 100 mm. . .	29
3.11	CPI experimental intensity output. Interference fringes obtained from the CPI for HCBs ($K=0$) with increasing topological charge.	30
3.12	Intensity line profiles. CPI intensity line scans for $l = +10, +15$ and $+20$	30
3.13	Helicity dependence of the CPI output. (Top row) Positively and (bottom row) negatively charged HCBs ($K=0$) acquired experimentally. The sign manifests in the outputs as maximum and minimum when the charge is positive and negative, respectively.	31
3.14	Analytic CPI intensity output for HCBs ($K = 0$) with positive topological charges.	31
4.1	Phase distribution of LG beams for $l = 1$ and $l = 2$.	35

4.2	Nonlinear optical vortex coronagraph. Schematic diagram of (a) a linear OVC and (b) the proposed n-OVC. In the n-OVC, the signal beam (red lines) is mixed with a vortex-shaped pump beam (green lines) in the nonlinear PPLN crystal. With such a process, the coronagraphic and off-axis images are produced at the SFG wavelength (blue lines). The two insets in (b) illustrate the phase match (Δk) dependence on the angular direction ϕ_s of the input signal k -vector. (c, d) Calculated intensity distributions at the respective pupil planes of the two coronagraphs. $L_1 - L_5$, lenses; DM, dichroic mirror; F, spectral filters that only allows SFG beam. . .	37
4.3	Halo intensity outputs. (a, c) Numerical and (b, d) experimental irradiance outputs of the n-OVC at the pupil plane for two signal wavelengths (a, b) $\lambda_s = 1575$ nm and (c, d) $\lambda = 1550$ nm. The blurred images are caused by the finite extent of the PPLN crystal aperture.	41
4.4	Tunability of the signal central wavelength. Phase-match curves showing the $\Lambda - \lambda_s$ combinations for which $\Delta k_z = 0$ can be achieved for (a) $\lambda_p = 1064$ nm and varying T , and for (b) $T = 180$ °C.	42
4.5	Tunability of the n-OVC bandwidth. Normalized upconversion efficiency as a function (a) of both the PPLN period and the signal wavelength, and (b, c) of only the signal wavelength for fixed PPLN periods (b) $\Lambda = 11.8$ μm and (c) $\Lambda = 23.0$ μm . For all plots, $\lambda_p = 1064$ nm, $T = 180$ °C and $L = 2.5$ mm are used.	42
4.6	Rendered experimental on-axis and off-axis coronagraphic images from the n-OVC.	43
4.7	Peak-to-peak attenuation plots of the n-OVC obtained from numerical simulations and experiments.	44
4.8	Azimuthally averaged radial profiles of the output PSF.	45
5.1	Schematic of the metasurface. (a) Unit cell of the metasurface consisting of amorphous silicon (a-Si) on SiO_2 substrate. The height of the nanopillars is 411 nm. (b) Schematic of FDTD calculation for the transmission coefficient and phase shift incurred by a beam after passing through a uniform set of pillar periodically arranged in a square lattice with $a = 350$ nm.	51
5.2	Field confinement in high-index dielectric nanopillar. Magnetic energy density inside a-Si nanopillars from the (a, b) top-view and (c, d) side-view. For the top-view, the monitors are placed at the end (a) and inside (b) the nanopillars. The elliptical diameters are $D_x = 168$ nm and $D_y = 270$ nm under TE-polarized plane-wave illumination. The dotted lines mark the boundaries of the nanopillars.	52
5.3	Transmission coefficients and phase shifts of the beam after passing through periodically arranged nanopillars for different diameters, D_x and D_y , under TE and TM-polarized plane-wave illumination.	52
5.4	Phase-to-diameter conversion map. Look-up table to convert a combination of $\phi_{\text{TE}} - \phi_{\text{TM}}$ phase shifts into the elliptical diameters of the nanopillars in (a) x and (c) y directions. (b, d) Transmission coefficients of the nanopillars as a function of the elliptical diameters.	53
5.5	Schematic diagram of a polarization-dependent metahologram.	55
5.6	Metahologram design calculations. (a) Schematic of the Gerchberg-Saxton algorithm. (b) Sample intensity constraints. In the spatial domain, $I(x, y)$ has a top-hat profile, while in the Fourier domain, $\hat{I}(\eta, \nu)$ contains the desired beam intensity shape.	56
5.7	Simulated metahologram output. Far-field intensity distributions obtained from FDTD calculations of the designed metahologram under (a) TE and (b) TM-polarized illumination. The insets show the far-field <i>amplitude</i> distributions, revealing no polarization cross-talk.	56

5.8	Experimental metahologram output. Far-field intensity distributions obtained by (a) TE and (b) TM illumination of a fabricated metahologram.	57
5.9	Optical setup for k-space measurements. Schematic of the optical setup used to characterize the diffraction efficiency of the polarization splitters. Col, collimator; P1, polarizer; BP, bandpass filter; A, aperture, $L_1 - L_5$, lenses; O1-O2, objectives; BS, beams splitter; C1-C2, cameras.	59
5.10	Fabricated metasurface-based polarization splitters. Scanning electron microscopy (SEM) images of the fabricated polarization splitter for $\alpha = 0.088$	59
5.11	Metasurface-based polarization splitter diffraction orders. Far-field intensity distributions obtained by (a) TE and (b) TM illumination of the polarization splitter.	60
5.12	Overall transmission efficiency of the metasurface-based polarization splitters. Simulated and experimental transmission efficiencies under TE and TM illumination.	60
5.13	Experimental diffraction efficiencies. Measured diffraction efficiencies of the metasurface-based polarization splitters.	61
5.14	Iterative calculation of the TIE.	64
5.15	Quantitative phase imaging configuration. (a) Schematic diagram of the metasurface (MS)-based quantitative phase imaging setup (MS-TIE). L_1 and L_2 form a $4f$ optical setup. The object located at input plane (IP) is illuminated with a 45° -plane polarized illumination. Note that IP can also coincide with the output or intermediate image plane of a conventional microscope. The metasurface is placed at the Fourier plane and acts as a polarization-dependent optical filter that splits two orthogonal polarization components into two different directions and axially shifts one polarization from the other. (b) Introducing an angular displacement θ at the Fourier plane corresponds to a transverse shift $f \tan \alpha$ at the output of the $4f$ setup. (c) Phase profiles of the metasurface to perform polarization splitting and axial translation.	65
5.16	Metasurface phase profiles. (a, b) Analytic and (c, d) designed phase profiles of the metasurface imparted to the (a, c) TE and (b, d) TM components of an incident wave. Yellow square depicts the size of the fabricated metasurface, $350 \times 350 \mu\text{m}^2$	68
5.17	Numerical simulation of MS-based TIE. Reconstructed phase profiles of (top row) convex and (bottom row) concave lenses with $f = 250$ mm using the conventional TIE and MS-TIE with the analytic (a-MS-TIE) and converted (MS-TIE) phase profiles.	69
5.18	Line profiles of the phase reconstructions. Phase line scans of the restored phase maps from the simulations for (a) convex and (b) concave lenses.	69
5.19	Fabricated metasurface for QPI. SEM images of the fabricated multifunctional metasurface employed for TIE-based QPI.	70
5.20	Experimentally obtained images from MS-based phase reconstruction of a convex lens. (a) Bright-field image (<i>false color</i>) of the object without the metasurface in the setup. Cropped images from the split (b) TE and (c) TM beams, respectively, from the MS-TIE. Scale bar: 0.5 mm	71
5.21	Reconstructed phase profiles of the convex lens. (a) Phase profile of the convex lens with focal length $f = 250$ mm using the analytic equation. (b) Reconstructed phase profile from FFT-based simulations of MS-TIE. Experimentally retrieved phase profiles from (c) MS-TIE, (d) conventional TIE (C-TIE) and (e) multiple-plane phase retrieval.	71
5.22	Converted optical thickness of the lens. (a) Horizontal (left) and vertical (right) line profiles of the optical thickness of the lens converted from MS-TIE and C-TIE. (b) Optical thickness profile from the MS-TIE reconstruction.	72

5.23	Experimentally obtained images from MS-based TIE configuration for a concave lens technical sample. Cropped images from the split (a) TE and (b) TM beams, respectively, from the MS-TIE. Scale bar: 0.2 mm	73
5.24	Reconstructed phase profiles of a concave lens. Phase profile of the concave lens reconstructed experimentally using (a) MS-TIE and (b) C-TIE. (c) Horizontal line profiles at the center of the phase maps and (d) continuous phase distribution of the MS-TIE reconstruction. Scale bar: 0.2 mm.	73
5.25	Schematic of the optical setup for the MS-TIE experiments. L1-L4, lenses; O1-O2, objectives; CCD, camera.	74
5.26	Experimentally obtained raw images of phase-only vertical bars from MS-TIE setup. Cropped images from the split (a) TE and (b) TM components using the MS-TIE setup. Scale bar: 20 μm	74
5.27	Reconstructed phase maps of phase-only vertical bars using (a) MS-TIE and (b) C-TIE. (c) Central line scan of the phase maps. (d) Continuous phase distribution of the MS-TIE reconstruction. Scale bar: 40 μm	75
5.28	Experimentally obtained raw images of phase-only horizontal bars from MS-TIE setup. Cropped images from the split (a) TE and (b) TM components using the MS-TIE setup. Scale bar: 20 μm	75
5.29	Reconstructed phase maps of phase-only horizontal bars using (a) MS-TIE and (b) C-TIE. (c) Central line scan of the phase maps. (d) Continuous phase distribution of the MS-TIE reconstruction. Scale bar: 40 μm	76
A.1	Schematic of the optical setup to obtain multiple intensities using noninterferometric methods. (a) Multiple-plane phase retrieval, (b) conventional TIE and (C) metasurface-based TIE.	89
A.2	Iterative phase retrieval using multiple intensity constraints.	90

1 Introduction

Throughout history, light-based technologies have been at the forefront of advancing our knowledge about nature. From Janssen's first invention of the compound microscope to Galileo's telescope, innovations in optics have assisted us in our quest to understand the smallest specimens on Earth as well as the largest structures in the universe. In the past decade or two, optical technologies have become ever more relevant and ingrained in our mundane activities. At the same time, our fundamental understanding of light has also significantly advanced.

Tremendous progress in computing and micro and nanofabrication technologies has ushered the realization of tools to control different properties of light with unprecedented precision. One of such properties is the wavefront or the phase of light. Traditionally, the most direct method to modulate the phase is by letting light pass through a refractive element. This is the mechanism behind most of today's commercial lenses, if not all. Diffractive optics have also been employed to flatten the thickness profile of the modulating element, but the mechanism is still based on light refraction. Spatial light modulators (SLM) based on liquid crystals have become a standard choice for wavefront engineering due to their real-time configurability, allowing for dynamic shaping of the wavefront. In the past decade, metasurface optics started to emerge, and have now gained significant attention due to the scale at which they modulate the wavefront. At the same time, the overall size of this new class of optical components is conducive for compact integrated setups that previously could not be attained with conventional optics. Additionally, metasurfaces have been demonstrated to achieve multiple functions simultaneously that can be realized traditionally only by a combination of bulky optical components.

Regardless of the mechanism of implementation, wavefront modulation has far-reaching applications. Imaging is one application that has greatly benefited from modulated wavefronts: by resolution and/or contrast enhancement. Placed in the illumination path, wavefront modulators can achieve structured or shaped illumination that can increase the resolution of the system. Placed in the imaging path, a wavefront modulator can influence the image resolution and/or contrast. Such is the case of the Nobel winning Zernike phase contrast technique. By introducing a phase-shift between the scattered and unscattered components of an incident field, the phase information was

directly mapped into a detectable amplitude variation [1]. Since then, a wide variety of optical filtering techniques based on wavefront modulation has popped out, the applications of which have gone beyond optical microscopy.

This thesis explores imaging applications of modulated wavefronts. Three applications are presented, each employing a different phase mask placed at the Fourier plane of a 4f optical architecture. The thesis is structured as follows:

In **Chapter 2**, the mathematics (Fourier optics) and some technical terms that are consistently used in all chapters are presented, after which wavefront modulation techniques are briefly surveyed.

In **Chapter 3**, a refractive element is employed to construct a common-path interferometer to determine the topological charge of helico-conical beams, which are a class of optical beams that carry orbital angular momentum. The phase-shifting element introduces a π -phase shift onto the unscattered component of the beam at the Fourier plane to synthesize a reference wave that interferes with scattered component. Similar to the Zernike phase contrast, this maps the phase of the helico-conical beams into a detectable intensity that allows for the topological charge determination.

In **Chapter 4**, an optical vortex, introduced by a liquid crystals-based element, is utilized in a nonlinear imaging setup to suppress bright sources and allow for the imaging of accompanying dim sources. This is an established technique called optical vortex coronagraphy or high-contrast imaging that is used to directly image exoplanets. The use of a nonlinear imaging system could potentially benefit the conventional optical vortex coronagraphy in terms of the system's wavelength tunability and broadband operation, even with the use of a vortex mask that operates for single-wavelength.

In **Chapter 5**, a metasurface-based optical element is exploited to facilitate the simultaneous recording of two images for noninterferometric quantitative phase imaging. The metasurface device splits the two orthogonal polarization components of an incident beam, and axially displaces one from the other. These two operations can be achieved traditionally with the use of multiple bulky optical components (e.g. an SLM, beam splitters and mirrors). The two images are used as constraints in an iterative algorithm to retrieve the phase profile of technical samples. In this chapter, we also present two other polarization-dependent wavefront modulators based on metasurfaces.

Chapters 3-5 start with an introduction on the specific work, followed by a mathematical description of the optical design and finally the results from numerical simulations and experiments. Utmost effort has been dedicated to the consistent use of variables in all chapters. However, a little mix-up was inevitable. It is therefore important to note that variables are defined in each chapter and in some cases, the same notation used in different chapters are not in any way related to each other.

2 Optical wave diffraction: definitions and some mathematical preliminaries

Diffraction can be loosely defined as the deviation of an optical wave from rectilinear propagation. It is commonly encountered when the extent of the wave is confined, for example, by an aperture. The development of the diffraction theory centuries ago led to a fundamental description of wave propagation, and still plays a vital role in describing many optical applications such as imaging. The utilization of analytic Fourier theory has made optical diffraction analyses easier to implement and visualize, thanks to efficient computational approaches of solving Fourier transforms combined with the inherent linearity of diffraction problems. In this chapter, a brief overview of optical wave propagation is presented, specifically, the reduction of Maxwell's equations to the so-called scalar diffraction formula. The basic definition and some theorems of Fourier transforms that are relevant for the succeeding chapters are also presented. The chapter ends with a brief review of wavefront engineering techniques which include the use of conventional and metasurface optics.

2.1 From Maxwell's equations to scalar wave equation

The propagation of optical waves can be described by Maxwell's equations, which in general, couple the electric field \vec{E} component of the wave to its magnetic field \vec{H} component. In the absence of free charges, the equations are given by

$$\nabla \times \vec{E} = -\mu \frac{\partial \vec{H}}{\partial t} \quad (2.1a)$$

$$\nabla \times \vec{H} = \epsilon \frac{\partial \vec{E}}{\partial t} \quad (2.1b)$$

$$\nabla \cdot \epsilon \vec{E} = 0 \quad (2.1c)$$

$$\nabla \cdot \mu \vec{H} = 0, \quad (2.1d)$$

where \vec{E} and \vec{H} have components (E_x, E_y, E_z) and (H_x, H_y, H_z) , respectively, while ϵ and μ are the corresponding electric permittivity and magnetic permeability of the medium in which the

wave is propagating. In the case where the medium is a dielectric, i.e. $\epsilon > 0$, that is considered *linear* (field from multiple sources can be summed), *isotropic* (polarization-independent permittivity), *homogeneous* (position-independent permittivity), *nondispersive* (wavelength-independent permittivity) and *non-magnetic* (magnetic permeability is equal to the vacuum permeability), the field components in Maxwell's equations become decoupled and follow the wave equation:

$$\nabla^2 \vec{E} - \frac{n^2}{c^2} \frac{\partial^2 \vec{E}}{\partial t^2} = 0 \quad \text{and} \quad \nabla^2 \vec{H} - \frac{n^2}{c^2} \frac{\partial^2 \vec{H}}{\partial t^2} = 0 \quad (2.2)$$

where $n = \sqrt{\frac{\epsilon}{\epsilon_0}}$ is the refractive index of the medium and $c = \frac{1}{\sqrt{\mu_0 \epsilon_0}}$ is the speed of light in vacuum. Since each of the three components of the electric field and magnetic field follows the wave equation, their behaviour can be summarized into one scalar wave equation given by

$$\nabla^2 u(\mathbf{r}, t) - \frac{n^2}{c^2} \frac{\partial^2 u(\mathbf{r}, t)}{\partial t^2} = 0. \quad (2.3)$$

Here, the field components are represented by $u(\mathbf{r}, t)$, which also shows their explicit dependence on the position $\mathbf{r} = (x, y, z)$ and time t . Equation 2.3 simplifies the analysis of how a wave propagates or behaves under the specific conditions described above. While the premise of having the wave propagation happen in an *ideal* (fulfilling the aforementioned conditions of being linear, homogenous, nondispersive and non-magnetic) medium seems rather restrictive, this mathematical simplification is valid for a large number of situations. For example, free-space propagation, which is frequently used in optical imaging and communications systems analysis, the assumptions are clearly satisfied, but the validity of the scalar wave theory extends even to situations where light diffracts around objects or structures, as long as the feature sizes and observation distance are much larger than the wavelength of the incident light. In cases where the assumptions fail, for example when light propagates in subwavelength structures, the vectorial nature of light (i.e. Maxwell's equations) should be considered. Our work on metasurfaces as discussed later in Chapter 5 presents one such example where the full-wave calculation needs to be implemented. For now, supposing that these assumptions hold, consider the following function that is a solution to the scalar wave equation,

$$u(\mathbf{r}, t) = A(\mathbf{r}) \cos[\phi(\mathbf{r}) - 2\pi\nu t] = \text{Re} \{ A(\mathbf{r}) \exp [i\phi(\mathbf{r}) - i2\pi\nu t] \} \quad (2.4)$$

$u(\mathbf{r}, t)$ describes a monochromatic wave with temporal frequency ν and having position-dependent real amplitude $A(\mathbf{r})$ and phase $\phi(\mathbf{r})$. Direct substitution of Equation 2.4 to 2.3 leads to the Helmholtz wave equation given by

$$(\nabla^2 + k^2) u = 0. \quad (2.5)$$

Propagation in a linear medium means that the temporal frequency remains constant and can therefore be omitted to simplify notation. For further simplification, consider the case of a paraxial wave propagating along the z direction; Equation 2.4 can be written as

$$u(\mathbf{r}) = A(x, y) \exp [i\phi(x, y)] \exp(-ikz) \quad (2.6)$$

where $k = \frac{2\pi}{\lambda}$ is the wave number and λ is the vacuum wavelength. The explicit z -dependence can again be omitted to define the transverse complex field profile

$$u(x, y) = A(x, y) \exp [i\phi(x, y)]. \quad (2.7)$$

In the thesis, $u(x, y)$ will also be referred to as the *complex field amplitude* of a beam at a defined z -position in the optical axis.

2.2 Fourier optics

At this point, it is worthwhile to introduce the basic definition and theorems of Fourier transforms, which will also provide context to later discussions in this and the succeeding chapters.

2.2.1 Analytic Fourier theory

Definition

Given a function g of two variables x and y in the *spatial domain*, its Fourier transform (or *frequency spectrum*) is

$$\mathfrak{F}\{g(x, y)\} = G(f_x, f_y) = \int_{-\infty}^{\infty} \int_{-\infty}^{\infty} g(x, y) \exp[-i2\pi(f_x x + f_y y)] dx dy, \quad (2.8)$$

where \mathfrak{F} denotes the Fourier transform operation, $G(f_x, f_y)$ is the transform result, f_x and f_y are independent spatial frequency variables associated with the x and y directions, respectively. Meanwhile, the inverse Fourier transform, denoted by $\mathfrak{F}^{-1}\{G(f_x, f_y)\}$, is given by

$$\mathfrak{F}^{-1}\{G(f_x, f_y)\} = g(x, y) = \iint_{-\infty}^{\infty} G(f_x, f_y) \exp [i2\pi (f_x x + f_y y)] df_x df_y \quad (2.9)$$

Fourier transform theorems

Table 2.1 summarizes some basic mathematical properties of Fourier transforms, which will also find useful in later chapters and have the following implications:

- Linearity theorem: The transform of the sum of two weighted functions is the weighted sum of their individual transforms.
- Shift theorem: The transform of a transversely shifted function corresponds to the transform of the function gaining a linear phase shift in the Fourier domain.
- Convolution theorem: The transform of the convolution of two functions is the product of the individual transforms of the two functions.

Table 2.1: Fourier transform theorems

Theorem	Expression
Linearity	$\mathfrak{F}\{Ag(x, y) + Bh(x, y)\} = A\mathfrak{F}\{g(x, y)\} + B\mathfrak{F}\{h(x, y)\}$
Shift	$\mathfrak{F}\{g(x - a, y - b)\} = G(f_x, f_y) \exp[-i2\pi (f_x a + f_y b)]$
Convolution	$\mathfrak{F}\{\iint g(\eta, \nu)h(x - \eta, y - \nu)d\eta d\nu\} = G(f_x, f_y)H(f_x, f_y)$
Central ordinate (zero-frequency)	$\mathfrak{F}\{g(x, y)\} _{f_x=0, f_y=0} = G(0, 0) = \iint g(x, y)dx dy$

Given an input function $g_1(x_1, y_1)$ that can be decomposed into several weighted elementary functions, a system with a known operation S is *linear* if the output $g_2(x_2, y_2)$ is just the weighted sum of the results of S operating on the individual functions. Additionally, it is considered *space-invariant* if the operation only depends on the relative positions between two points in the input and the output. For systems that satisfy both these properties, i.e. space-invariant linear systems, the output is specified by

$$g_2(x_2, y_2) = \iint_{-\infty}^{\infty} g_1(x_1, y_1)h(x_2 - x_1, y_2 - y_1)dx_1 dy_1. \quad (2.10)$$

Here, $h(x_2 - x_1, y_2 - y_1)$ is the so-called *impulse response*, which is also known as the *point-spread function* (PSF) in imaging systems. Equation 2.10 implies that the output is the convolution between the input and the system's impulse response. In shorthand notation,

$$g_2(x, y) = g(x, y) \otimes h(x, y) \quad (2.11)$$

where \otimes denotes the convolution operator and the subscripts are unnecessary and dropped. Calculation of the convolution integral can become tedious especially when implemented numerically. In most cases, it can be simplified using the convolution theorem of Fourier transforms (see Table 2.1). From Equation 2.10,

$$g_2(x, y) = \mathfrak{F}^{-1} \{G(f_x, f_y)H(f_x, f_y)\} \quad (2.12)$$

Here, $H(f_x, f_y)$ is known as the *transfer function* of the space-invariant linear system which is regularly used to describe spatial frequency-filtering methods in imaging systems.

2.2.2 Rayleigh-Sommerfeld diffraction formula

Classical scalar diffraction theory aims to model optical wave propagation through free-space or similar media. Such a theory deterministically predicts the evolution $u_2(x, y)$ of a transverse field profile $u_1(x', y')$ at an observation plane that is separate from and parallel to the source plane, as schematically shown in Figure 2.1.

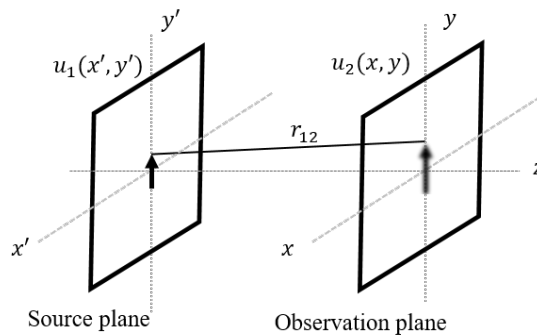


Figure 2.1: **Scalar wave propagation.** Schematic diagram of complex field profile at a source plane being observed at a parallel observation plane, a distance z away.

Describing wave propagation through diffraction has been tackled by finding solutions to the

Helmholtz equation with appropriate application of boundary conditions; a detailed derivation of which can be found in reference [2]. In this thesis, it suffices to say that the final solution, $u_2(x, y)$, at an observation plane with a distance z from the source plane is given by the Rayleigh-Sommerfeld (RS) diffraction integral,

$$u_2(x, y) = \frac{z}{j\lambda} \iint_{\Sigma} u_1(x', y') \frac{\exp(ikr_{12})}{r_{12}^2} dx' dy' \quad (2.13)$$

where $r_{12} = \sqrt{(x - x')^2 + (y - y')^2 + z^2}$ is the distance between two points at the source and the observation planes, and Σ corresponds to the area of the source that serves as the limits of integration for x' and y' . Equation 2.13 is reminiscent of a superposition integral, and is an expression of the Huygens-Fresnel principle, which supposes that the source is composed of infinite number of point sources, each emitting a spherical wave. These waves then travel and interfere with each other, and the superposition of which at a particular position (x, y) in the observation plane specifies the complex field value at that point. In short-hand notation, the RS diffraction integral can be written as the convolution of the source field and the RS impulse response, $h_{\text{RS}}(x, y) = \frac{z}{i\lambda} \frac{\exp(ikr)}{r^2}$,

$$u_2(x, y) = u_1(x, y) \otimes h_{\text{RS}}(x, y) \quad (2.14)$$

In the aforementioned context, wave propagation is inherently linear and space-invariant; thus, analytic Fourier theory holds and greatly simplifies analysis of optical diffraction. This branch of optical science is known today as *Fourier optics*. From the convolution theorem, Equation 2.14 can be written as

$$u_2(x, y) = \mathfrak{F}^{-1} \{ \mathfrak{F} \{ u_1(x, y) \} H(f_x, f_y) \} \quad (2.15)$$

$$H_{\text{RS}}(f_x, f_y) = \exp \left(ikz \sqrt{1 - (\lambda f_x)^2 - (\lambda f_y)^2} \right) \quad (2.16)$$

$H(f_x, f_y)$ is the RS transfer function. Equation 2.16 is usually derived using the angular spectrum method where the incident field is decomposed into its plane wave (Fourier) components. The output at a parallel plane is the superposition of these Fourier components accounting for the phase

shifts that each undergoes as it propagates from the source to the observation plane. The *spatial frequencies* (f_x, f_y) are related to the transverse components of the wavevector by $f_x = \frac{k_x}{2\pi}$ and $f_y = \frac{k_y}{2\pi}$ [2, 3]. Importantly, other propagation integrals (i.e. Fresnel and Fraunhofer) can be derived from the RS diffraction integral by application of different approximations.

Imaging with a $4f$ optical setup

It can be shown that a lens physically performs Fourier transformation of an input field at its back-focal plane [2, 3]. Such a physical realization has paved the way for different spatial frequency-space manipulation of an incident field, and is the basis of the presented works in this thesis. The optical architecture shown in Figure 2.2 is commonly known as a $4f$ setup since the input and the output are separated by four separate distances, each has length f . In a typical $4f$ imaging configuration, a plane-wave illuminates a two-dimensional object that can be represented by $u_1(x, y)$ located at the input plane P1 of the setup. A first transforming lens, L_1 , is placed a distance f away from the input. At the back-focal plane P2 of L_1 , the spatial Fourier decomposition of the input $U_1(f_x, f_y) = \mathfrak{F}\{u_1(x, y)\}$ is obtained. Here, an optical filter, which can be described by a complex transmittance function $t(\eta, \nu)$, can be inserted to achieve different desired operations on the spatial frequencies of the input field. Another f -distance from P2, a second lens L_2 is employed to perform a second Fourier transformation, yielding the $4f$ output $u_2(x, y)$ at P3, the back-focal plane of L_2 . In terms of the input field, the output can be expressed as

$$u_2(x, y) = \mathfrak{F}^{-1}\{U_1(f_x, f_y)t(\eta, \nu)|_{\eta=\lambda f f_x, \nu=\lambda f f_y}\} \quad (2.17)$$

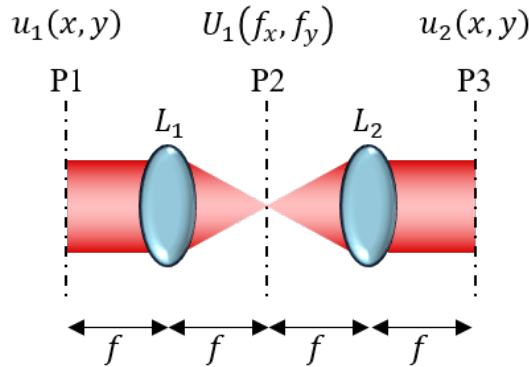


Figure 2.2: A $4f$ optical configuration. P1, input plane; P2, Fourier plane; P3, output plane; L1-L2, lenses; f , focal length.

Note that in the absence of a filter, the output field appears an inverted input due to the imaging configuration.

2.3 A review of beam engineering techniques

Beam engineering lends itself into many optical applications such as imaging [4], communications [5], optical micromanipulation [6, 7] and microfabrication [8, 9], among others. While beam engineering may refer to the modulation of different properties of an incident light, in this section we will only focus on amplitude and phase modulations. The latter is also known as *wavefront engineering*. Engineered wavefronts have found use in more efficient shaping of a beam's intensity profile for the aforementioned applications. In this thesis, *wavefront engineering encompasses any practice that modulates the phase of a beam regardless of the intended application or the method of implementation*. For example, in imaging, wavefront engineering can refer to either modulating the phase of the illumination before the sample, or that of the wave that has already passed through the sample. Both these techniques aim to enhance the performance of the imaging system in terms of resolution and/or contrast, but are implemented differently. Wavefront engineering is typically performed by letting the incident light pass through an optical element that imprints a phase profile, which may depend on the optical architecture being employed, to achieve whatever the desired output is. In contrast to amplitude modulation, phase modulation naturally leads to higher efficiency as it does not involve any beam truncation, but rather it just redirects or redistributes light to attain the output beam. In the following, two different mechanisms on how to modulate a beam's wavefront are introduced: conventional optics and metasurface optics.

2.3.1 Conventional optics

Refractive optical elements

Perhaps the simplest way to imprint a specific phase profile on an incident optical wave is by the use of a refractive element (i.e. glass) with a spatially varying thickness profile. The phase is accumulated as the light propagates through the element, and in the end produces a beam with the desired properties. For example, refractive axicons are now commercially available to convert an incident Gaussian beam into Bessel beams [10]. By controlled manipulation of the phase profile of an incident Gaussian beam, output beams with uniform profiles (i.e. flat intensity and wavefront) have been demonstrated [11–13]. Probably the most commonly used refractive optical element is

the traditional spherical lens, whose radially-dependent thickness induces phase shift that results in the convergence (or divergence) of the optical beam at the back-focal plane. While refractive elements have an advantage of high efficiency and broadband operation, fabricating tall structures can be quite challenging, which is a primary reason why a lens with high numerical aperture is difficult to achieve from a single optical element [11, 14].

Conventional diffraction-based optics

In principle, the surface profile of refractive phase masks can be flattened by introducing a maximal phase value that the optical element imprints, which is usually 2π . The phase is therefore wrapped from 0 to 2π , introducing discontinuities in an otherwise continuous profile. For conventional diffractive elements, the phase induced still depends on the optical path length that light travels within the material, which is similar to the mechanism behind refractive elements. For diffractive lenses, the thickness profile is divided into concentric rings that impart appropriate phase values. Focusing is achieved by constructive interference of the transmitted waves through the rings. One problem in diffractive optics is the strong chromatic dependence, which for the case of diffractive lenses, leads to different focusing planes for different wavelengths. One suggestion to tackle such a challenge is by the use of a multilevel design [15].

Liquid-crystals spatial light modulators

Phase-only spatial light modulators (SLM) have become ubiquitous in any research that deals with beam shaping. One of the primary reasons is the tunability afforded by SLMs, which allows for dynamic beam shaping that can be tailored for specific applications. Phase-only SLMs usually consist of a layer of liquid crystals (LC), whose inherent birefringence induces the phase shift in the incident light as it passes through. In an LC molecule, the birefringence is defined as $\Delta n = n_e - n_o$, where n_o is the ordinary refractive index of the polarization component of the incident light that is perpendicular to the LC director (long axis) and n_e is the refractive index for the parallel component. By changing the voltage across a layer of LCs, the molecules re-orientate around an axis orthogonal to both the incident polarization and the propagation direction. This changes the effective refractive index, resulting in the phase modulation of the incident wave that can be adjusted by proper setting of the applied voltage. The induced phase shift is then given by $\delta = 2\pi\Delta nd/\lambda$, where d is the thickness of the LC layer and λ is the incident wavelength [16]. SLMs have been extensively used in optical micromanipulation applications [6, 13], optical communications [5] and

performance enhancement in optical imaging [4]. To this end, we have employed SLMs for beam shaping [17, 18], and for optical manipulation and actuation of microstructures in a fluid [19].

2.3.2 Metasurface optics

Metasurfaces are composed of subwavelength unit structures, called meta-atoms, that are capable of locally modifying the properties of an incident light, including its phase. In comparison with conventional refractive and diffractive optics, the mechanism behind the induced phase shift on the input beam is fundamentally different. Metasurfaces exploit nanoscale light-matter interactions that can be tuned to achieve the desired phase response in the transmitted/reflected wave. In such a regime, the field components in Maxwell's equations are coupled, rendering the scalar wave theory not applicable in this case. In most cases, it is also futile to find analytic solutions to the Maxwell's equations due to the complicated geometries involved. As such, numerical approaches are utilized to investigate the response of an optical wave due to such structures. Figure 2.3 shows a schematic that compares a metasurface with conventional refractive and diffractive elements. Depending on the constituent material, metasurfaces can either be plasmonic or dielectric.

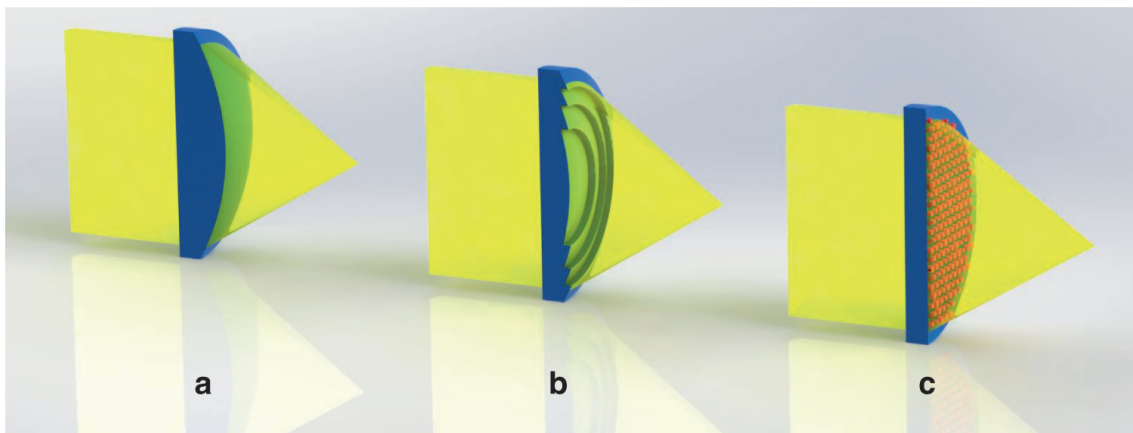


Figure 2.3: **Wavefront engineering mechanisms.** Wavefront shaping using (a) refractive element, (b) diffractive element and (c) a metasurface. Image is adapted from [20].

Plasmonic metasurfaces

Plasmonic metasurfaces are comprised of metallic components (nanostructure/nanoparticle) whose optical responses arise from the plasmon resonances they support. The collective oscillation of the conducting electrons under an external time-varying electromagnetic field can be described by the Drude's free electron model [21, 22]. Localized surface plasmons (LSP) are a fundamental plasmonic excitation that constitute non-propagating oscillations of the conducting electrons. Resonant

excitation leads to huge field enhancements as well as strong scattering, determined by the polarizability, which is dependent on the geometry and material properties of the metallic nanoparticle. The strong interaction between LSPs and the incident electromagnetic field facilitates the phase tuning of the scattered field. For example, resonant excitation can be attained by properly setting the length of an elongated nanoparticle (i.e. a nanoantenna); under such condition, the excited current, a result of charge oscillations along the axis of the nanoantenna, is in phase with the incident electromagnetic field. Consequently, since the scattered light originates from the oscillating antenna current, its phase can be tuned by appropriate choice of the antenna length [23]. With a single nanoantenna, up to π -phase shift tuning can be achieved. The response can be extended to cover the 2π phase modulation, for example, by utilizing the so-called geometric phase or Pancharatnam-Berry (PB) phase[24–28]. The PB phase is the acquired phase due to polarization change of the optical wave transmitted through or reflected from anisotropic, subwavelength scatterers. The mechanism can be readily understood with a circularly polarized light incident on the scatterer. The scattered field consists of a linear combination of co-polarized and cross-polarized components, with the cross-polarized field gaining additional phase that is dictated by the rotation angle of the scatterer. In a plasmonic meta-atom, the amplitude of the cross-polarized outgoing wave is influenced by the resonance, while the phase shift is determined from a purely geometric origin, being twice the angular orientation of the meta-atom. Even before the advent of plasmonic metasurfaces in the past decade, the PB phase has already been demonstrated using subwavelength gratings [25, 26] and birefringent crystals [29]. Metasurfaces are good alternatives because properly designed meta-atoms can exhibit strong birefringence, allowing therefore for subwavelength phase tuning. Since the modulation has also a weak wavelength dependence, broadband operation is possible while sustaining uniform amplitude regardless of the phase-shift introduced. Spatial distribution and proper arrangement of the meta-atoms in a 2D periodic lattice facilitates the realization of any phase motif for 2D wavefront shaping. Additionally, the subwavelength spacing between the meta-atoms eliminates higher diffraction orders, which is a persistent problem in conventional diffractive wavefront shapers. While such functionalities can be very appealing in wavefront engineering, the material losses incurred from plasmonic metasurfaces limit their range of applications. Several studies have delved into improving the overall efficiencies in plasmonic metasurfaces [30–32]; however, the demand for efficiencies that can compete with conventional optical components has paved the way for the use of all-dielectric platforms as con-

stituent materials for metasurfaces.

All-dielectric metasurfaces

All-dielectric metasurfaces are composed of low-loss dielectric materials, promising highly efficient wavefront engineering and at the same, inheriting the benefits of subwavelength tuning similar to their plasmonic counterparts. Dielectric materials with high refractive index are employed as constituting materials for this type of metasurfaces, in which wavefront tuning is commonly based on: 1) Mie resonances [33, 34], 2) geometric phase [35, 36] and 3) dynamic or propagation phase [37, 38]. High-index dielectric nanoparticles can exhibit electric and magnetic dipole, and higher order Mie resonances that can lead to strong magnetic response, which in turn can be exploited to enhance light manipulation in the sub-diffraction regime. By engineering the geometries of the nanoparticles, multipolar modes can be generated and made to interfere, enabling the tailored control of the scattered light. In nanodisks, for example, a strong magnetic resonance occurs when the diameter becomes comparable to λ/n , where n is the refractive index of the material. By spectrally overlapping the electric and magnetic resonances, forward scattering is enhanced while backward scattering is suppressed. This is the mechanism behind the Huygen's metasurfaces [39–41]. Within the overlapped spectra, high transmittance is attained, and around the resonance wavelength, the total electric field undergoes a 2π -phase change. By varying the lattice period or meta-atom dimensions, the resonance can be spectrally shifted to tune the phase modulation locally introduced to the incident wave [40, 41]. In contrast to the first mechanism, the geometric phase is polarization-dependent relying on the same mechanism as in the PB phase in plasmonic metasurfaces [35]. Here, the birefringence is introduced by structurally anisotropic meta-atoms that are also composed of high-index dielectric material. Spatially dependent phase tuning is achieved by meta-atoms with identical structural parameters but varying orientation. Finally, the propagation or dynamic phase allows the independent shaping of two orthogonal polarization components, owing to the large contrast between the refractive indices of the dielectric meta-atom and the medium [37, 38, 42]. The nanostructures are thicker (about 0.5λ to λ) than those employed in Huygen's metasurfaces and can be considered as truncated waveguides, inside which, multiple Fabry-Pérot modes are excited. Light is mainly confined in the dielectric medium, and coupling between neighboring meta-atoms is insignificant [37, 43, 44]. As such, the local properties of the scattered wave are primarily determined by the geometrical properties of a meta-atom and have negligible dependence on the neighboring meta-atoms. This means that each meta-atom can be regarded as a

pixel that locally modulates the phase of the incident wave. Additionally, structural anisotropy, for example with the use of elliptical nanopillars as meta-atoms, leads to different effective refractive indices of the polarized components directed along the two ellipse diameters. Thus, by careful arrangement of the elliptical pillars, the wavefronts of two orthogonal polarization components of an incident light can be manipulated simultaneously.

2.4 Summary

To summarize the chapter, the scalar wave propagation formula was presented starting from the Maxwell's equations. Beam shaping techniques were also discussed. While metasurfaces may provide clear advantage over the others in terms of the resolution and overall size of the wavefront-shaping optical element, some situations or applications that do not really rely on such a high-precision wavefront engineering may benefit from the other techniques. We present an example in the next chapter, where a simple etched glass is employed in a typical imaging setup to determine the characteristic properties of beams that have orbital angular momentum.

3 Topological charge measurement using a common-path interferometer

3.1 Introduction

Optical beams with orbital angular momentum (OAM), also known as optical vortex beams, have a plethora of applications that have gained footing in the fields of optical communications [5], high-resolution imaging [4], optical manipulation [45] and photolithography [46]. Among the OAM-carrying beams, Laguerre-Gaussian (LG) beams are perhaps the most common and simplest case. Mathematically, their complex field can be described by $\exp(il\phi)$, where ϕ is the azimuthal angle [47]. Such a ϕ -dependent profile results in the spiraling of the wavefront about the optical axis as the beam propagates, and at the center of which, phase is undefined. The OAM properties of an LG beam are specified by the topological charge l , whose magnitude and sign determine the number of twists the beam experiences in one wavelength of propagation and the direction of the rotation, respectively. The magnitude determines “how fast” the beam is rotating about the axis and, in quantum optics, it is related to the extrinsic angular momentum of a photon, $l\hbar$, while the sign is also known as the helicity of the beam. In the far-field, one striking feature of such beams is the doughnut-shaped intensity profile consisting of a dark central core surrounded by a bright ring. This is a result of the phase singularity at the beam’s center.

Studies on OAM-carrying beams are geared towards how to generate or detect them, or investigating how they interact with matter. There are numerous ways to generate LG beams, which will be further introduced in Chapter 4; the most intuitive way is the use of phase plates to introduce the helical profile [47]. This, perhaps, is also the prevalent method being used in the literature. Detection of the OAM properties of LG beams is of equal importance, especially with the emergence of their application in optical communications in the past decade [5]. The topological charge magnitude and sign of LG beams can be ascertained commonly by looking at their diffraction through apertures and optical elements, or by interfering them with a reference wave. Most often than not, both the magnitude and sign manifest in the output intensity. Current methods for charge determination include but are not limited to the use of amplitude diffractive apertures [48–50], interferometry

[51–53], and spatial mode projection [54]. The use of phase-only elements has also been employed due to their higher efficiency compared to their amplitude-only counterparts [55, 56].

In this chapter, we introduce an in-line interferometric technique that is based on a simple refractive element to determine the topological charge of a class of OAM-carrying beams, called helico-conical beams. The common-path interferometer (CPI) employed in this work is based on the generalized phase contrast (GPC), which is an extension of the Zernike phase-contrast technique [1] to accommodate large phase variations [13]. The rest of this chapter is structured as follows: first an introduction of helico-conical beams, followed by the mathematical model and experimental demonstration of the CPI-based topological charge detection, and in the end, a summary of the chapter.

3.2 Helico-conical beams

Helico-conical beams (HCB) are a different class of OAM-carrying beams that are characterized by their helical intensity and phase profiles. The phase distribution of HCBs has a non-separable radial and azimuthal components, being the product of helical and conical phase fronts given by [57]

$$\varphi_{\text{HCB}}(r, \phi) = l\phi \left(K - \frac{r}{r_0} \right), \quad (3.1)$$

where (r, ϕ) are the radial and azimuthal coordinates with $r = \sqrt{x^2 + y^2}$ and $\phi = \tan^{-1} \left(\frac{y}{x} \right)$, K is a constant between 0 and 1, l is the topological charge, and r_0 normalizes the radial coordinate, which is usually set to be the same as the beam radius. Figure 3.1 shows the phase distributions of HCB for $K = 0, 1$ and $l = 0, 1$. In LG beams, the phase increases along the azimuth and remains constant radially, while for HCBs, it also linearly scales with the radial coordinate. As a result, HCB intensity profiles in the far-field are strikingly different from those of LG beams, and are characterized by having spiral distributions, as opposed to the doughnut-shaped intensity profiles of LG beams [57]. Figure 3.2 shows the spiral intensities at the focused plane of HCBs for different topological charges.

The far-field evolution of HCBs and their propagation dynamics have been reported in [57] and specifically for $K = 0$ in [58]. In both studies, it was shown that the spiral intensities scale linearly

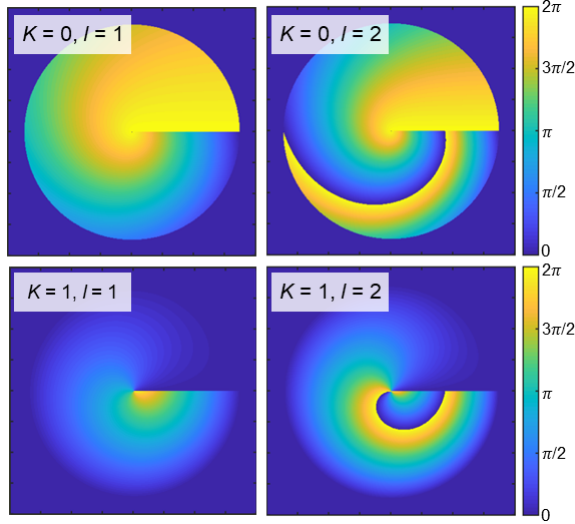


Figure 3.1: **Helico-conical beams phase profiles.** Wrapped phase profiles of helico-conical beams for $K = 0, 1$ and $l = 1, 2$, showing the radial and azimuthal dependence of the phase.

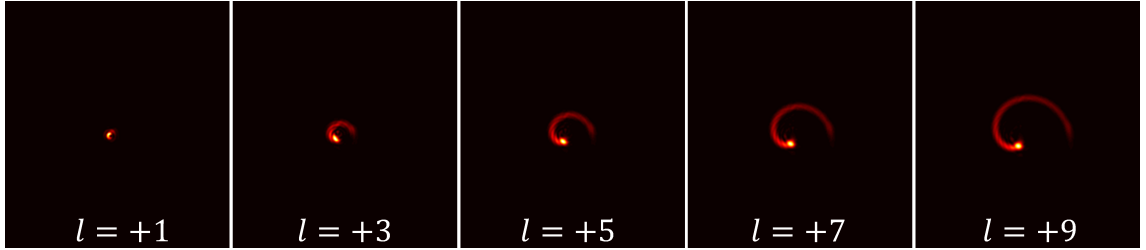


Figure 3.2: **Helico-conical beams far-field intensity profiles.** Spiral far-field intensities of helico-conical beams with $K = 0$ and $l = 1, 3, 5, 7$ and 9 .

with the topological charge of the incident beam. For HCBs with $K = 0$, not only do the phase and amplitude of the beam twists about the optical axis, but they also maintain high photon density even for larger l 's [58]. This is in contrast with LG beams where, as the charge increases, the photons are also known to spread in a wider area. As such, optical twisters have been envisioned to benefit applications where large l 's and high concentration of photons at the focus are needed. Similar to other OAM-carrying beams, it is also important for some applications to deduce the topological charge of an incoming HCB. Here, we show that a phase-contrast image can be generated from the HCB, specifically the case of $K = 0$, that allows for the determination of both the magnitude and sign of the topological charge. In far-field intensity measurements, a lens is usually employed to visualize the helical intensity profile at the lens' back-focal plane. Instead, a CPI is proposed for charge detection, where a second lens is added to form a $4f$ optical setup and a phase-shifting element is placed at the center of the Fourier plane. In the next section, the optical design of the common CPI is discussed.

3.3 Common-path interferometer

Figure 3.3 illustrates the schematic diagram of the $4f$ -based CPI. A phase object truncated by a circular aperture is located at the front focal plane of the first lens, which implements an optical Fourier transformation of the input field. This spatially separates the zero-order or on-axis (low-frequency components) and off-axis scattered light (high-frequency components) at the back-focal plane of L1. The focused light corresponds to light directly propagated through the object, while the scattered light is a result of the spatially varying object information. A phase-shifting element called phase-contrast filter (PCF) is placed at the center of the Fourier plane. The PCF modulates the amplitude and phase components of the focused and scattered light. Specific in this work, a θ phase-shift is applied onto the focused light within a circular region of radius R_1 while the amplitude for both focused and scattered light remains almost unperturbed. The phase-shifted low-frequency components serve as the synthetic reference wave (SRW) which interferes with the scattered light to facilitate the formation of the phase-contrast image after the second lens.

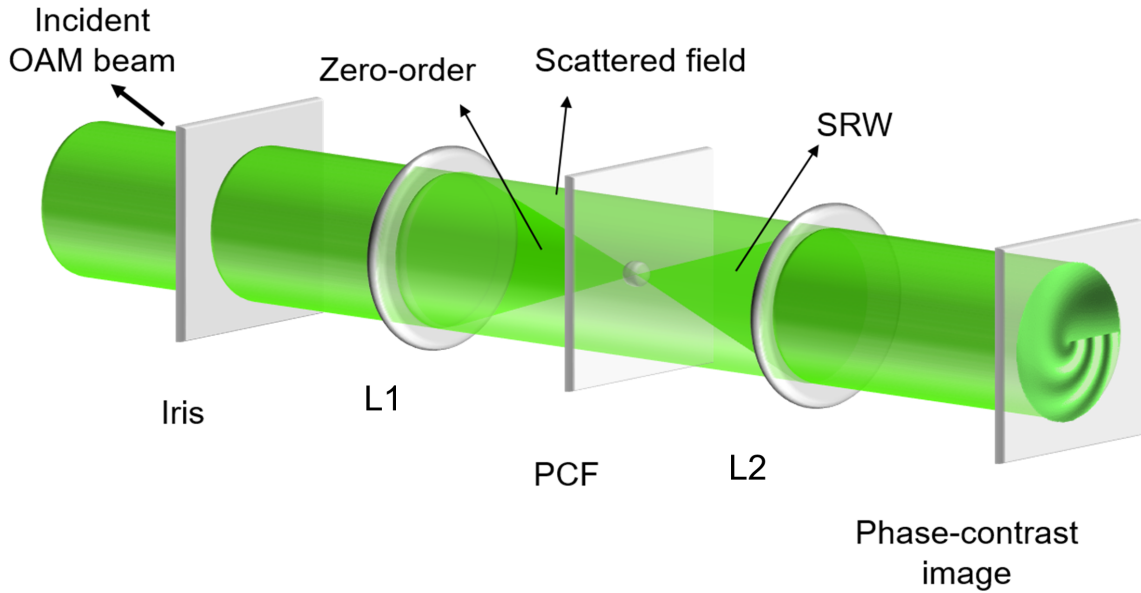


Figure 3.3: **Common path interferometer for topological charge detection.** Schematic diagram of the common-path interferometer built from a $4f$ optical setup. The phase-contrast filter (PCF) introduces θ -phase shift to the low-frequency components of the incident HCB that serve as the synthetic reference wave.

In the following derivation, it is shown that the coherent superposition of the SRW with the scattered light results in the direct mapping of the HCB phase into the CPI interferogram. From an approximate description for the intensity distribution, the parameters for the CPI output optimization are discussed to produce sufficient visibility and irradiance for topological charge determination

of HCBs.

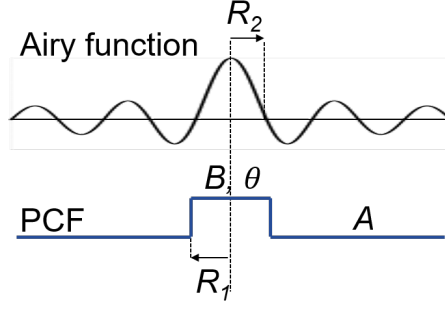


Figure 3.4: Schematic of the PCF relative to the Airy profile incident on it at the Fourier plane. A, B are transmittance used to adjust the relative strength of the SRW relative to the scattered field. θ is the amount of phase shift introduced to the zero-order, R_1 is the PCF radius and R_2 is the Airy radius. The Airy profile is generated at the Fourier plane by the input circular aperture with $R_2 = 0.61\lambda f/r_0$.

The PCF's transmittance function defines the amplitude transfer function $H(f_x, f_y)$ of the $4f$ -based CPI and can be expressed as

$$H(f_x, f_y) = A \left(1 + \left(BA^{-1}e^{i\theta} - 1 \right) \text{circ} \left(\frac{f_r}{\rho_0} \right) \right), \quad (3.2)$$

where $\theta \in [0, 2\pi]$ by the PCF, (f_x, f_y) are the spatial frequency coordinates, $\rho_0 = R_1/\lambda f$, and A and $B \in [0, 1]$ are the transmittance factors outside and inside the region of the PCF, respectively, f and λ denote the focal length of the lenses and the illumination wavelength of the setup. The function $\text{circ} \left(\frac{f_r}{\rho_0} \right)$ denotes a value of 1 within the circular region of radius ρ_0 and 0 otherwise. This means that all spatial frequencies with magnitude $\sqrt{f_x^2 + f_y^2} \leq \rho_0$ are θ -phase shifted by the PCF. These parameters are depicted in Figure 3.4. In practice, the PCF is made of glass and so as mentioned earlier, the amplitude of both the focused and scattered light is unperturbed; hence, from here on, the transmittance factors A and B are set to 1. From the transfer function, the corresponding point-spread function (PSF) of the system is

$$h(x', y') = \mathfrak{F} \{ H(f_x, f_y) \} = \delta(x', y') + \left(e^{i\theta} - 1 \right) \rho_0 J_1(2\pi\rho_0 r')/r' \quad (3.3)$$

where \mathfrak{F} represents the Fourier transform operator, (x, y) and (x', y') are the spatial coordinates at the input and output planes of the CPI, and J_1 is the Bessel function of the first kind of order one. For an input field $u(x, y) = a(x, y)e^{i\varphi(x, y)}$, the CPI intensity output is given by

$$I(x', y') = |u(x', y') \otimes h(x', y')|^2 \quad (3.4)$$

$$I(x', y') = \left| u(x', y') + \left(e^{i\theta} - 1 \right) \left[u(x', y') \otimes \rho_0 J_1(2\pi\rho_0 r')/r' \right] \right|^2. \quad (3.5)$$

Here, \otimes denotes the convolution operator. The second term in Equation 3.5 comprises the SRW of the CPI, whose interference with the imaged input field $u(x', y')$ produces the CPI intensity output. The SRW is not only dependent on the PCF parameters (i.e. phase shift θ and size ρ_0), but also on the object. This indicates that the SRW does not always have a flat profile over the system output aperture, which has been assumed so in previous phase-contrast imaging techniques. For this reason, the CPI just presented has been termed generalized phase contrast (GPC) method [13, 59]. We follow the approximation in [59, 60]: for a PCF that is well within the main lobe of the Airy function produced by the circular input aperture, $R_1 < R_2$ (see Figure 3.4) in the Fourier plane, the field within the PCF central region can be approximated as having an Airy profile that is scaled by the complex zero-frequency value. Mathematically, this reduces the intensity profile into

$$I(x', y') \approx \left| u(x', y') + \bar{\alpha} \left(e^{i\theta} - 1 \right) g(x', y') \right|^2, \quad (3.6)$$

where $\bar{\alpha}$ is the normalized zero-order (complex zero-frequency value) given by [2]

$$\bar{\alpha} = |\bar{\alpha}| e^{i\varphi_{\bar{\alpha}}} = \frac{\iint u(x, y) dx dy}{\iint a(x, y) dx dy} \quad (3.7)$$

while

$$g(r') = 2\pi r_0 \int_0^{\rho_0} J_1(2\pi r_0 f_r) J_0(2\pi f_r r') df_r. \quad (3.8)$$

Note that with the assumption above, the SRW no longer strictly depends on $u(x', y')$, which is valid for phase objects. To examine the effect of the PCF size relative to the Airy profile radius, the dimensionless variable η is introduced:

$$\eta = \frac{R_1}{R_2} = \frac{r_0 R_1}{0.61 \lambda f}. \quad (3.9)$$

For a fixed PCF radius $R_1 = 9.8 \mu\text{m}$, $\lambda = 532 \text{ nm}$ and $f = 100 \text{ mm}$, the SRW profile was plotted using Equation 3.8 for $\eta = 0.2, 0.4$ and 0.627 over the output aperture. Figure 3.5 shows the normalized SRW amplitude as a function of the radial distance normalized to the input aperture radius. As shown in the plots, the SRW starts to deviate from a flat profile for larger η values, i.e. the PCF is larger than the main lobe of the Airy profile. For phase imaging, it is necessary to have a negligible curvature of the SRW profile over the imaged aperture to avoid distortions in the output interferogram. This can be achieved by using small η values (i.e. $\eta = 0.2$), but it comes at the expense of the fringe visibility. A good trade-off between the flatness and the magnitude of the SRW can be achieved using $\eta \leq 0.627$. It should be noted, however, that the curvature is negligible only in the central region, which limits the effective field-of-view of the system where phase imaging or measurement is accurate. For $\eta \leq 0.627$,

$$g(r') = 1 - J_0(1.22\pi\eta) \quad (3.10)$$

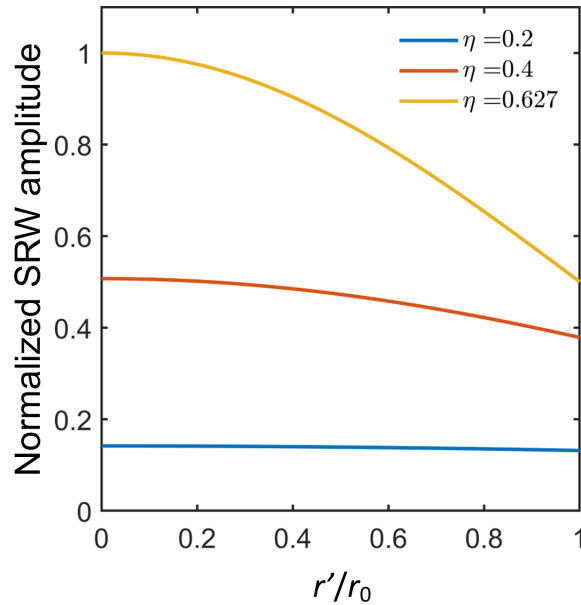


Figure 3.5: SRW spatial profile over the output aperture normalized to the input aperture radius for $\eta = 0.2, 0.4$ and 0.627 .

3.4 OAM characterization of optical twisters

Up to this point, we have not yet considered an incoming HCB. For the purpose of showing that the CPI output in fact contains information about the beam's topological charge, we will focus on the case of optical twisters ($K = 0$):

$$u(r, \phi) = \text{circ}\left(\frac{r}{r_0}\right) e^{-il\phi\frac{r}{r_0}}. \quad (3.11)$$

From Equation 3.7, the normalized zero-order is given by

$$\begin{aligned} \alpha &= \frac{1}{\pi r_0^2} \int_0^{2\pi} \int_0^{r_0} e^{-il\phi\frac{r}{r_0}} r dr d\phi \\ \alpha &= \frac{1 - e^{-2\pi il} - 2\pi il}{2\pi^2 l^2} \\ \alpha &= -\frac{i}{\pi l} \text{ for } l \in \mathbb{Z} \end{aligned} \quad (3.12)$$

Equation 3.12 implies that a significant amount of light is deflected towards the center in the Fourier plane for small values of l , which is what we exploited for charge determination. It further shows that the magnitude of the focused light $|\alpha|$ decreases as the topological charge increases consistent with the results presented in [58]. Since the reference wave is synthesized based on phase-shifting the central region around the zero-order, Equation 3.12 indicates that the magnitude of the SRW tend to decrease with l . The relationship specified in Equation 3.12 was verified numerically by Fourier transformation of a simulated HCB complex field profile, and Figure 3.6 shows exact fitting between the analytic and the numerical $|\alpha|$.

In the experiments, the input aperture radius can be adjusted to achieve $\eta = 0.627$ for a fixed PCF radius, which matches the PCF to the main lobe of the Airy profile, which reduces the SRW magnitude to $g(r' \in \text{central region}) \approx 1$. Using Equations 3.6, 3.8 and 3.12, the CPI output intensity can then be expressed for $\theta = \pi$,

$$I(r') = 1 + \frac{4}{\pi^2 l^2} + \frac{4}{\pi l} \cos\left(l\phi\frac{r'}{r_0}\right) \quad (3.13)$$

Equation 3.13 describes the presence of interference fringes that modulate with both the radial and

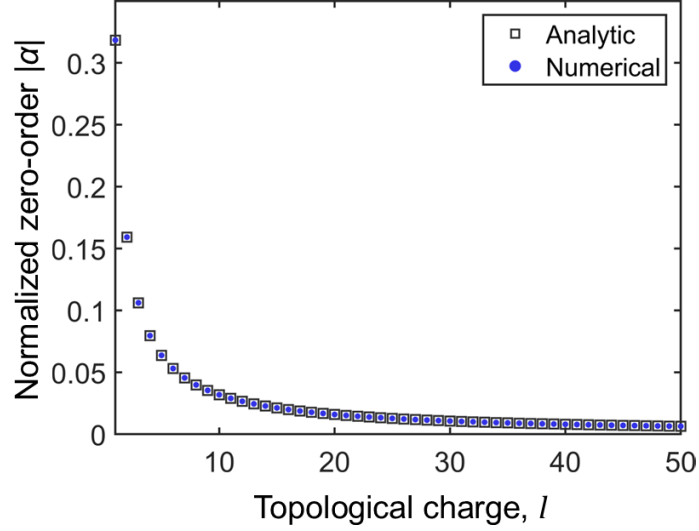


Figure 3.6: Normalized zero-order of HCBs ($K = 0$) for different topological charges obtained from Equation 3.12 and from numerical simulations.

azimuthal positions, and that $I(r')$ contains information about both the sign and the magnitude of l . The appearance of the phase term of optical twisters in the intensity distribution indicates the direct conversion of the HCB's phase into the CPI output intensity. Figures 3.7 and 3.8 show the intensity distributions described by Equation 3.13 for increasing l and for positive and negative helicity. As shown in both figures, the topological charge can be determined by counting the number of interference fringes. However, as the charge increases, the fringe contrast degrades making it difficult to employ this method. This can be traced back to the decreasing strength of the zero-order that is available to synthesize the reference wave. With higher l , the imaged object field in Equation 3.13 overpowers the SRW resulting in the reduced fringe contrast. From the intensity equation, the quality of the interference fringes can be quantified by the visibility defined as

$$\text{Visibility} = \frac{I_{\max} + I_{\min}}{I_{\max} - I_{\min}} \quad (3.14)$$

$$= \frac{4\pi l}{4 + \pi^2 l^2} \quad (3.15)$$

Figure 3.9 shows the plot of Equation 3.15 and the measured contrast in the numerically obtained CPI outputs, where close matching between the graphs is observed.

It should be noted that in the previous discussions, the far-field intensity distribution of HCBs deviate from an Airy profile, which was an assumption made to approximate the SRW. However,

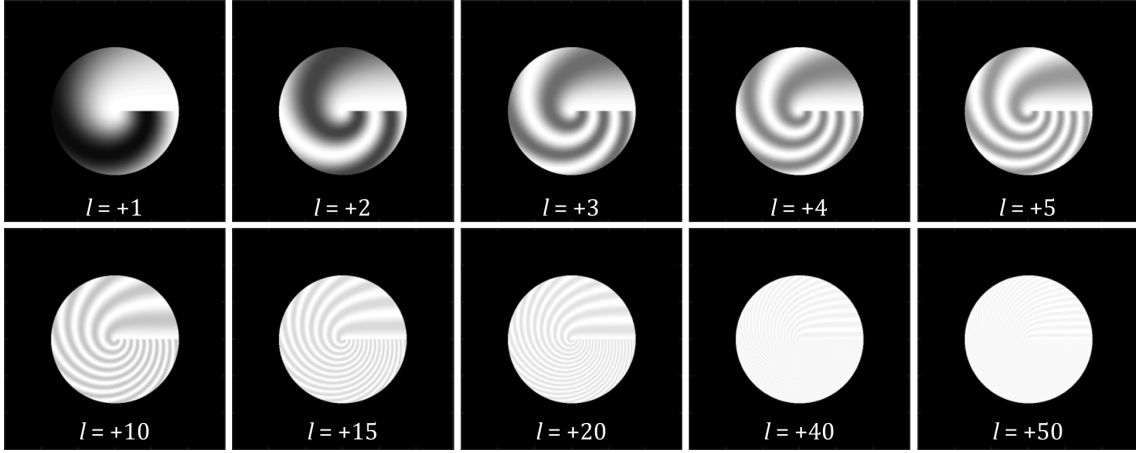


Figure 3.7: Analytic CPI intensity output for HCBs ($K = 0$) with positive topological charges.

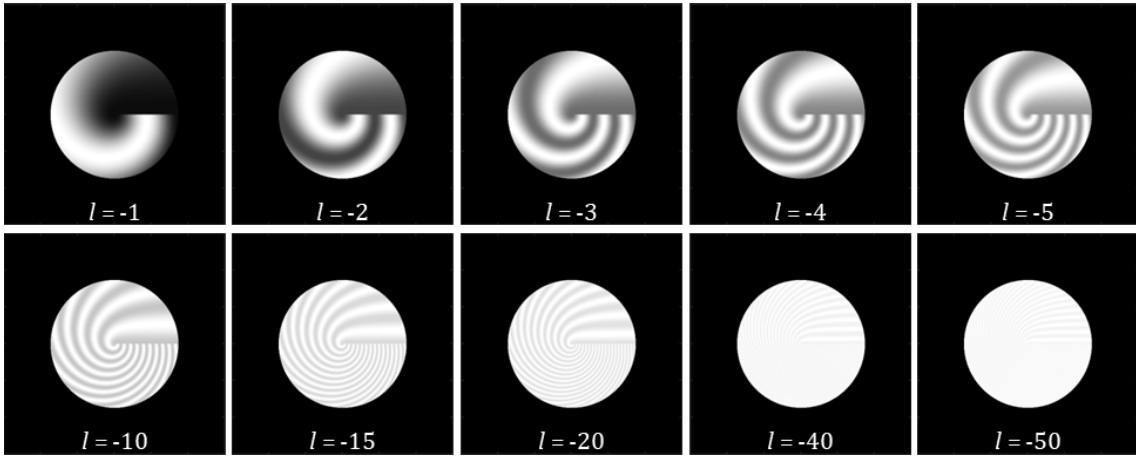


Figure 3.8: Analytic CPI intensity output for HCBs ($K = 0$) with negative topological charges.

to gain a simplistic model of the intensity output of the CPI, it was necessary to impose such assumption. In a real system, the problem is posed as an incoming HCB with a priori information about the system parameters, but not the beam's charge or helicity. Optical experiments were performed to demonstrate the interferometry-based charge detection of HCBs.

Optical experiments

Figure 3.10 shows the optical setup to detect HCB. To test our proposed scheme, HCBs were generated using the expanded Gaussian output of a 532-nm diode laser impinging on an SLM (Hamamatsu, $12.5 \mu\text{m}$ pixel pitch), where the HCB phase function is displayed. The reflected beam carries the HCB phase profile and passes through the CPI configuration. The focal length of the lenses used to construct the CPI is 100 mm, and the output is detected by a CMOS camera (Basler, $5.86 \mu\text{m}$ pixel size). The PCF introduces a π phase-shift and its radius is $9.8 \mu\text{m}$. The alignment process of the PCF was carried out by observing the intensity pattern on the camera in

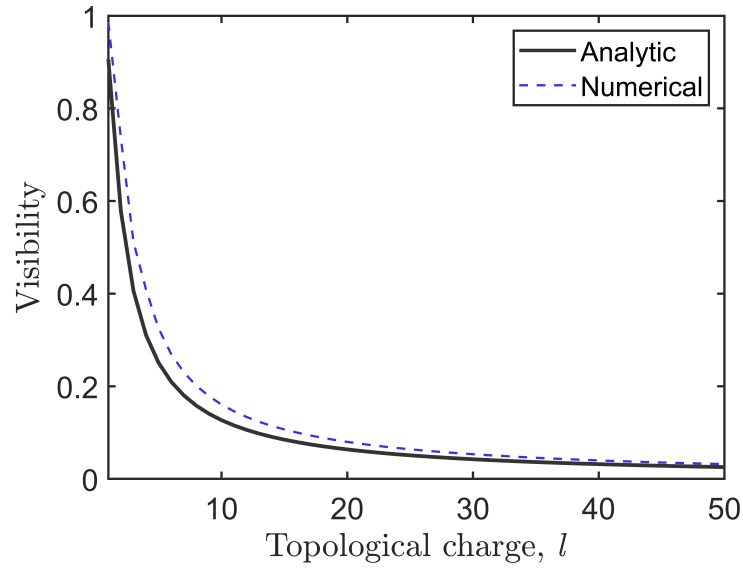


Figure 3.9: **Fringe contrast.** Visibility of the interference fringes from the CPI output as the topological charge is increased obtained by calculating the contrast of the CPI output (dashed line) and by plotting the analytic expression (solid line).

the absence of an encoded phase on the SLM. It was shown previously that a dark central core surrounded by a halo of intensity that decreases radially outwards can be produced for $\eta = 0.4$ [61]. This was exploited to ascertain that the PCF is correctly positioned, and was achieved by setting the input aperture radius to $r_0 = 1.3$ mm. With the optimally aligned PCF, the aperture size was then adjusted to $r_0 = 2.1$ mm to set $\eta = 0.627$, and the CPI was ready to use for HCB charge detection.

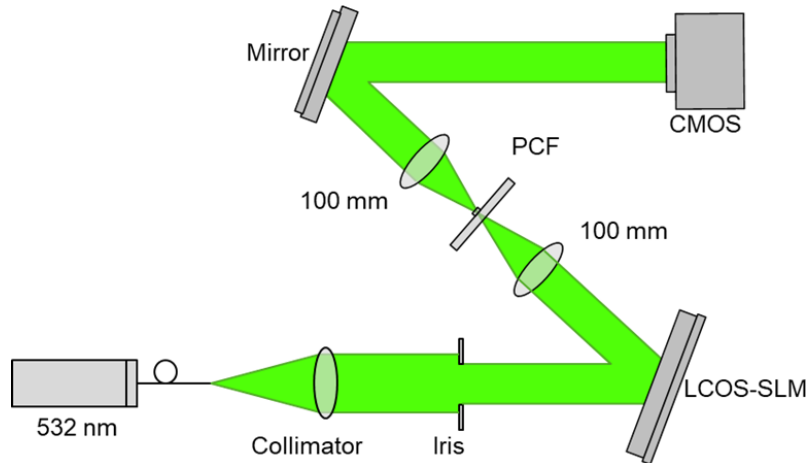


Figure 3.10: **Experimental setup for HCB detection.** The Gaussian output of a 532-nm diode laser is first expanded and then imprinted with the HCB phase profile using an LCOS-SLM (Hamamatsu). The outgoing beam carries the helico-conical phase and is then incident on the CPI for topological charge detection. The output of the CPI is imaged using a CCD camera. The focal length of the lenses is 100 mm.

Figure 3.11 shows the phase-imaged HCBs for $K = 0$ and for increasing l 's. Visual inspection of the boxed region reveals that the number of fringes matches the HCB topological charge. Given the good output visibility, a simple image post-processing can be implemented to count the fringes. As shown in Figure 3.12 for $l = 10, 15$ and 20 , scans of the relevant region shows that the count is consistent with the charge for up to $l = 20$. For higher l 's, the fringe visibility degrades and it becomes difficult to determine the charge based on this method.

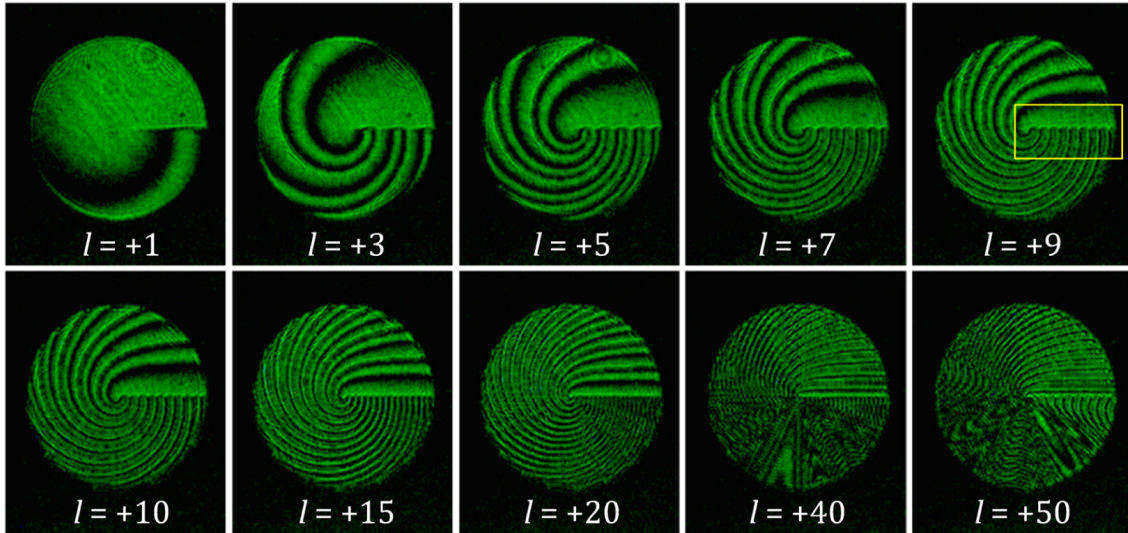


Figure 3.11: **CPI experimental intensity output.** Interference fringes obtained from the CPI for HCBs ($K=0$) with increasing topological charge.

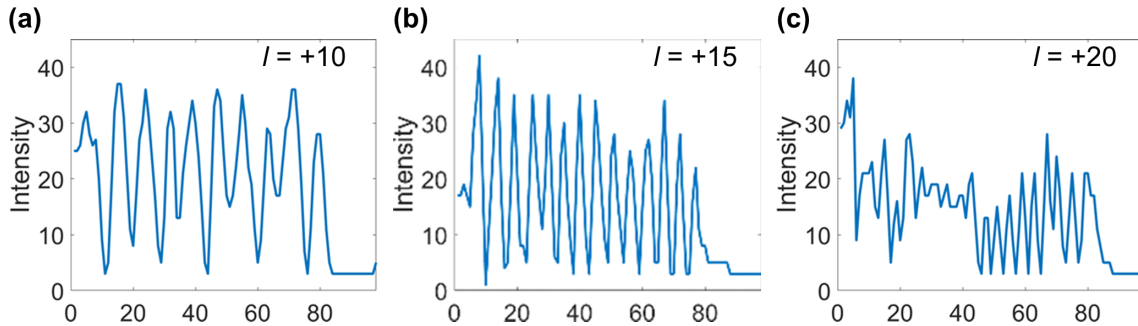


Figure 3.12: **Intensity line profiles.** CPI intensity line scans for $l = +10, +15$ and $+20$.

We also examined the output when the helicity of the beam is reversed. Figure 3.13 shows the images obtained from the CPI for HCBs with $l = \pm 1, \pm 2, \pm 4, \pm 10$ and ± 15 . As described by third term of Equation 3.13, the sign of the charge manifests in the output. This is also observed experimentally. From the analytic description, the intensity in the $\phi = 0$ region is maximum when l is positive and minimum when l is negative. This is supported by the experiments as shown in the top and bottom rows of Figure 3.13 for positive and negative l 's, respectively. By observing,

therefore, the intensity along the $\phi = 0$ region, we can determine both the charge magnitude and helicity of the incoming HCB.

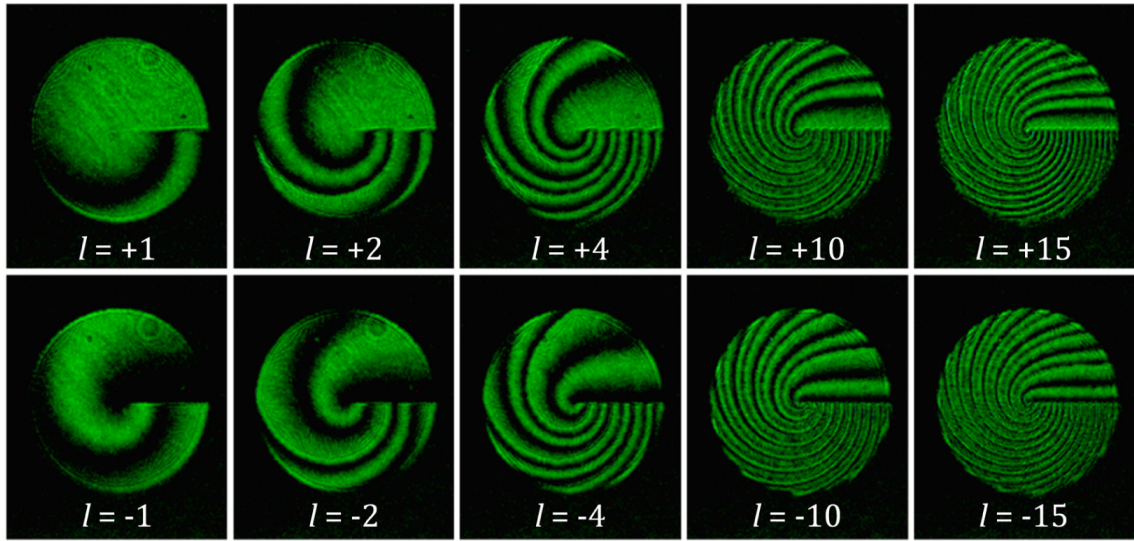


Figure 3.13: **Helicity dependence of the CPI output.** (Top row) Positively and (bottom row) negatively charged HCBs ($K=0$) acquired experimentally. The sign manifests in the outputs as maximum and minimum when the charge is positive and negative, respectively.

Finally, the same CPI setup was employed to image HCBs with $K = 1$ and $K = \frac{1}{2}$. Figure 3.14 shows the CPI intensity outputs for select topological charges, revealing that it is also possible to phase-image these types of HCBs, albeit a much stricter condition to determine the actual magnitude and helicity of the beam.

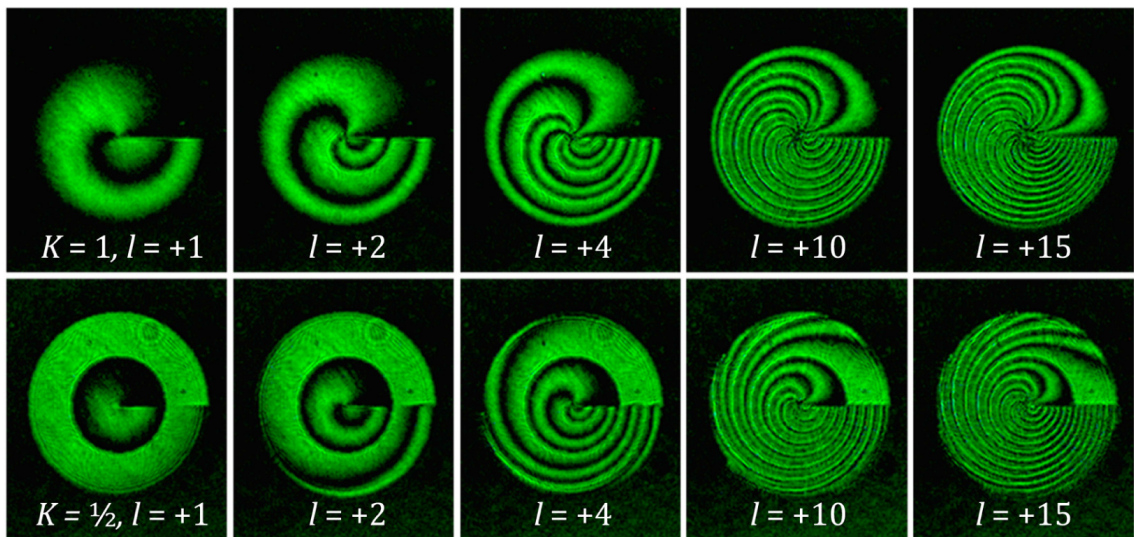


Figure 3.14: Analytic CPI intensity output for HCBs ($K = 0$) with positive topological charges.

For the optical twisters, several parameters in the CPI setup can be tweaked. The visibility can be enhanced by increasing the magnitude of the SRW. This can be implemented, for example, with the

use of a dynamic PCF (i.e. by using an SLM [62]), A can be adjusted to obtain matched amplitude. However, this presents a drawback in terms of losses incurred in the system.

3.5 Summary

To summarize this chapter, a common-path interferometer was constructed to determine the topological charge (both magnitude and helicity) of helico-conical beams, specifically the so-called optical twisters. Here, a π phase-shifting refractive element is placed at the Fourier plane of the $4f$ setup comprising the CPI to synthesize a reference wave that interferes with the scattered object wave. An analytic model was presented showing that the phase distribution of the HCB ($K = 0$) converts into the CPI intensity output, allowing the determination of the HCB topological charge magnitude and sign.

In the next chapter, a similar $4f$ configuration but with a different phase filter at the Fourier plane is shown to enhance the performance of a nonlinear imaging system. Such a system becomes highly beneficial when directly imaging mid-infrared sources that are dwarfed by a close and more intense source.

4 High-contrast nonlinear imaging using an optical vortex

4.1 Introduction

The use of optical vortices is an established approach that is known to enhance the performance of imaging systems. In microscopy, for example, an optical vortex can facilitate contrast enhancement of weakly absorbing or scattering samples by highlighting their edges isotropically [63, 64]. The vortex in this case is employed as an optical Fourier filter that introduces spatially-dependent phase shifts onto the Fourier components of an incoming field. In such a setup, the complex field at the $4f$ output is the far-field of the optical vortex convoluted with every image point. The azimuthally dependent phase profile of the optical vortex results in the destructive interference of the fields in adjacent points over a uniform area. Meanwhile, in nonuniform regions (i.e. amplitude or phase edges of the image), the fields in adjacent points do not completely interfere destructively, resulting in intensity maxima at these points. Edge-enhancement of a macroscopic object (i.e. circular aperture) was first demonstrated by K. Crabtree et al in 2004 [63], and thereafter, applied in microscopy by the group of Ritsch-Marte [64]. Since then, the technique has become known as spiral phase contrast (SPC), an alternative modality to dark-field and phase-contrast microscopy.

Optical vortex coronagraphy (OVC), while not entirely different, is a separate field that employs the same concept and was proposed in the same year that SPC was first reported [65, 66]. While SPC deals with small objects, an optical vortex coronagraph aims to directly image large ones - exoplanets. In general, the challenge is posed as detecting a dim scatterer that is illuminated or overwhelmed by a much brighter light source. Such is the case in the direct imaging of exoplanets orbiting their parent stars. Owing to the ability to image dim objects under these situations, the technique has also been termed as *high-contrast imaging*. In exoplanet imaging, the challenge comes from the large flux ratio between the planet and its parent star, which is further complicated by their close angular proximity to each other. In this type of situation, using physical stops, such as those used in amplitude-type coronagraphs, is disadvantageous because of the possibility to block light coming from the stellar companion. Along with other types of phase-based techniques, OVC

provides an advantage over amplitude-type coronagraphs as it allows starlight attenuation while having minimal effect on the weaker source even for small angular separations.

One crucial part in OVC is the fabrication of the employed vortex mask (VM). In general, a VM can be grouped into either a scalar [66–68] or a vector VM [65]. Probably the most direct way of generating an optical vortex is by the use of a scalar VM (i.e. a spiral phase plate), which imprints the helical phase onto the beam by azimuthal variation in its optical thickness. On the other hand, a vector VM relies on polarization manipulation and has been fabricated with the use of, for example, liquid crystal polymer (LCP) half-wave plates or with masks based on form birefringence [65, 69, 70]. Achromatic masks for both scalar and vector VMs can be fabricated by multilayer or tailored designs, but even with the technological advancements in terms of fabrication, such structures can still be difficult to achieve [70–72].

In the optical region, a contrast requirement of 10^9 is needed to identify a Jupiter-like planet located 1 AU from its star, where 1 AU is the distance between the earth and the sun. Compounded by atmospheric turbulence, such a contrast ratio can be challenging to achieve for Earth-based telescopes. In the infrared region, there is more favorable star-planet flux ratio and the contrast requirement is relaxed to 10^6 , owing to the heating and re-radiation of longer wavelengths by the planet [73, 74]. Additionally, the near-infrared (NIR) and mid-infrared (MIR) domains are also two of the key spectral regions of interest as they allow for the determination of a planet's atmosphere composition. While imaging in the infrared region may have more favorable conditions, there is still a need for achromatic VMs and MIR cameras with sophisticated cooling systems.

In the following work, a nonlinear optical vortex coronagraph (n-OVC) is proposed. By exploiting angular momentum conservation in a sum-frequency generation (SFG) process, the proposed n-OVC has the following valuable properties: (1) spectral translation, which enables the VM to operate only at one fixed (pump) wavelength, (2) tunability to signal center wavelength, and (3) achromatic operation without the need for an achromatic VM. While our laboratory demonstration focuses on the NIR, an n-OVC extended to MIR will circumvent the need for both achromatic MIR VM and MIR camera (e.g. MCT array).

4.2 Mathematical model

Figure 4.1 shows the phase profiles of two optical vortices corresponding to LG beams with topological charges $l = 1$ and $l = 2$. In the original paper of Foo et. al, they compared optical vortices with different topological charges ($l = 1, 2, 3$) and found that $l = 2$ had the superior performance [66]. In this work, we also employed the same optical vortex.

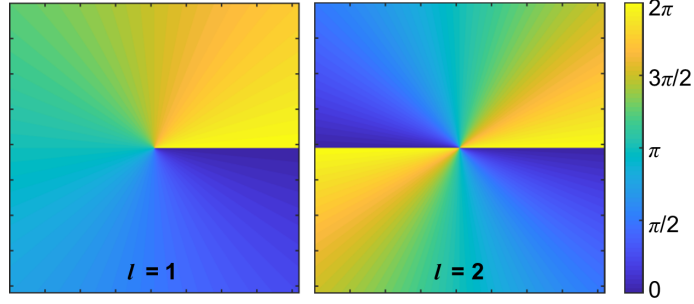


Figure 4.1: **Phase distribution of LG beams for $l = 1$ and $l = 2$.**

The optical setup for the nonlinear optical vortex coronagraph (nOVC) is shown in Figure 4.2 along with the conventional OVC. The linear OVC in Figure 4.2(a) consists of a circular entrance aperture of radius r_0 , which forms an Airy profile at the back-focal plane of the lens L_1 . The optical vortex placed at the Fourier plane has a transmission function given by

$$H(\rho, \phi) = \exp(il\phi) \quad (4.1)$$

where l is the topological charge of the optical vortex, (ρ, ϕ) are the polar coordinates in the Fourier plane and $l\phi$ is the helical phase profile introduced by the vortex. The output field of the OVC system at the pupil plane can then be expressed as

$$E_{\text{OVC}}(r, \theta) = \mathfrak{F}^{-1} \left\{ \mathfrak{F} \left\{ \text{circ} \left(\frac{r'}{r_0} \right) \right\} \cdot \exp(il\phi) \right\}. \quad (4.2)$$

Here, (r, θ) are the polar coordinates at the pupil plane and $\text{circ} \left(\frac{r'}{r_0} \right)$ represents the circular input aperture defined as unity for radius $r' < r_0$ and null otherwise. For $l = 2$, the resulting field reduces to [65, 66]

$$E(r, \theta)_{\text{OVC}} = \begin{cases} 0 & r < R' \\ E_1 \exp(i2\theta) \cdot \left(\frac{R'}{r}\right)^2 & r > R' \end{cases} \quad (4.3)$$

where $R' = \frac{f_2}{f_1} r_0$ is the radius of the pupil plane image of the input aperture. Equation (4.3) means that for an on-axis source, the optical vortex acts to diffract all light outside the imaged aperture. The corresponding intensity profile would appear as a dark central core surrounded by a bright ring of radius R' , after which, the irradiance decreases radially outwards. Figure 4.2(c) shows the simulated intensity profile at the pupil of a linear OVC for $l = 2$. By adding a truncating aperture (called Lyot stop) with radius $R_{\text{Lyot}} < R'$ at the pupil plane, the bright halo intensity can be attenuated. The lens L_3 finally produces an image of the dimmed, if not annihilated, on-axis source. An incoherent off-axis point source eludes the center of the optical vortex; hence it is transmitted with less effect from the vortex, resulting in negligible attenuation at the coronagraphic image plane.

The proposed nonlinear optical vortex coronagraph (n-OVC) in Figure 4.2(b) employs the SFG process of two beams facilitated by a nonlinear crystal. The n-OVC architecture is comprised of a signal beam through a $4f$ setup (L_1 and L_2), and a top-hat illuminated optical vortex ($l = 2$) pump beam that interact nonlinearly in a periodically poled lithium niobate (PPLN) crystal. Similar to OVC, the path of the signal beam (red rays in Figure 4.2) consists of an entrance aperture characterized by its radius r_0 and can be represented as

$$E_s(r, \theta) = \text{circ}\left(\frac{r}{r_0}\right) \quad (4.4)$$

The lens L_1 focuses E_s onto the center of the PPLN crystal, where it interacts with the pump beam E_p , which is an imaged $l = 2$ optical vortex through L_4 and L_5 and is given by

$$E_p(\rho, \phi, z = 0) = \text{circ}\left(\frac{\rho}{\rho_0}\right) \exp(i2\phi) \quad (4.5)$$

with $z = 0$ defined at the center of the PPLN crystal. The lens L_2 collimates (through a band-pass filter) the upconverted beam E_{up} which has a spatial profile that closely resembles that of its linear counterpart. The Lyot stop and lens L_3 facilitate the formation of the final n-OVC output. By

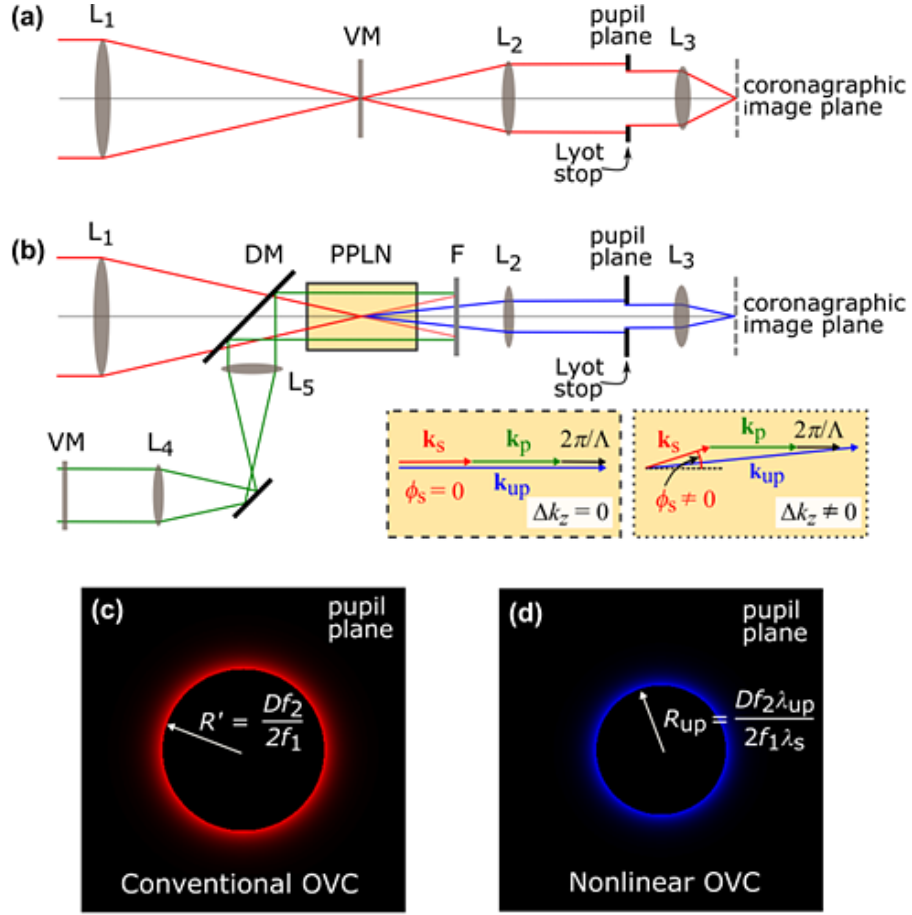


Figure 4.2: **Nonlinear optical vortex coronagraph**. Schematic diagram of (a) a linear OVC and (b) the proposed n-OVC. In the n-OVC, the signal beam (red lines) is mixed with a vortex-shaped pump beam (green lines) in the nonlinear PPLN crystal. With such a process, the coronagraphic and off-axis images are produced at the SFG wavelength (blue lines). The two insets in (b) illustrate the phase match (Δk) dependence on the angular direction ϕ_s of the input signal k -vector. (c, d) Calculated intensity distributions at the respective pupil planes of the two coronagraphs. $L_1 - L_5$, lenses; DM, dichroic mirror; F, spectral filters that only allows SFG beam.

conservation of energy, the angular frequency of the upconverted field should be the sum of the angular frequencies of the two input fields. Equivalently, the upconverted field will have a wavelength that follows $1/\lambda_{up} = 1/\lambda_p + 1/\lambda_s$, where λ_p and λ_s are the pump and signal wavelengths, respectively. The mathematical model of the n-OVC follows the theory of upconversion imaging, which can be treated similar to scalar diffraction theory as discussed by A. Barh et al. in [75]. In this mathematical treatment, the overall transfer function of the system is proportional to the spatial profile of the shaped pump beam at the center of the PPLN crystal. Borrowing the tools in Fourier optics (scalar diffraction theory), the upconverted field of the n-OVC for arbitrary l can be expressed as

$$E_{\text{n-OVC}}(r, \theta) \propto \left[\mathfrak{F}^{-1} \left\{ \mathfrak{F} \left\{ \text{circ} \left(\frac{r}{r_0} \right) \cdot \exp(il\phi) \right\} \right\} \otimes F(r, \theta) \right] \cdot \text{sinc} \left(\frac{\Delta k_z(\phi_s)L}{2} \right) \quad (4.6)$$

where \otimes denotes the convolution operator. Here, $F(r, \theta)$ is the Fourier transform of an apodizing filter that defines the truncating effects the finite width of the PPLN crystal or the pump radius. $F(r, \theta)$ can be approximated as a delta-function when the Airy profile formed by E_s is contained well within the crystal cross-section. The $\text{sinc}(\Delta k_z(\phi_s)L/2)$ arises from the phase matching of the upconversion process, where $\Delta k_z(\phi_s, \Lambda, T) = k_{\text{up}} - k_{\text{p}} - k_{\text{s}} - 2\pi/\Lambda + k_{\text{s}}(1 - k_{\text{s}}/k_{\text{up}})\phi_s^2$, $k_j = k_j(T)$ (subscript $j = \text{s, p or up}$ denotes signal, pump and upconverted field, respectively and T is the PPLN temperature) are the collinear k -vector magnitudes inside the PPLN crystal with poling period Λ . The internal angle ϕ_s refers to the angular direction of the input signal k -vector relative to the z axis [see insets in Figure 4.2(b)]. By proper combination of the PPLN crystal's poling period and temperature, the phase match condition can be achieved for normal k_s vectors, i.e. $\Delta k_z(\phi = 0) = 0$ that corresponds to maximum conversion efficiency, $\eta = \eta_0$. For $\phi_s \neq 0$, η deviates from the maximum value due to the phase mismatch ($\Delta k_z(\phi_s \neq 0) \neq 0$) and the efficiency follows the $\text{sinc}(\Delta k_z(\phi_s)L/2)$ distribution. Equation 4.6 implies that in the SFG process, the total angular momentum is conserved between the input and the output fields, with the upconverted field inheriting the OAM of the pump beam. This phenomenon has been demonstrated before in [76, 77] and exploited for edge enhancement in nonlinear imaging [78, 79].

For $l = 2$, Equation 4.6 simplifies to $E_{\text{n-OVC}} = 0$ inside a circle with radius $r < R_{\text{up}}$. For $r > R_{\text{up}}$,

$$E_{\text{n-OVC}}(r, \theta) \propto \exp(i2\theta) \cdot \left(\frac{R_{\text{up}}}{r} \right)^2 \cdot \text{sinc} \left(\frac{\Delta k_z(\phi_s)L}{2} \right) \quad (4.7)$$

where $R_{\text{up}} = r_0 \frac{f_2}{f_1} \frac{\lambda_{\text{up}}}{\lambda_{\text{s}}}$ is the radius of the upconverted image of the signal entrance aperture. The term $\frac{f_2}{f_1}$ comes from the standard magnification factor in a $4f$ setup, while $\frac{\lambda_{\text{up}}}{\lambda_{\text{s}}}$ is due to the upconversion process. Comparing Equations 4.3 and 4.7, the output of a nonlinear OVC is similar to that of the linear OVC apart from an added magnification factor and a masking function brought by the upconversion process. Note that the effect of $F(r, \theta)$ can be included but has been dropped with the assumption that the relative size of the Airy profile is smaller than the crystal aperture.

Unsurprisingly from this model, the n-OVC therefore also has a halo intensity output as shown in Figure 4.2(d). Importantly, it should be pointed out that the sinc-squared modulation should have an envelope whose main lobe is larger than the halo ring. Otherwise, such a modulation will behave as a smaller Lyot stop, which then reduces the overall efficiency and increasing the inner working angle (IWA) of the n-OVC.

4.3 Laboratory demonstration of a nonlinear optical vortex coronagraph

4.3.1 Optical setup

The n-OVC is experimentally demonstrated using the setup in Figure 4.2(b). The pump and signal wavelengths are $\lambda_p = 1064$ nm and $\lambda_s = 1575$ nm, respectively. The signal beam, which has a collimated Gaussian profile with beam waist $w_s = 1$ mm, is incident on the entrance aperture with diameter $D = 1$ mm. The pump beam, on the other hand, is first expanded (not shown in the figure) then demagnified by L_4 and L_5 so that its waist is $w_0 = 1$ mm in the PPLN crystal. The PPLN crystal's length is $L = 10$ mm, its cross-section is 1×1 mm² and poling period is $\Lambda = 11.8$ μ m. To achieve collinear phase matching, that is $\Delta k_z(\phi_s = 0) = 0$, the PPLN temperature is set to $T = 130^\circ\text{C}$. The focal lengths of the lenses used are $f_1 = f_5 = 60$ mm, $f_2 = 200$ mm, $f_3 = 250$ mm and $f_4 = 300$ mm. The optical vortex (OV) is sandwiched between two quarter-wave plates - the first to generate a circularly polarized illumination on the OV and the second to transform back to linear polarization. The OV is made of spatially varying half-wave plate (SVHWP) that is based on LCP. For this vortex mask, a central defect arises from the failure of the LCP molecules to follow the right orientation at the central region [80–82]. As such, the vortex mask fails to perfectly imprint the helical phase into the pump and consequently the SFG beam. This central disorientation, along with other aberrations in the optical system, results in the imperfect nulling of light inside the halo intensity for the SFG beam. To minimize this, the relative size of the defect should be made smaller than the central lobe of the Airy disk [80, 82]. A silicon-based camera is used to record the n-OVC output.

4.3.2 Numerical simulation and experimental verification

Numerical simulations were implemented using fast Fourier transform (FFT)-based calculations in Matlab. The finite extent of the nonlinear crystal was taken into account, and all other parameters matched those in the experiments. For $\lambda_s = 1575$ nm, the intensities obtained numerically and experimentally at the pupil plane are illustrated in Figure 4.3, showing good qualitative agreement. The blurring of the halo images for both simulation and experiment comes mainly from the truncating width of the nonlinear crystal. For the latter, other factors such as slight misalignment or the presence of impurities (i.e. dust) in the setup contribute to both blurring and incomplete nulling of the inner region of the halo. Aside from utilizing a larger nonlinear crystal, the blurring can be alleviated by adjusting the size of the Airy profile to increase the number of rings that fit into the PPLN aperture. However, to minimize the relative size of the vortex central defect, which is usually in the micrometer range [82], the main lobe of the Airy profile was kept large, i.e. 115 μm .

4.3.3 Wavelength tunability and broadband operation

To demonstrate wavelength tunability of the n-OVC, we simulated a $\lambda_s = 1550$ nm signal beam for the same λ_p and Λ . The PPLN temperature was adjusted to satisfy phase match conditions, with $T = 40^\circ\text{C}$. The simulated output intensity is shown in Figure 4.3(c) which was also experimentally verified as shown in Figure 4.3(d). This demonstration indicates that the operational wavelength of the n-OVC can be actively tuned even with the use of a single monochromatic vortex mask. The implication of which is that, one can fabricate a monochromatic VM (i.e. for λ_p) with superior quality and can then extend its functionality to several signal wavelengths, albeit indirectly, using the n-OVC, provided the phase match condition can be achieved. Figure 4.4 shows a possible combination of parameters to achieve phase match condition for different signal wavelengths. In Figure 4.4(a), the temperature or PPLN period can be adjusted for a fixed pump wavelength $\lambda_p = 1064$ nm to achieve collinear phase match. The tuning effect by the pump wavelength is seen to be more pronounced in Figure 4.4(b) for a fixed PPLN period with $T = 180^\circ\text{C}$. Additionally, the bandwidth of the n-OVC for either $\lambda_s = 1575$ nm or $\lambda_s = 1550$ nm was measured to be about 1 nm, which is consistent with the acceptance bandwidth of the PPLN crystal. The bandwidth is determined by the full-width at half maximum of the main lobe of the $\text{sinc}^2(\Delta k_z L/2)$ as a function of the signal wavelength λ_s . Figure 4.5(a) shows the dependence of the upconversion

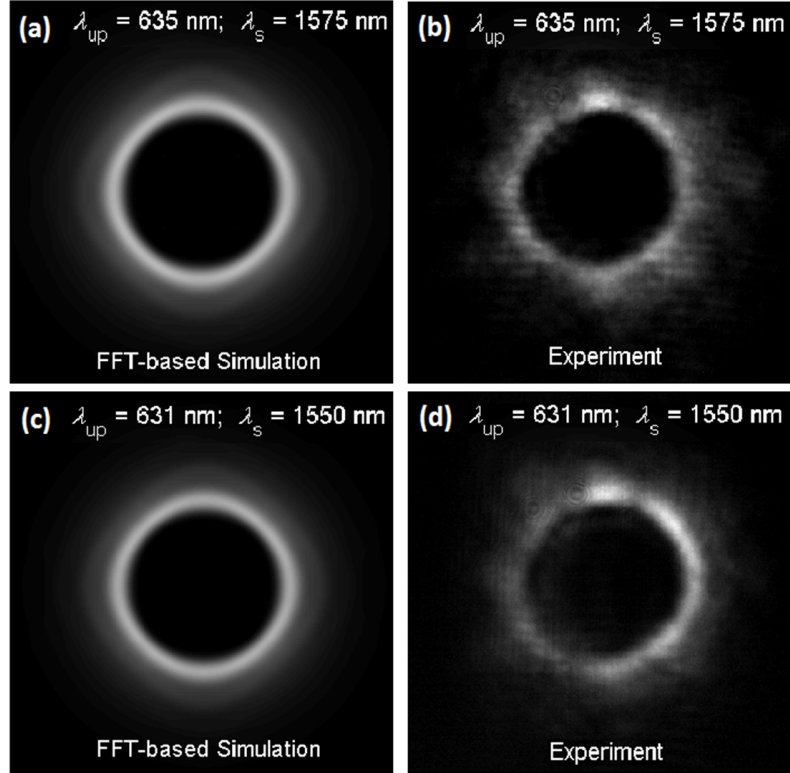


Figure 4.3: **Halo intensity outputs.** (a, c) Numerical and (b, d) experimental irradiance outputs of the n-OVC at the pupil plane for two signal wavelengths (a, b) $\lambda_s = 1575$ nm and (c, d) $\lambda = 1550$ nm. The blurred images are caused by the finite extent of the PPLN crystal aperture.

efficiency to Λ and λ_s . Figure 4.5(b, c) plot the normalized η for fixed PPLN periods $\Lambda = 11.8$ μm and $\Lambda = 23.0$ μm , respectively, showing the 1-nm bandwidth for the parameters using in our experiments. Meanwhile, by using a PPLN crystal with $\Lambda = 23.0$ μm the central wavelength can be tuned to the MIR region and at the same time achieve broadband operation with a FWHM of approximately 600 nm. By appropriate combination, therefore of Λ , T , λ_p and the nonlinear material comprising the crystal, both the central wavelength and bandwidth operation of the n-OVC can be adjusted.

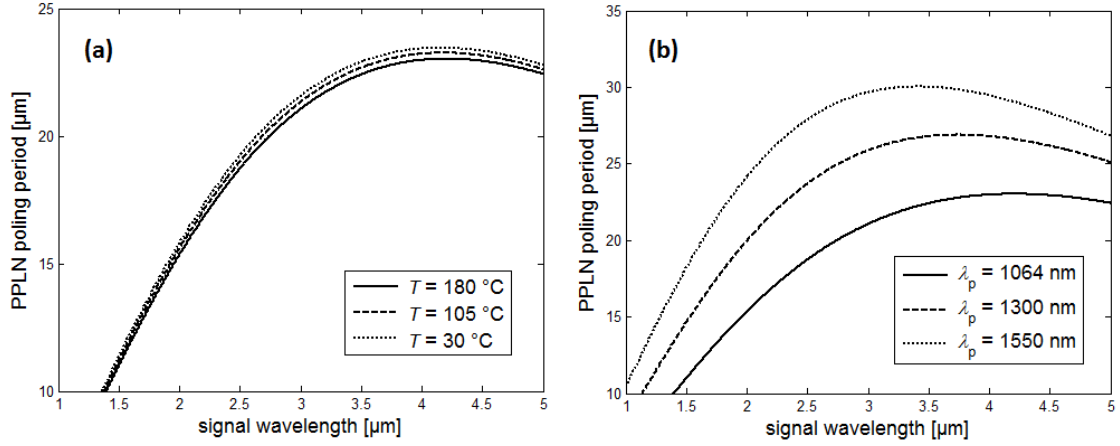


Figure 4.4: **Tunability of the signal central wavelength.** Phase-match curves showing the $\Lambda - \lambda_s$ combinations for which $\Delta k_z = 0$ can be achieved for (a) $\lambda_p = 1064$ nm and varying T , and for (b) $T = 180$ °C.

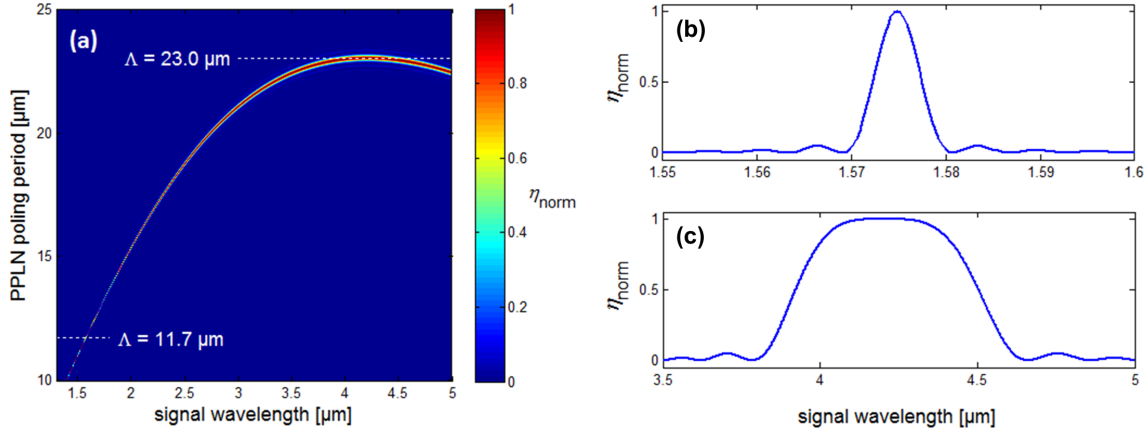


Figure 4.5: **Tunability of the n-OVC bandwidth.** Normalized upconversion efficiency as a function (a) of both the PPLN period and the signal wavelength, and (b, c) of only the signal wavelength for fixed PPLN periods (b) $\Lambda = 11.8$ μm and (c) $\Lambda = 23.0$ μm . For all plots, $\lambda_p = 1064$ nm, $T = 180$ °C and $L = 2.5$ mm are used.

4.3.4 n-OVC performance

To assess the performance of the proposed n-OVC, two commonly used metrics were employed: 1) peak-to-peak (PTP) attenuation and 2) intensity contrast. As the name suggests, PTP attenuation serves as a measure of the n-OVC's capability to attenuate on-axis sources. As the vortex is translated from the optimally aligned position, coronagraphic images are recorded. The PTP attenuation is defined as the ratio of the peak irradiance of such coronagraphic images to the peak of an off-axis image obtained with sufficient displacement of the vortex from the center. On the other hand, the intensity contrast measures the attenuation in the full coronagraphic image. It is

calculated by azimuthally averaging the intensity values from the center and normalizing it with respect to the peak of an off-axis coronagraphic image. Here, it should be noted that the increasing displacement of the vortex from the center is equivalent to an increasing angular displacement of the source. Therefore, in the measurements and in the presented data, vortex displacement is expressed in terms of the angular separation λ_s/D , where $D = 2r_0$ is the diameter of the entrance aperture.

To obtain the coronagraphic image, the upconverted field transmitted through a Lyot stop with $R_{\text{Lyot}} = 0.8R_{\text{up}}$ was focused through lens L_3 . Using a 14-bit camera, a series of images was recorded for three different exposure times to capture the intense and weak lobes in the output irradiance. To remove the electronic noise, a dark-median background was obtained for each exposure time while the upconverted light is blocked. A similar procedure was implemented for the off-axis images. The final coronagraphic (on-axis) and off-axis images were rendered after subtracting the dark-median background from the raw images and accounting for the exposure times used to record the images. These were then used for the PTP attenuation and intensity contrast analyses. Figure 4.6 shows the rendered coronagraphic and off-axis images from the n-OVC.

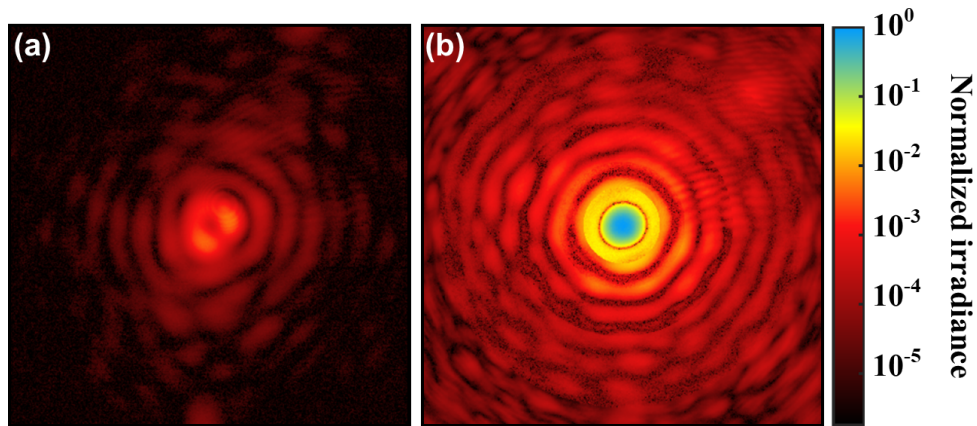


Figure 4.6: Rendered experimental on-axis and off-axis coronagraphic images from the n-OVC.

The PTP attenuation plots from both experiment and simulations are shown in Figure 4.7. From the experiments, a 6×10^{-3} attenuation is achieved with an optimally aligned optical vortex. The deviation between the experimental and numerical plots can be attributed to several factors including optical aberrations, tiny misalignments and the VM central defect. The effect of the central disorientation has been minimized in other studies using an amplitude stop. [80, 82] In our case, the relative size of the vortex defect was made to shrink by demagnification using lenses L_4 and L_5 . Nonetheless, with minimal aberrations in the setup and using a nonlinear crystal with larger

aperture, our simulations show that two orders of magnitude better attenuation can be realized with an n-OVC. The inner working angle (IWA) is another metric used in characterizing coronagraphs, which is arbitrarily defined as the 50% throughput angle. From the PTP plots, the current IWA of our n-OVC is $\text{sub-}\lambda/D$, similar to other coronagraphs that utilize vortex or phase-only masks.

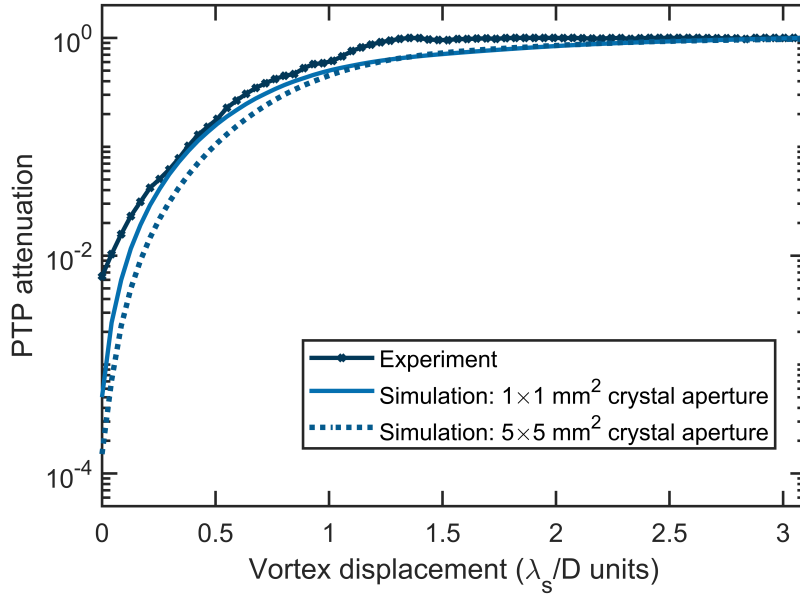


Figure 4.7: Peak-to-peak attenuation plots of the n-OVC obtained from numerical simulations and experiments.

The normalized irradiance profiles are plotted in Figure 4.8 for an optimally aligned VM ($\alpha = 0$) and a displaced VM with angular offset $\alpha = 3.2\lambda_s/D$. The subscripts “ex” and “si” correspond to the experimentally and numerically obtained coronagraphic images. The on-axis radial profile shows 10^{-3} contrast at $1.5\lambda_s/D$ and 10^{-4} at $3\lambda_s/D$. Comparing the experimental on-axis and off-axis plots (squared lines), the on-axis (i.e. starlight) is extinguished by four orders of magnitude compared to the off-axis at $3.1\lambda_s/D$. In other words, an off-axis source (i.e an exoplanet) appearing at the same angle will experience 10^{-4} less attenuation compared to the on-axis source (i.e. the parent star). A much higher intensity contrast can be achieved with a tophat signal pupil plane profile, $5 \times 5 \text{ mm}^2$ PPLN crystal aperture and a defect-free VM, which is the case numerically simulated in Figure 4.8.

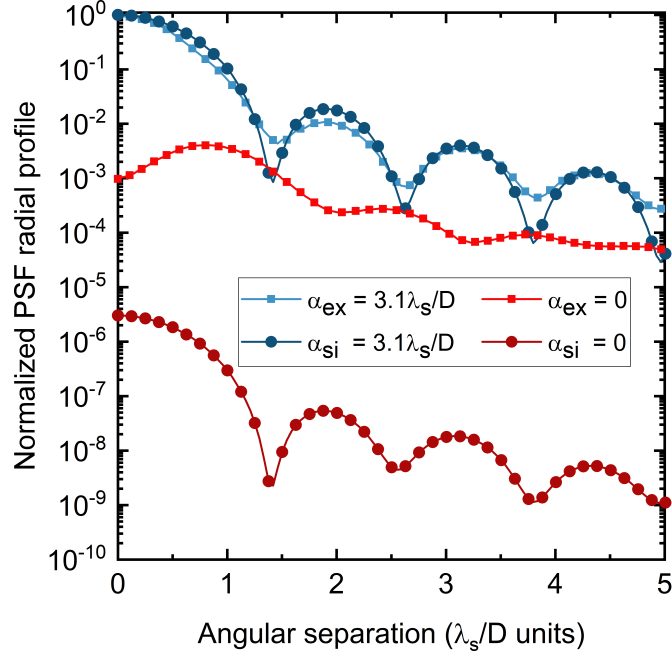


Figure 4.8: Azimuthally averaged radial profiles of the output PSF.

nOVC Sensitivity

The sensitivity of the n-OVC can be assessed using the conversion efficiency of the SFG process. For both pump and signal wavelengths, the Rayleigh range $\pi\omega_{0/s}^2/\lambda_{p/s}$ is much longer than the length of the PPLN crystal. Under this condition, paraxial approximation can be employed to calculate the conversion efficiency, which is given by [75, 83]

$$\eta = \frac{P_{\text{up}}\lambda_{\text{up}}}{P_{\text{s}}\lambda_{\text{s}}} = \frac{8\pi^2 d_{\text{eff}}^2 L^2 I_{\text{p}}}{\varepsilon_0 c n_{\text{s}} n_{\text{p}} n_{\text{up}} \lambda_{\text{up}} \lambda_{\text{s}}}. \quad (4.8)$$

Here, P_{up} and P_{s} are the upconverted and signal power, $d_{\text{eff}} = 14 \times 10^{-12}$ m/volt for MgO-doped PPLN crystal, I_{p} is the pump intensity, n_j is the refractive index of lithium niobate at wavelength λ_j , and ε_0 is the vacuum permittivity. In the n-OVC demonstration, a conversion efficiency of 2×10^{-5} was experimentally measured, which is in fair agreement with the theoretical value, $\eta = 3 \times 10^{-5}$ for $P_{\text{p}} = 1$ W. In principle, the conversion efficiency can be significantly improved by three approaches. The first strategy is straightforward, where the pump power can be increased to 10-100 W to significantly enhance η . Secondly, for modest pump powers, a smaller pump beam radius ω_0 can be employed to increase the pump power density. However, as modeled in Equation 4.6, smaller pump radius can serve as a truncating aperture that could further result in

halo blur and hence, reduce the n-OVC discovery space or the ability to image planets with larger angular separation from their parent star. Thirdly, the efficiency scales with L^2 . Using, therefore, a longer crystal will increase the upconversion efficiency. However, this could present penalties in both the signal acceptance bandwidth and signal acceptance angle. The former drawback has an obvious effect of degrading the broadband operation of the n-OVC. The latter has the potential consequence of broadening the image plane PSF, thereby increasing the IWA of the coronagraph. Using a combination of these approaches, an estimate of 0.2% upconversion efficiency can be achieved. With this, we estimate that an n-OVC for MIR operation that utilizes a low-noise silicon camera can readily compete with a conventional MIR OVC using state-of-the-art cryogenic cameras e.g., based on MCT detectors. In [84], it was found that even at 6% upconversion efficiency, a PPLN-based frequency converter combined with a silicon detector can achieve a sensitivity 50 times that of a cooled MCT detector.

4.4 Summary

In summary, a nonlinear optical vortex coronagraph was presented as an alternative to the conventional optical vortex coronagraph. Through the use of an optical vortex as a Fourier filter, high contrast nonlinear imaging was demonstrated. We claim that a vortex mask made for narrowband operation can be tuned to work for other wavelengths and even achieve a broadband operation.

5 Quantitative phase imaging using a polarization-dependent all-dielectric metasurface

5.1 Introduction

Quantitative phase imaging

Quantitative phase imaging (QPI) has emerged as a powerful tool for non-invasive inspection in optical metrology [85, 86], materials science [87] and microscopy [88, 89]. QPI is a collection of techniques that aims to recover the phase shifts that an incident light undergoes when it passes through a sample. Such phase shifts provide information about the light's optical path length that can be related to the structural components of the sample under observation. Due to the inherent insensitivity of current detectors to fast oscillations in the optical regime, direct phase measurement remains a challenge. QPI techniques therefore aim to convert the phase information of the sample into detectable intensity variations. In microscopy, QPI eliminates the need for chemical staining of weakly scattering or absorbing specimens, thus it enables the imaging of biological samples without risking to alter their natural behavior [89]. In optical metrology, QPI has been applied in wavefront aberration correction [90], defect detection in semiconductors [91] and materials characterization [87, 92, 93]. QPI can be generally grouped into 1) interferometric, and 2) non-interferometry-based or phase retrieval techniques.

Interferometric techniques remain the benchmark for phase measurement schemes, relying on the superposition of the object wave with a known reference wave. Included in this category are digital holographic microscopy [94], phase-shifting differential interference contrast microscopy [95, 96], and quadriwave lateral shearing interferometry [92, 97].

Alternatively, non-interferometric techniques enable phase reconstruction from recorded images of the diffracted object field without the need for a reference beam. As such, unlike two-beam interference strategies, non-interferometric approaches do not necessitate highly coherent source

and are less affected by optical aberrations and instability in the setup. In the phase reconstruction, the multiple intensity recordings are used in a constrained calculation based on, for example, different diffraction integrals [98, 99] or the transport-of-intensity equation (TIE) [100]. Non-interferometric techniques exploit phase-induced variation in the intensities such as, when light propagates, it gains additional phase shift that manifests in a change in the intensity. TIE-based phase reconstructions rely on this mechanism, with the TIE relating the axial intensity gradient to the phase of a complex field [100]. Experimentally, the axial intensity gradient can be estimated by finite-difference of two axially displaced images of the sample. The measurement scheme traditionally involves displacing the camera or the sample [101], which has restricted the application of TIE-based phase reconstruction to static objects. To extend the applicability of the technique to dynamic objects, a single-shot configuration was proposed in [102] by utilizing multiple optical components (i.e. an SLM, mirrors, lenses and a beam splitter). Two images were simultaneously captured by splitting the object wave into two and using an SLM to introduce the free-space propagation transfer function onto one of the beams. Such an architecture was implemented for the dynamic QPI of biological cells [102].

In this chapter, we exploit the multifunctional capability of metasurfaces targeted to facilitate the single-shot recording of two images for TIE-based phase reconstruction.

Metasurfaces

As the demand for compact, lightweight and efficient systems continues to rise, increasing focus has been put in searching and developing new alternative devices that do not only embody the aforementioned attributes but also exceed current standards, for example, in terms of multifunctionality. Like in many other disciplines, this has also been the trend in optics. The past two decades saw rapid advancements in miniaturized optical systems driven by demand from various fields ranging from medicine for accurate and rapid diagnostics to commercial technologies for integration in electronic gadgets. In the quest for such development, it has also pushed our understanding of fundamental phenomena that are being exploited to achieve the desired optical functionalities. While the theoretical foundations may have long existed, it is only recently that they start to be realized, thanks to the enormous progress in computation and nanofabrication technologies.

One of such advancements are metamaterials - artificial structures engineered in such a way to elicit responses that may not be found in nature. Metasurfaces are the planar counterparts of meta-

materials and are composed of subwavelength unit structures called meta-atoms [103]. By proper adjustment of the geometry of the meta-atoms, different properties of an incident optical wave can be tuned. Wavefront engineering has particularly benefited from metasurfaces due to the subwavelength arrangement of the meta-atoms, resulting in the suppression of higher diffraction orders - a persistent problem in traditional diffractive optical elements [44]. Additionally, the substantially reduced overall size of metasurfaces make them favorable for integration in compact optical setups. Perhaps one of the most exciting new capabilities of these ultra-thin components is the ability of a single metasurface to achieve complex functionalities that would otherwise require a combination of bulky optical components [37, 38, 44]. As such, metasurfaces have found applications in beam focusing [104–106], beam deflection [107–110], and holography [111, 112]. Multifunctional optical devices based on metasurfaces have been reported including independent wavefront control of orthogonal polarization components of an incident wave [37, 42, 113]. Tailored design of metasurfaces have also been recently shown to improve imaging performance [114] facilitating resolution [115, 116] and contrast enhancements [96, 117–121].

5.2 All-dielectric metasurfaces

Having more favorable optical properties over their metallic counterparts, all-dielectric materials have gained traction as constituting materials for metasurfaces. All-dielectric materials can lead to more efficient metasurfaces due to the lower absorption losses that an optical wave incurs as it passes through the material. To achieve $0-2\pi$ phase modulation, several mechanisms can be employed. Among these is the use of high-index dielectric nanopillars as meta-atoms to impart the propagation or dynamic phase, as introduced in Section 2.3.2. The substantial difference between the refractive indices of the dielectric and the medium results in field confinement within the high-index dielectric [42, 43, 108]. Each nanopillar acts as a truncated waveguide that can support several modes. Few studies have dug into describing the exact physical mechanism behind this. In [108], Yang et al used Bloch mode analysis to elucidate the propagation dynamics of light inside periodic nanowaveguides. They found that the optical properties of designed systems can be accurately described by accounting for contributions from propagating modes inside the dielectric as well as from the mode that is mostly distributed in the medium between the nanowaveguides. The latter is often neglected in typical design methodologies for dielectric metasurfaces, although its effect only becomes more relevant for applications that require beam deflection at large angles.

To cover the full 2π phase modulation, the geometry of the metaatoms can be adjusted. The strong birefringence afforded by the use of high-index constituting material, and introduced via structural anisotropy (i.e. with the use of elliptical nanopillars) has facilitated the independent phase modulation of orthogonal linear polarizations directed along the main axes of the meta-atoms. Such a response can be summarized by the Jones matrix [37, 38, 42]

$$J = R(-\theta) \begin{bmatrix} e^{i\phi_x} & 0 \\ 0 & e^{i\phi_y} \end{bmatrix} R(\theta) \quad (5.1)$$

where ϕ_x and ϕ_y are the imposed phase shifts on the wave components polarized along the meta-atom's fast and slow axes, $R(\theta)$ is a rotation matrix with θ defining the angular orientation of the axes. For meta-atoms whose principal axes are directed in the x and y - directions, the Jones matrix reduces to $J = \begin{bmatrix} e^{i\phi_x} & 0 \\ 0 & e^{i\phi_y} \end{bmatrix}$. In terms of the input field, the output's linearly polarized components are then given by $E_{\text{out},x} = E_{\text{in},x}e^{i\phi_x}$ and $E_{\text{out},y} = E_{\text{in},y}e^{i\phi_y}$. We capitalize on this capability of metasurfaces to fabricate different polarization-dependent optical devices.

The rest of this chapter discusses our work on all-dielectric metasurfaces. Three functional metasurfaces were designed and fabricated, with the ultimate objective of achieving a metasurface that can be used for single-shot QPI.

As discussed in Chapter 2, determining the evolution of an optical wave in subwavelength structures requires the treatment of the full Maxwell's equations. While analytic solutions exist for some geometries, it can be difficult to find closed solutions for others. Thus, numerical calculations are implemented to determine the changes in the wave properties, e.g. its amplitude and phase, after it has propagated through the structure. In our case, we used finite-difference time domain (FDTD) modeling to calculate the transmission coefficients and phase shifts of a beam after passing through a uniformly arranged meta-atoms.

Figure 5.1(a) shows the unit structure of the metasurface that we used in all optical devices that we fabricated. The unit cell consists of elliptical nanopillars made of amorphous silicon (a-Si) on a fused silica (SiO_2) substrate. The height of the nanopillar is 411 nm. The electric permittivity, which was deduced experimentally from a deposited bare layer of silicon, is $\epsilon = 16.55 + 0.16i$. In the calculations, a single nanopillar is periodically arranged in a square lattice with $a = 350$ nm by applying periodic boundary conditions on the sides of the unit cell in both transverse direc-

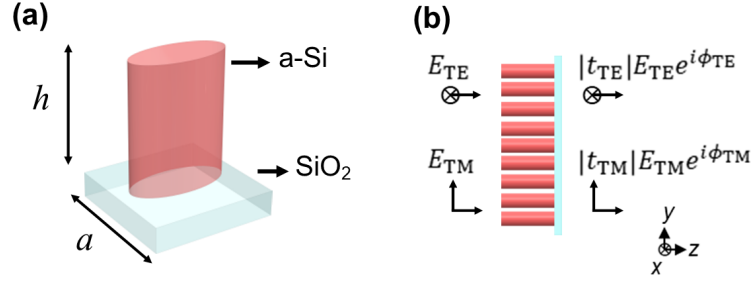


Figure 5.1: **Schematic of the metasurface.** (a) Unit cell of the metasurface consisting of amorphous silicon (a-Si) on SiO_2 substrate. The height of the nanopillars is 411 nm. (b) Schematic of FDTD calculation for the transmission coefficient and phase shift incurred by a beam after passing through a uniform set of pillar periodically arranged in a square lattice with $a = 350$ nm.

tions. Under plane-wave illumination, the transmission coefficients ($|t_{\text{TE}}|, |t_{\text{TM}}|$) and phase shifts ($\phi_{\text{TE}}, \phi_{\text{TM}}$) were calculated for different elliptical nanopillars by sweeping the diameters from 70 - 270 nm in both x and y directions for both TE and TM incident waves, as shown in Figure 5.1(b).

Figure 5.2 shows the magnetic energy density from both (a, b) top-view and (c, d) side-view perspectives for nanopillars with elliptical diameters $D_x = 168$ nm and $D_y = 270$ nm. In (a) and (b), the monitors are placed at the end and inside the nanopillars, respectively. As mentioned earlier, substantial difference between the nanopillars' refractive index and that of the medium results in the field confinement inside the pillar. This is also exemplified in the a-Si pillars that comprise our metasurface. Additionally, the magnetic energy density plots show that there is weak coupling between the meta-atoms, indicating that each site can be regarded as a pixel element that locally modifies the wavefront of the incoming beam. Figure 5.3 shows the calculated transmission coefficients and phase shifts for combinations of elliptical pillar geometries.

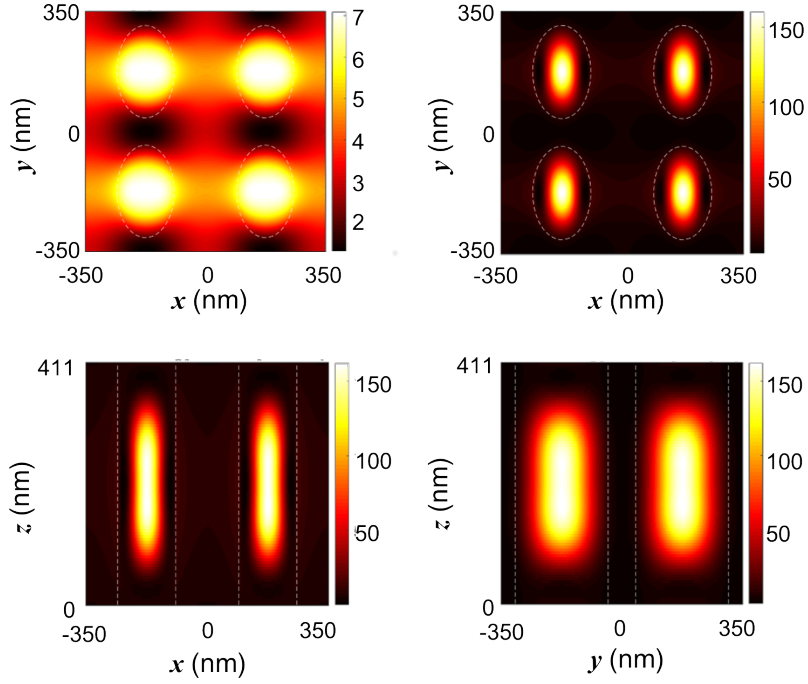


Figure 5.2: **Field confinement in high-index dielectric nanopillar.** Magnetic energy density inside a-Si nanopillars from the (a, b) top-view and (c, d) side-view. For the top-view, the monitors are placed at the end (a) and inside (b) the nanopillars. The elliptical diameters are $D_x = 168$ nm and $D_y = 270$ nm under TE-polarized plane-wave illumination. The dotted lines mark the boundaries of the nanopillars.

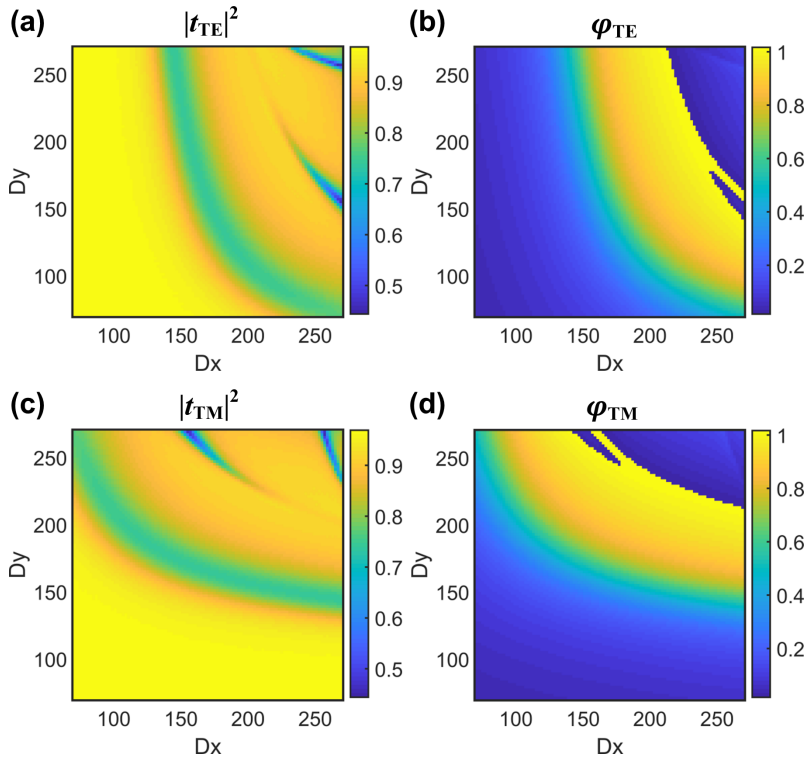


Figure 5.3: **Transmission coefficients and phase shifts** of the beam after passing through periodically arranged nanopillars for different diameters, D_x and D_y , under TE and TM-polarized plane-wave illumination.

From the transmission coefficients and phase shifts obtained using FDTD computations, the optimal geometries of nanopillars to introduce the desired phase shifts are compiled in a library. These were determined by calculating the mean-squared error given by

$$E = \left| e^{i\phi_{\text{TE,desired}}} - t_{\text{TE}} e^{i\phi_{\text{TE}}} \right|^2 + \left| e^{i\phi_{\text{TM,desired}}} - t_{\text{TM}} e^{i\phi_{\text{TM}}} \right|^2. \quad (5.2)$$

where $\phi_{\text{TE(TM),desired}}$ are the desired phase shifts. The geometry that minimizes Equation (5.2) is added to the library. Such a minimization ensures that high transmission is achieved while providing the phase shift that is close to the desired one. Figure 5.6 shows the results of this step, depicting the look-up map to convert the desired phase shift into the geometry of the pillars.

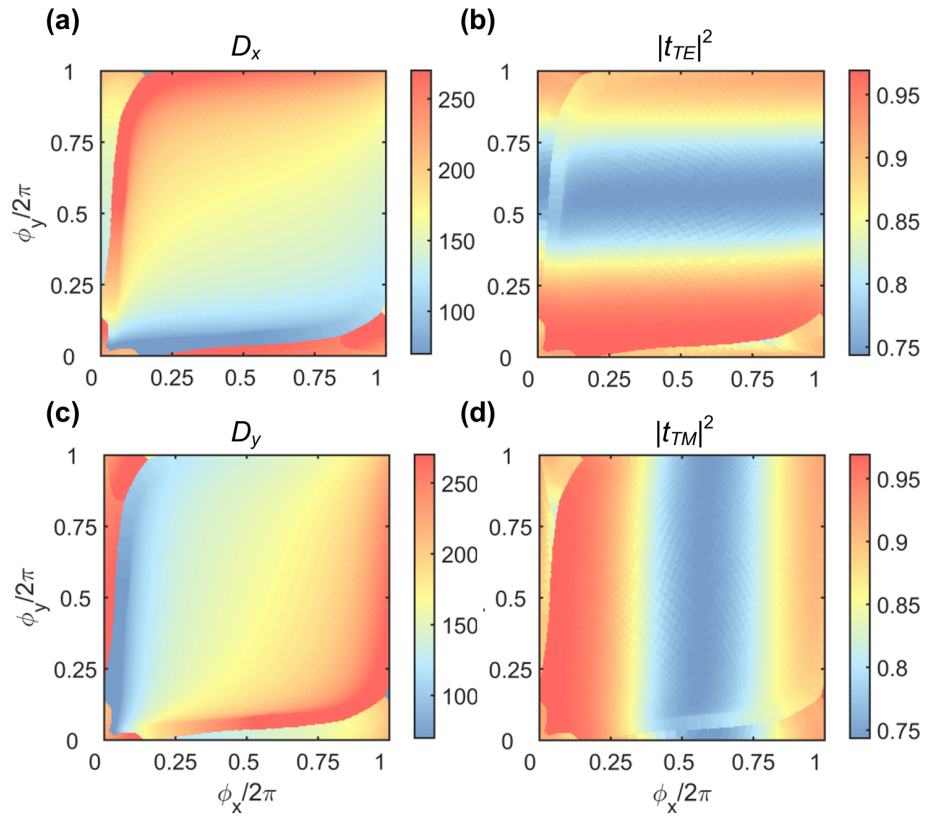


Figure 5.4: **Phase-to-diameter conversion map.** Look-up table to convert a combination of $\phi_{\text{TE}} - \phi_{\text{TM}}$ phase shifts into the elliptical diameters of the nanopillars in (a) x and (c) y directions. (b, d) Transmission coefficients of the nanopillars as a function of the elliptical diameters.

5.2.1 Metasurface design and fabrication process

To determine the metasurface design, the phase profiles $\phi_{\text{TE}}(x, y)$ and $\phi_{\text{TM}}(x, y)$ to be imparted on the incident beam have first to be determined. Note that the variables x and y now denote the 2D spatial position. $\phi_{\text{TE}}(x, y)$ and $\phi_{\text{TM}}(x, y)$ are then wrapped from 0- 2π , and the positions are

discretized with step distance equal to the lattice constant of the metasurface. After which, the pillar geometries are determined in each discretized location using the look-up map.

The fabrication was done by Radu Malureanu and is based on a standard electron beam lithography technique. A layer of amorphous Si is deposited using low pressure chemical vapor deposition (LPCVD) techniques onto a fused silica substrate. Then, a 145nm thick layer of AR-P6200 CSAR resist is spun on top and a thin, 20nm layer of aluminum (Al) is thermally evaporated to help with the discharge of electrons. The desired structure is then exposed and the Al layer is subsequently wet etched in a $\text{H}_3\text{PO}_4:\text{H}_2\text{O}$ solution. After developing, a new Al layer is deposited and lifted off. This new layer is then used as a mask to etch the Si beneath using a BOSCH process. The remaining Al is then wet etched, finally resulting in the desired structure.

5.2.2 Wavefront engineering using metasurfaces

For the first two applications described below, the goal was to verify the capability of our metasurfaces to introduce spatially-dependent phase shifts into the TE and TM components of an incident beam simultaneously. To this end, metaholograms and polarization beam splitters are two functionalities that easily depict independent shaping of two polarizations.

5.3 Metaholograms

A metahologram was designed to have different phase responses to the TE and TM components of an incident beam leading to the shaping of the beam's intensity profile that depends on its polarization state. To achieve such shaping, a $2f$ optical configuration is employed, with the incident beam assumed to have a top-hat intensity profile and a planar wavefront. Experimentally, this can be implemented by truncation of the central region of a magnified and collimated beam using an aperture. By placing the metasurface at the front focal plane of the lens, the phase profile of the hologram is imprinted on the impinging beam resulting in the intensity shaping at the back-focal plane of the lens. Figure 5.5 shows the schematic of a metahologram that transforms a top-hat intensity profile into "DTU" or "META" depending on the polarization of the incident beam.

Design of a metahologram using the Gerchberg-Saxton algorithm

To determine the metahologram's phase profiles, the Gerchberg-Saxton (GS) algorithm is implemented. GS is an iterative calculation to retrieve the phase of an input complex field with *a priori*

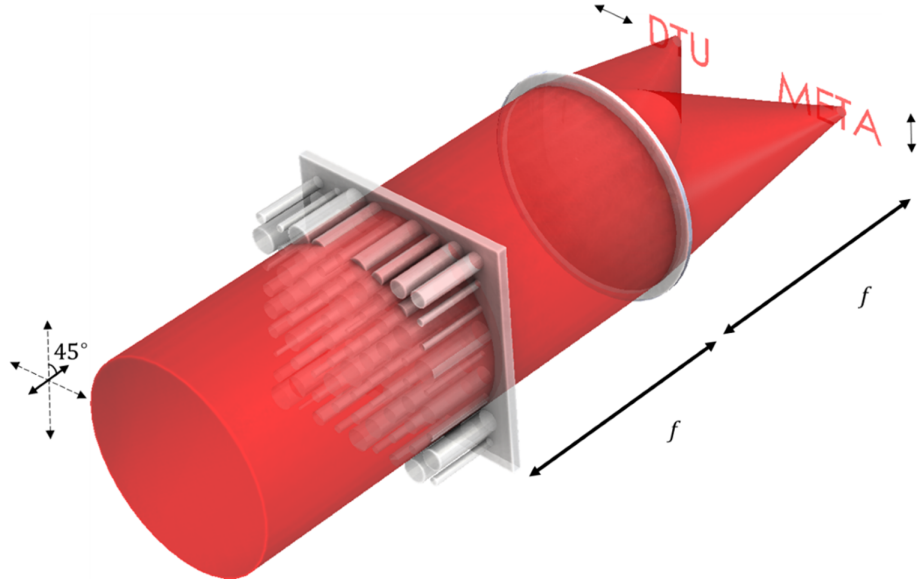


Figure 5.5: **Schematic diagram of a polarization-dependent metahologram.**

information about the field intensities at two planes, traditionally, the spatial and Fourier domains or the front focal plane and back focal plane of a lens, respectively [98]. GS can be viewed as a linear system problem where information about the input is sought, knowing the response of the system (i.e. Fourier transform for $2f$ architecture) and imposing a desired output. The algorithm starts with a complex input field $u(x, y) = \sqrt{I(x, y)}$ at the spatial domain, which is then Fourier transformed to obtain the complex amplitude $\hat{u}(\eta, \nu) = |\hat{u}(\eta, \nu)| \exp(i\hat{\phi}(\eta, \nu))$. At this point, the constraint at the Fourier is implemented by setting $|\hat{u}(\eta, \nu)| = \sqrt{\hat{I}(\eta, \nu)}$ where \hat{I} is the desired output intensity profile of the beam. The resulting field is then inverse Fourier transformed followed by imposing the known profile of the beam $|u'(x, y)| = \sqrt{I(x, y)}$. This constitutes one iteration, and the calculation continues until the calculated and the desired intensities at the $2f$ output have negligible difference.

Experimental demonstration of a polarization-dependent metahologram

The GS algorithm was implemented to generate two different output intensities for TE and TM-polarized components of the incident beam. For FDTD calculations, a metahologram consisting of 32×32 nanopillars was first rendered. From the GS-calculated phase profiles, the elliptical pillar parameters were obtained using the look-up table presented in Figure 5.6. These were then used to generate the metasurface in the FDTD solver *Lumerical* with perfectly matched layer (PML) boundary conditions on all sides of the metasurface. Figure 5.7 shows the far-field intensity distributions from the FDTD calculations under (a) TE and (b) TM polarized plane-wave illumination.

was captured afterwards by a CCD camera. Figure 5.8 shows the output beams shaped by the metasurface under (a) TE and (b) TM polarizations. While an evident zero-order is present, successful shaping of the beam manifests. This indicates effective imprinting of the spatially varying phase shifts onto the incident beam. Furthermore, by rotating the incident polarization and employing an analyzer before the camera, it was observed that cross-polarized light was not shaped by the metasurface. That is, a TE-polarized incident beam produced unshaped intensity profile with values that are within the noise level of the image when the analyzer is cross-polarized. This implies polarization-dependent response of the metasurface. Overall, in this section, we validated the design and fabrication process for a polarization-sensitive metasurface using a metahologram.

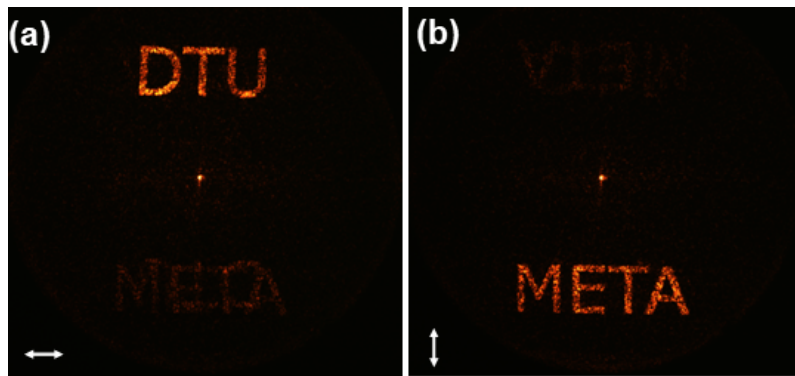


Figure 5.8: **Experimental metahologram output.** Far-field intensity distributions obtained by (a) TE and (b) TM illumination of a fabricated metahologram.

5.4 Polarization beam splitters

To facilitate quantification of the efficiency of the metasurface as a wavefront shaper, polarization-beam splitters were fabricated.

Design of polarization beam splitters

An incident wave can be steered from the optical axis by introducing the continuous phase profile of a blazed grating or a *tilt* to the beam wavefront. Given a desired deflection along the x -axis, the phase function can be expressed as

$$\phi(x, y) = \frac{2\pi}{\lambda} x \tan \alpha \quad (5.3)$$

where α is the steering angle and $-\tan \alpha$ represents the slope of the tilted wavefront in the $x - z$

plane. To split therefore the TE and TM polarizations, different angles α_{TE} and α_{TM} are introduced using the tilt function. In our case, we introduced the same angular displacement magnitude, but with the two traveling in opposite x -directions after the metasurface. Four metasurface designs were fabricated, all working as polarization splitters but with different angular magnitudes: $\alpha = 0.044, 0.088, 0.132$ and 0.176 . Each metasurface was comprised of 1000×1000 nanopillars. FDTD simulations were implemented on the corresponding metasurfaces with smaller cross-sections and comprised of 56×56 pillars to calculate the overall efficiency and the deflection angles (via far-field projection).

Experimental demonstration of polarization beam splitters

To characterize the fabricated polarization splitters, the optical setup shown in Figure 5.9 was constructed. The beam was prepared in a similar fashion as that in the setup for the metaholograms. Here, the metasurface is first imaged through a $10\times$ magnifying optics followed by the detection of its output in the k -space (Fourier plane) by the camera C1, through lens L_3 . A $4f$ system, L_4 and L_5 , with unit magnification was also employed to monitor the position of the metasurface. Importantly, it should be noted that the illumination spot was smaller than the cross-section of the metasurface. From these measurements, two quantities were derived: the deflection angles of the beams and the diffraction efficiency. For the deflection angle, the position of the peak in the expected location of the first-order was converted into the corresponding angular position using $x = f \tan \alpha$, where x is the peak position and $f = 50$ mm. For the diffraction efficiency, the optical power distribution to the different orders were obtained from the images recorded by the camera. From this, the diffraction efficiency was calculated from the ratio of the power in the first order to the total power in all diffraction orders. To obtain an accurate measurement of the power distribution, a series of images was recorded with different exposure times to capture both strong and weak diffraction orders. Figure 5.11 shows a rendered k -space image of the polarization splitter that introduces $\alpha = 0.044$ rad.

The measured deflection angles are summarized in Table 5.1 along with the designed and FDTD-calculated values. For all four metasurfaces, the discrepancy from the designed is very minimal, with a maximum nominal value of $\Delta\alpha = 0.003$ rad (or 0.17°) corresponding to a relative deviation of $|\Delta\alpha|/\alpha = 2.3\%$ for $\alpha = 0.132$ rad. Notably, the precision of the measurement is down to the camera pixel level, equivalent to an angular resolution of 9×10^{-5} rad. Furthermore, the optical

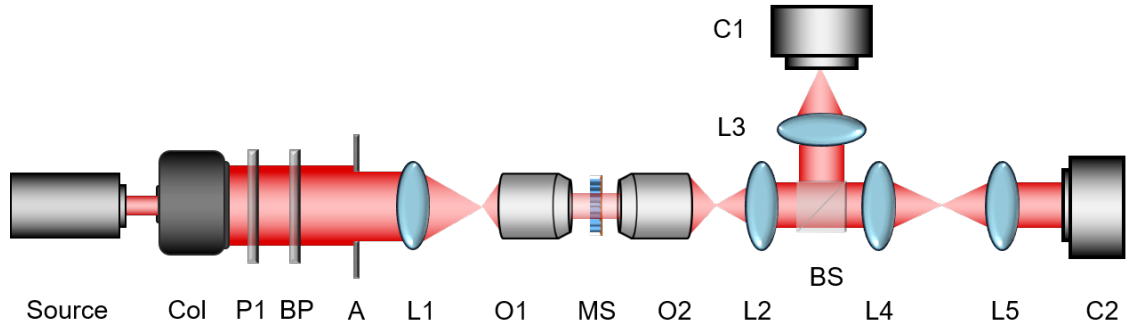


Figure 5.9: **Optical setup for k -space measurements.** Schematic of the optical setup used to characterize the diffraction efficiency of the polarization splitters. Col, collimator; P1, polarizer; BP, bandpass filter; A, aperture, $L_1 - L_5$, lenses; O1-O2, objectives; BS, beams splitter; C1-C2, cameras.

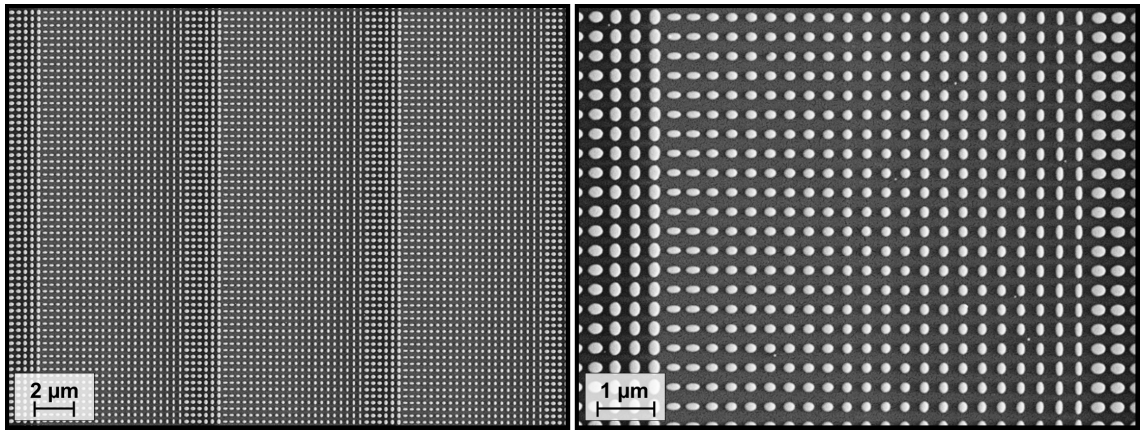


Figure 5.10: **Fabricated metasurface-based polarization splitters.** Scanning electron microscopy (SEM) images of the fabricated polarization splitter for $\alpha = 0.088$.

paths of the two components were separated indicating successful beam splitting capability.

Table 5.1: Designed, simulated and measured deflection angles of the TE and TM beams after passing through the metasurface-based polarization splitter.

	Designed (rad)	FDTD results (rad)	Measured (rad)
	TE / TM	TE / TM	TE / TM
Grating 1	-0.044 / 0.044	-0.041 / 0.041	-0.045 / 0.045
Grating 2	-0.088 / 0.088	-0.087 / 0.088	-0.090 / 0.090
Grating 3	-0.132 / 0.132	-0.131 / 0.130	-0.134 / 0.135
Grating 4	-0.176 / 0.176	-0.173 / 0.173	-0.178 / 0.178

For all four metasurfaces, an overall simulated efficiency of approximately 80% for both TE and TM components was obtained from FDTD calculations. The actual transmission efficiency of the polarization-dependent gratings, obtained by measurement of the relative power transmitted through the metasurfaces, varied from 68-72% as shown in Figure 5.12. The measurements' devi-

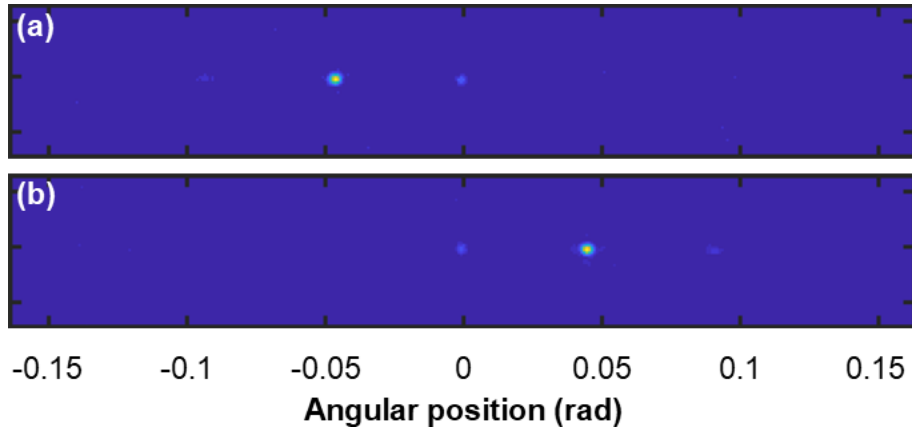


Figure 5.11: **Metasurface-based polarization splitter diffraction orders.** Far-field intensity distributions obtained by (a) TE and (b) TM illumination of the polarization splitter.

ation from the calculated can be due to factors that were not incorporated in the simulations, which include possible fabrication errors. Finally, the experimental diffraction efficiencies are plotted in Figure 5.13, showing that more than 75% of the transmitted optical power is distributed to the right diffraction order. Additionally, the efficiencies for the TE and TM incidence for each metasurface are within 3% of each other, which implies that a 45°-polarized illumination will be split with almost equal intensity.

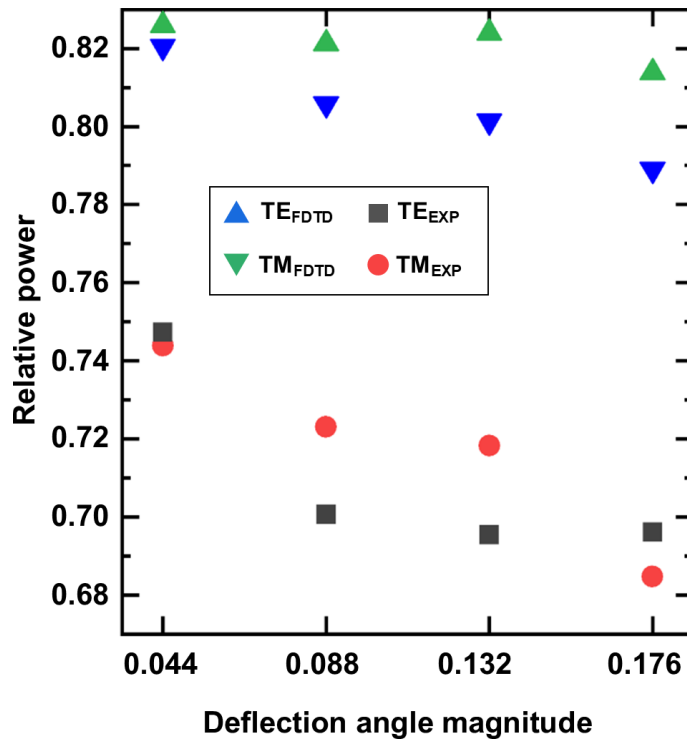


Figure 5.12: **Overall transmission efficiency of the metasurface-based polarization splitters.** Simulated and experimental transmission efficiencies under TE and TM illumination.

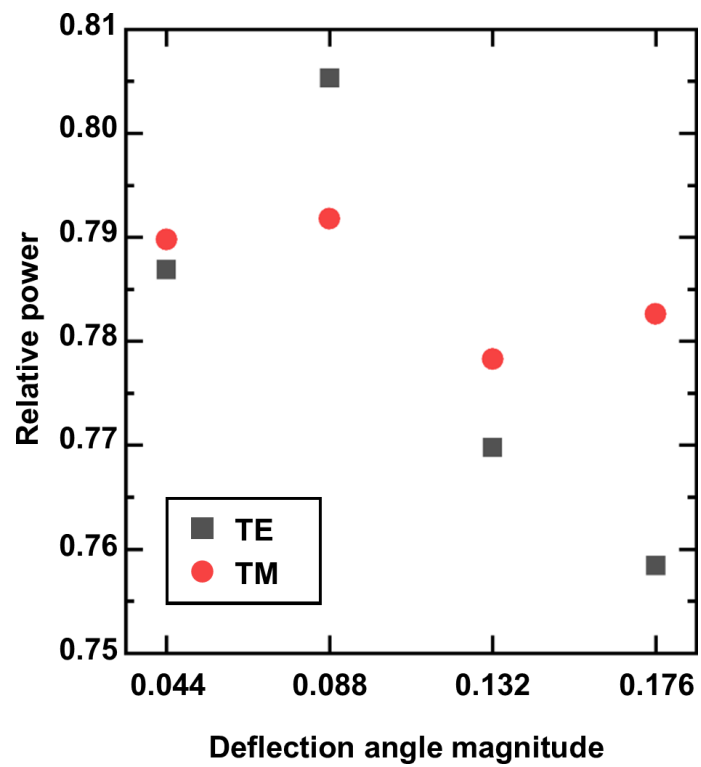


Figure 5.13: **Experimental diffraction efficiencies.** Measured diffraction efficiencies of the metasurface-based polarization splitters.

5.5 Quantitative phase measurement using a polarization-dependent metasurface

5.5.1 The transport-of-intensity equation

The transport-of-intensity equation (TIE) was derived in Michael Teague's original paper as a solution to the parabolic wave equation after imposing paraxial approximation to the Helmholtz wave equation [100]. Although it has been almost 40 years since the seminal paper, TIE-based approach for quantitative phase measurement remains to capture interest because of the simplicity of the technique over other phase reconstruction methods. TIE inherits the advantage of phase retrieval techniques in being non-interferometric, relying only on intensity diversity along the propagation axis. In contrast to other non-interferometry based methods, TIE in principle only requires two intensities for phase restoration. Mathematically, TIE relates the phase to the intensity derivative by [100, 101]

$$-k \frac{\partial I(x, y)}{\partial z} = \nabla_{\perp} \cdot [I(x, y) \nabla_{\perp} \varphi(x, y)]. \quad (5.4)$$

Here, ∇_{\perp} is gradient of the (x, y) directions, $I(x, y)$ is the intensity of the complex field and $\varphi(x, y)$ is the phase to be restored. The axial intensity derivative on the left-hand side of Equation (5.4) can be estimated using the finite difference (FD) of two axially separated intensity distributions:

$$\frac{\partial I}{\partial z} = \frac{I_2 - I_1}{\Delta z} \quad (5.5)$$

where Δz is the separation distance also called the *defocus distance*. Traditionally, for forward or backward difference scheme, the two images are recorded with one being a focused image (I_1) and the other defocused (I_2) by translating the camera or the sample. This limits the application of TIE-based phase retrieval to static objects. The mechanical translation also presents a possible source of instability in the setup.

Iterative calculation of TIE

Different numerical approaches can be implemented to recover the phase profile from two intensity measurements using TIE. Each of these methods entails satisfying boundary conditions, specific

shapes of the aperture bounding the region of interest, and uniformity in the focused intensity distribution [101]. For the boundary conditions, the phase (or its normal derivative) values at the boundary are assumed to be known. For the aperture requirements, specific settings are needed such as in the shape of the aperture, or it being hard-edged or soft-edged. Thirdly, some solvers assume that the focused image has a uniform value, which then reduces the TIE into a simpler Poisson equation that is easier to solve numerically. In practice, these requirements are rather difficult to achieve or establish *a priori*, and they eventually determine the accuracy of the phase calculation [101]. In our work, the iterative approach of Zhang et al. is implemented [122]. This approach was recently reported and shown to be applicable to a wide variety of phase objects, relaxing the requirements mentioned above. The main assumption in this work is that the focused image has a uniform intensity, I_{\max} which is the maximum recorded intensity. While this assumption has no physical grounds, it first simplifies the TIE and is afterwards corrected by iterations until the calculated intensity is negligibly different from the experimental recording.

The algorithm initially assumes a phase solution $\varphi_0 = 0$ and starts by calculating the observed intensity gradient from the focused and defocused images: $\Delta J_0 = \frac{\partial I}{\partial z} = \frac{I_2 - I_1}{\Delta z}$. After which, a phase estimate is calculated from the observed gradients and imposed $I(x, y) = I_{\max}$ assumption: $\phi_0 = -\frac{k}{I_{\max}} \nabla_{\perp}^{-2} \{\Delta J_0\}$. Then, ϕ_0 is used to obtain the calculated intensity gradient: $J_1 = -\frac{1}{k} \nabla_{\perp} \cdot [I(x, y) \nabla_{\perp} \phi_0(x, y)]$, which comes from the right side of the TIE and now utilizes the measured $I(x, y)$. The use of I_{\max} renders the initial calculated intensity gradient J_1 usually different from the observed gradient ΔJ_0 . The difference of the two, $\Delta J_1 = \Delta J_0 - J_1$, is used as the input for the next round of calculation. The phase solution is also updated by $\varphi_1 = \varphi_0 + \phi_0$. This ends one iteration, and the calculation continues until the observed and measured gradients have negligible discrepancy. Figure 5.14 summarizes the iterative calculation of the TIE.

5.5.2 Optical design of the metasurface-based TIE

The optical design of our proposed QPI configuration is shown in Figure 5.15. A $4f$ optical architecture is employed with a 45° -polarized illumination. The sample is placed at the input plane IP and detected at the $4f$ output plane OP by a camera. The polarization-dependent metasurface (MS)-based optical filter is placed at the Fourier plane. It acts to split the TE and TM components of the incident field, and additionally introduces a propagation phase shift onto the TM component. Note that the lenses employed in the setup have the same focal lengths, but the following mathe-

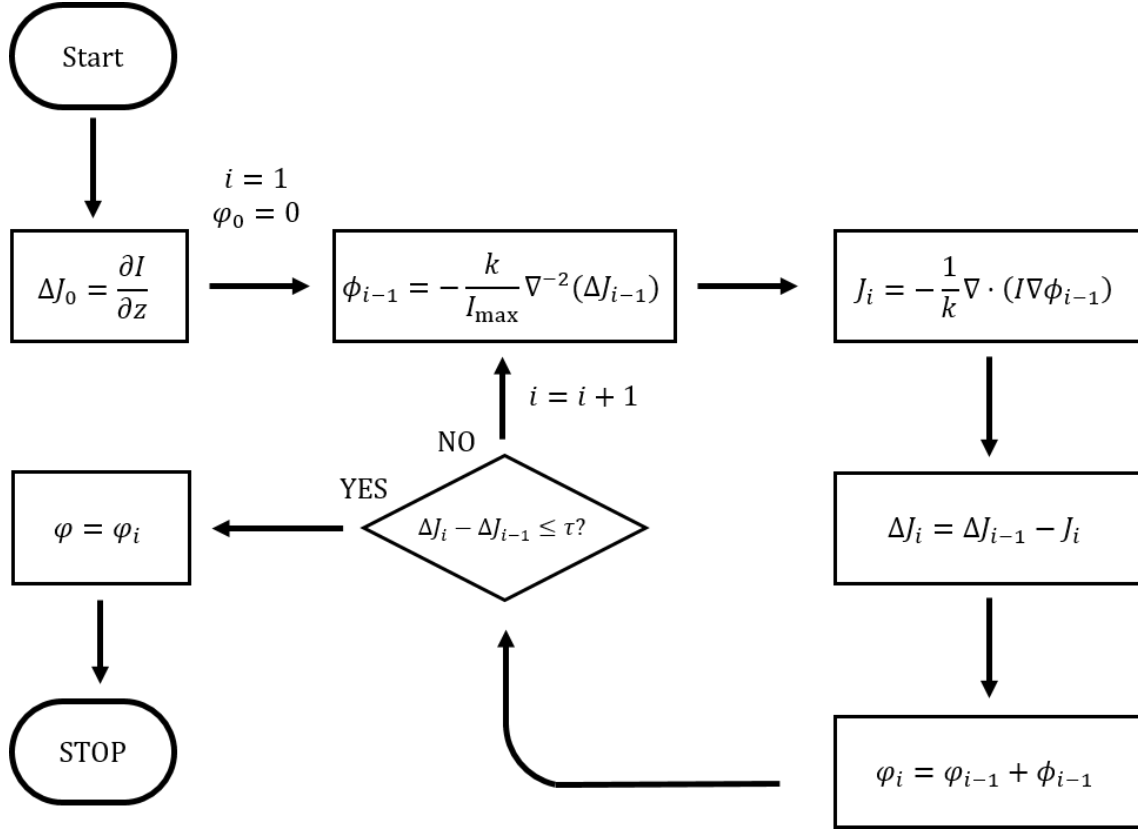


Figure 5.14: Iterative calculation of the TIE.

mathematical formulation can easily be adopted for different ones. Since the eventual target of the setup is microscopy, QPI can be implemented using this technique by relaying the microscope output to the input of the $4f$ setup. Similar to the imaging systems presented in the previous chapters, MS-based TIE can be treated using a paraxial propagation model. The object complex field profile at the input plane is represented as

$$U_{\text{in}}(x, y) = A(x, y) \exp [i\varphi(x, y)] \quad (5.6)$$

where $A(x, y)$ and $\varphi(x, y)$ are the amplitude and phase distributions, and (x, y) are the spatial coordinates. The metasurface response for the TE and TM components can be described separately by their individual transmittance functions

$$t_{\text{TE}}(\eta, \nu) = \exp (i\phi_{\text{TE}}(\eta, \nu)) \quad (5.7a)$$

$$t_{\text{TM}}(\eta, \nu) = \exp (i\phi_{\text{TM}}(\eta, \nu)). \quad (5.7b)$$

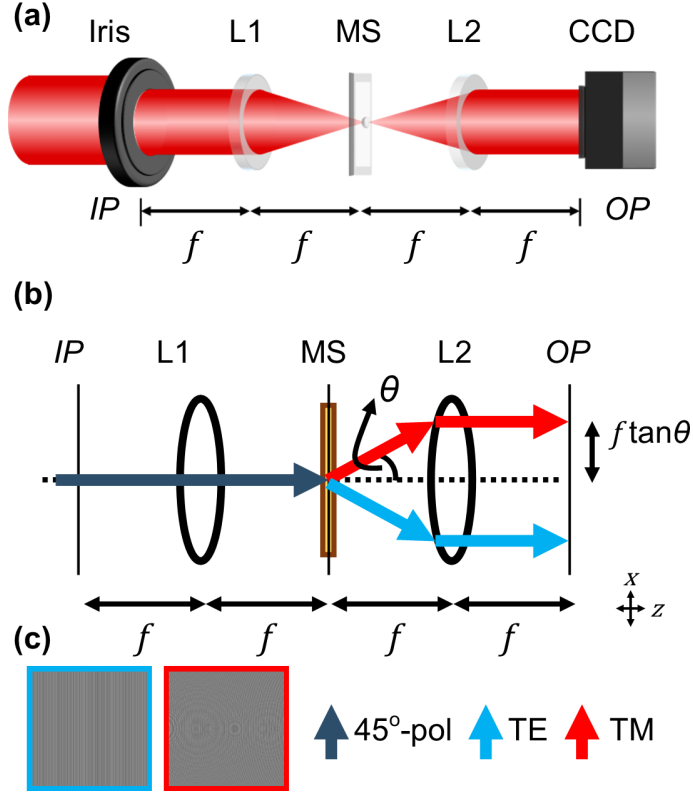


Figure 5.15: **Quantitative phase imaging configuration.** (a) Schematic diagram of the metasurface (MS)-based quantitative phase imaging setup (MS-TIE). L1 and L2 form a $4f$ optical setup. The object located at input plane (IP) is illuminated with a 45° -plane polarized illumination. Note that IP can also coincide with the output or intermediate image plane of a conventional microscope. The metasurface is placed at the Fourier plane and acts as a polarization-dependent optical filter that splits two orthogonal polarization components into two different directions and axially shifts one polarization from the other. (b) Introducing an angular displacement θ at the Fourier plane corresponds to a transverse shift $f \tan \alpha$ at the output of the $4f$ setup. (c) Phase profiles of the metasurface to perform polarization splitting and axial translation.

Here, (η, ν) are the spatial coordinates associated with the x and y directions at the Fourier plane, respectively, related to the spatial frequency coordinates by $\eta = \lambda f f_x$ and $\nu = \lambda f f_y$, λ is the illumination wavelength and f is the focal length of the lenses. In Equation 5.7, $\phi_{TE}(\eta, \nu)$ and $\phi_{TM}(\eta, \nu)$ are the phase profiles of the metasurface given by

$$\phi_{TE}(\eta, \nu) = \frac{2\pi}{\lambda} \eta \tan \alpha \quad (5.8a)$$

$$\phi_{TM}(\eta, \nu) = \frac{2\pi}{\lambda} \left(-\eta \tan \alpha + \Delta z \sqrt{1 - \frac{1}{f^2} (\eta^2 + \nu^2)} \right) \quad (5.8b)$$

As described in Equation 5.8a, the metasurface phase profile for TE illumination operates similar to a blazed grating that deflects the beam by an angle α . The first term in Equation 5.8b is of the same form but with the deflection introduced in the opposite direction for the TM component. The metasurface essentially splits the two components, introducing an angular separation of 2α between the beams. Additionally, the second term in Equation 5.8b is the Rayleigh-Sommerfeld free-space propagation transfer function, as discussed in Chapter 2, simulating the translation of the observation plane by a distance Δz for the TM component. After the second lens, the angular separation transforms into a lateral separation $\Delta d = 2f \tan \alpha$ between the beams while the RS transfer function results in the axial translation of the TM component relative to the TE-polarized wave. Figure 5.15(b) shows the action of the metasurface. Invoking the mathematical concepts discussed in Chapter 2, the PSFs of the system for the two polarizations are

$$\text{PSF}_{\text{TE}}(x, y) = \mathfrak{F} \{t_{\text{TE}}(\eta, \nu)\} = \delta(x - x_0) \otimes f(x, y) \quad (5.9a)$$

$$\text{PSF}_{\text{TM}}(x, y) = \mathfrak{F} \{t_{\text{TM}}(\eta, \nu)\} = \delta(x + x_0) \otimes \mathfrak{F} \left\{ \exp \left[ik\Delta z \sqrt{1 - \frac{1}{f^2} (\eta^2 + \nu^2)} \right] \right\} \otimes f(x, y) \quad (5.9b)$$

where δ is the Dirac delta function. $f(x, y)$ is the Fourier transform of a function in the Fourier space that defines the cross section of the optical filter, which can also include the limited exit aperture of the $4f$ setup itself. For sample feature sizes that are much larger than the resolution limit of the system and for metasurfaces with large cross-sections, $f(x, y)$ also approximates the delta function; for simplicity, this factor is dropped for the rest of the formulation. From Equations 5.6 and 5.9, the corresponding complex field profiles at OP are

$$U_{\text{out,TE}}(x, y) = U(x + x_0, y) \quad (5.10a)$$

$$U_{\text{out,TM}}(x, y) = U(x - x_0, y) \otimes \mathfrak{F} \left\{ \exp \left[ik\Delta z \sqrt{1 - \frac{1}{f^2} (\eta^2 + \nu^2)} \right] \right\} \quad (5.10b)$$

From these equations, the TE-polarized output field of the system is an imaged input field that is centered at $(x = x_0, y = 0)$, while the TM component is an axially displaced copy of the input field centered at $(x = -x_0, y = 0)$. From these mutually orthogonal fields, the intensity recorded by the camera is the sum of the individual intensities: $I(x, y) = I_{\text{TE}}(x, y) + I_{\text{TM}}(x, y)$, where

$$I_{\text{out,TE}}(x, y) = |U(x + x_0, y)|^2 \quad (5.11a)$$

$$I_{\text{out,TM}}(x, y) = \left| U(x - x_0, y) \otimes \mathfrak{F} \left\{ \exp \left[ik\Delta z \sqrt{1 - \frac{1}{f^2} (\eta^2 + \nu^2)} \right] \right\} \right|^2 \quad (5.11b)$$

By adjusting the aperture at the *IP*, the size of the beams can be controlled so that they fit within the camera and to avoid their overlap.

Numerical simulations

Numerical simulations were implemented using FFT-based calculations for phase objects that are common test objects in QPI. Figure 5.16 (a, b) shows the metasurface analytic phase profiles for TE and TM illuminations corresponding to Equation 5.8, which assumes that the metasurface has unit real amplitude. These were transformed into the metasurface design, giving the structural parameters of the nanopillars in each pixel site. Consequently, the nanopillars introduce amplitude and phase shifts on their own as calculated from FDTD simulations that may be different from the unit amplitude and the phase values assigned by Equation 5.8. Both phase distributions, i.e. analytic and converted, were implemented in the simulations. From here on, the former is termed analytic MS-TIE (a-MS-TIE), while the latter is MS-TIE. The converted MS phase profiles are illustrated in Figure 5.16 (c, d) for TE and TM, respectively. As depicted in the zoomed-in versions, some regions of the converted phase profiles deviate from the central part of the analytic. This is due to the fact that not all of the desired (ϕ_x, ϕ_y) combinations can be exactly introduced by the set of nanopillars employed in this work. The yellow box in Figure 5.16 demarcates the extent of the fabricated metasurface.

For the test objects, two types of macroscopic lenses comprising of a convex and a concave designs were employed, whose complex field profile can be expressed as [2, 123]

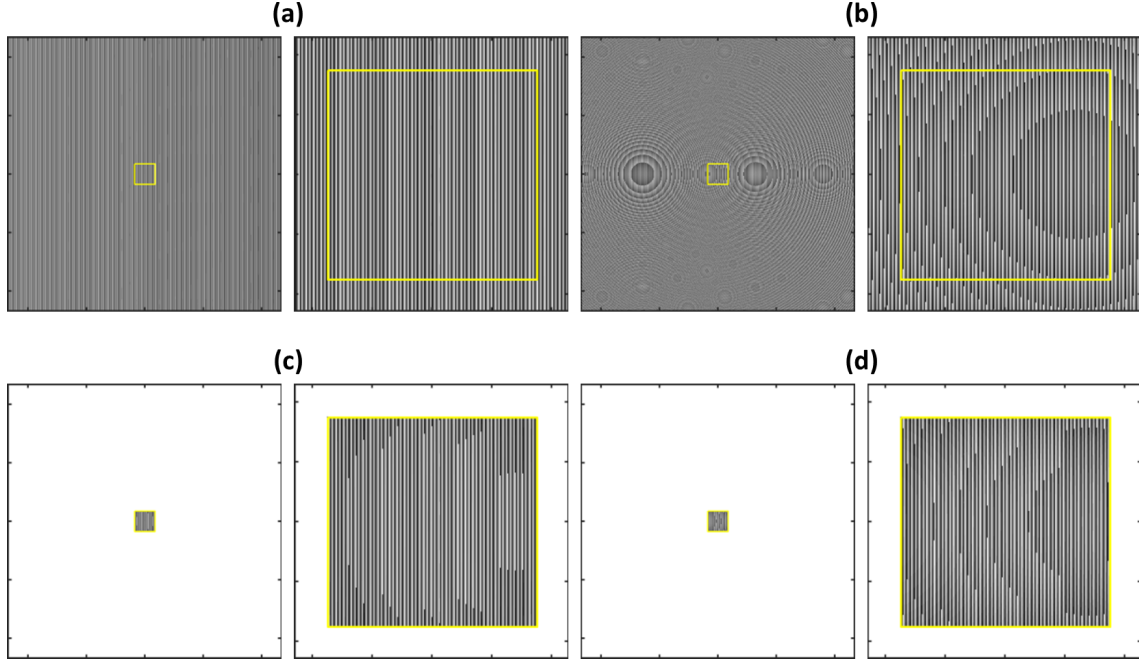


Figure 5.16: **Metasurface phase profiles.** (a, b) Analytic and (c, d) designed phase profiles of the metasurface imparted to the (a, c) TE and (b, d) TM components of an incident wave. Yellow square depicts the size of the fabricated metasurface, $350 \times 350 \mu\text{m}^2$.

$$U_{\text{lens}}(x, y) = A(x, y) \exp \left[(\mp) i \frac{2\pi}{\lambda} \left(\sqrt{f^2 + x^2 + y^2} \right) \right] \quad (5.12)$$

where the $-$ and $+$ signs are associated with the convex and concave lenses, respectively, f is the focal length and $A(x, y)$ is the real amplitude that describes the aperture bounding the lens, which in our case is a square aperture. Figure 5.17 shows the wrapped results from the numerical simulations, which include the analytic phase profile of the lens, and the reconstructions from conventional TIE (C-TIE), a-MS-TIE and MS-TIE for both convex and concave samples. Note that for the TIE reconstructions, an irrelevant constant phase difference was added to obtain the depicted phase maps. Moreover, TIE calculations have continuous phase profiles (i.e. unwrapped phase distributions) but for further comparison with a known robust phase retrieval technique in the experiments, the reconstructions from TIE were wrapped from $-\pi$ to π . By visual inspection of Figure 5.17, a-MS-TIE and MS-TIE both approximate the C-TIE reconstruction, indicating that the limited size and the introduced defocus distance are sufficient for a proof-of-concept demonstration using both the convex and concave lens samples. Furthermore, as mentioned earlier, some regions in the converted MS phase profile deviate from the analytic. The restored phase maps from MS-TIE in Figure 5.17 indicate a robust reconstruction aided by the iterative calculation of the TIE.

Figure 5.18 shows the line profiles of the reconstructed phase maps from numerical simulations of the TIE techniques.

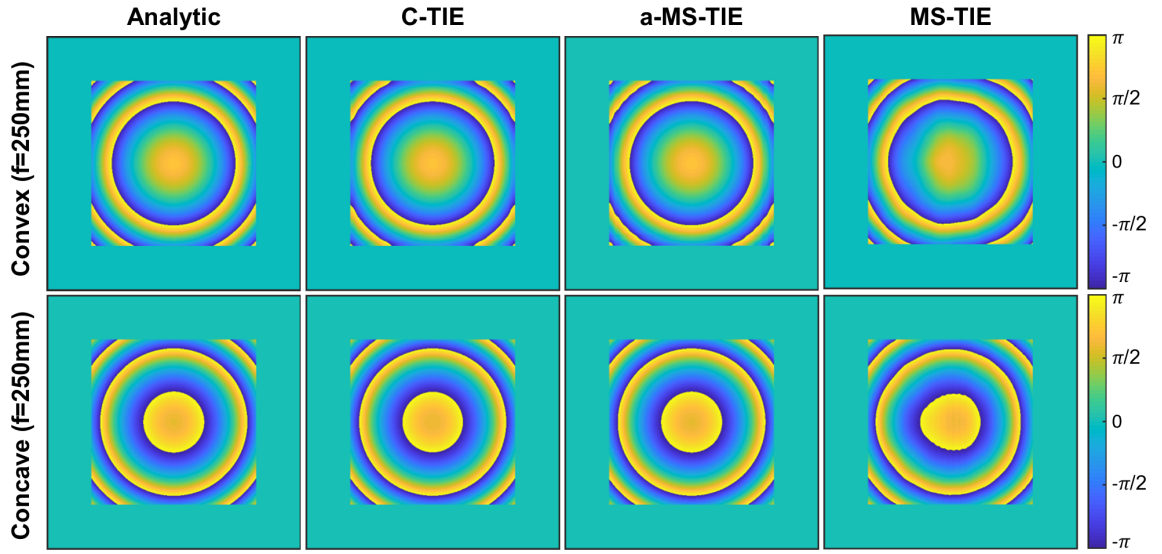


Figure 5.17: **Numerical simulation of MS-based TIE.** Reconstructed phase profiles of (top row) convex and (bottom row) concave lenses with $f = 250$ mm using the conventional TIE and MS-TIE with the analytic (a-MS-TIE) and converted (MS-TIE) phase profiles.

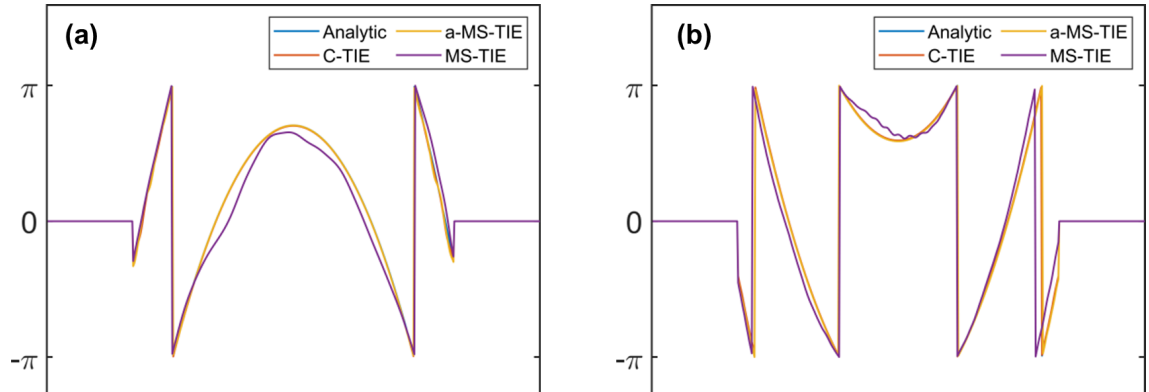


Figure 5.18: **Line profiles of the phase reconstructions.** Phase line scans of the restored phase maps from the simulations for (a) convex and (b) concave lenses.

5.5.3 Experimental demonstration of metasurface-based QPI

For the experimental demonstration, the metasurface is comprised of 2000×2000 pillars and was fabricated using the same procedure specified in Section 5.2.1. A deflection angle magnitude of $\alpha = 0.07$ rad was designed. For $f = 50$ mm, this corresponds to a lateral beam shift of 3.5 mm from the center at the $4f$ output. Figure 5.19 shows SEM images of the fabricated metasurface. The overall efficiency was measured to be 68% and 65% for TE and TM incidence, respectively. This slightly deviates from the obtained efficiency of the metasurface-based polarization splitters

due to the current metasurface being the composite of a blazed grating and the phase component of the RS transfer function.

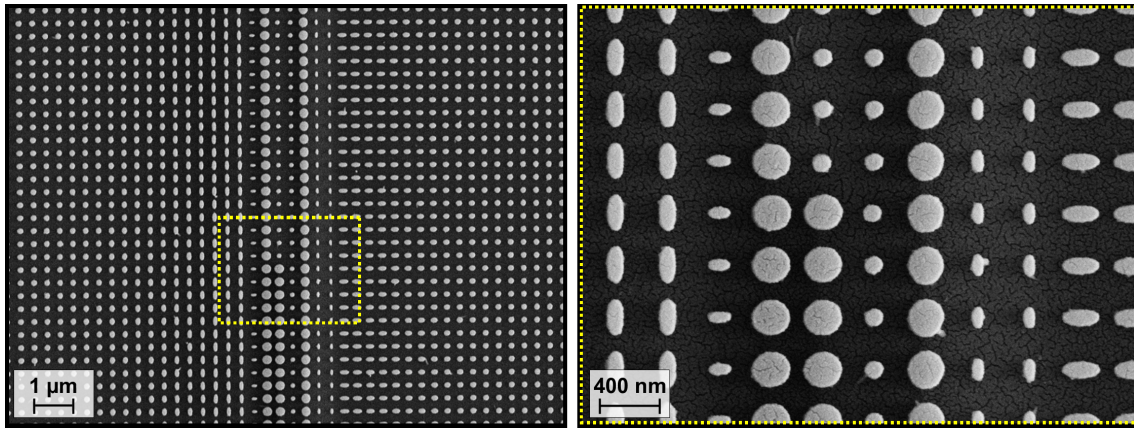


Figure 5.19: **Fabricated metasurface for QPI.** SEM images of the fabricated multifunctional metasurface employed for TIE-based QPI.

Experiments

As proof-of-concept of MS-TIE, its application in wavefront sensing is demonstrated. The optical setup for this experiment is schematically shown in Figure 5.15(a), with a 45° -polarized illumination having a wavelength of 850 ± 40 nm, prepared in the same way as in the previous experiments. A convex lens ($f = 250$ mm) was used as a technical sample by placing it behind the iris, which is a square aperture (width: 1.6 mm) in this case. Figure 5.20(a) shows the image obtained without the metasurface. Figures 5.20(b, c) are the cropped focused and defocused images corresponding to the TE and TM beams, respectively, with the aligned metasurface in the setup. These were then used for phase reconstruction of the lens sample using the iterative TIE. In principle, Figure 5.20(b) should be a focused image of the aperture. The observed blurring can be attributed to the limited size of the metasurface which effectively acts as an apodizing filter in the system. This was also observed in the simulations, but as discussed in Section 5.5.2, the numerical results indicate that good phase reconstruction is possible even with the limited size.

To assess our proposed technique, the restored phase from MS-TIE was compared with that of the conventional implementation of TIE (C-TIE). Figure 5.21 shows the analytic and reconstructed profiles of the lens from FFT-based simulation and the experiments. Here, the profiles are wrapped from $-\pi$ to π because the MS-TIE reconstruction was further benchmarked against a known robust phase retrieval technique called multiple-plane phase retrieval (MPPR). As shown in the restored phase maps, the reconstructions are in good qualitative agreement with each other, even to the

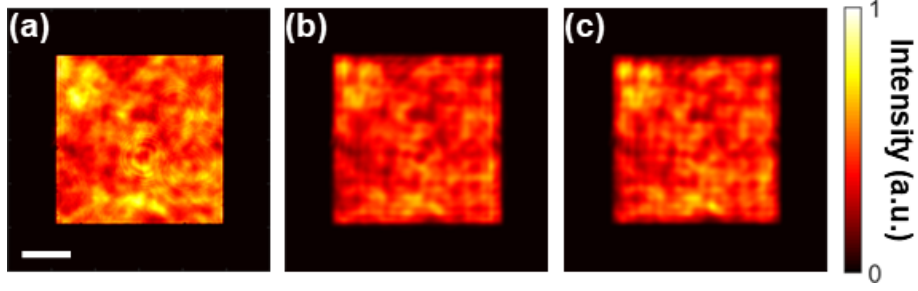


Figure 5.20: **Experimentally obtained images from MS-based phase reconstruction of a convex lens.** (a) Bright-field image (*false color*) of the object without the metasurface in the setup. Cropped images from the split (b) TE and (c) TM beams, respectively, from the MS-TIE. Scale bar: 0.5 mm

analytic profile, apart from obvious artifacts in the phase restored through MS-TIE.

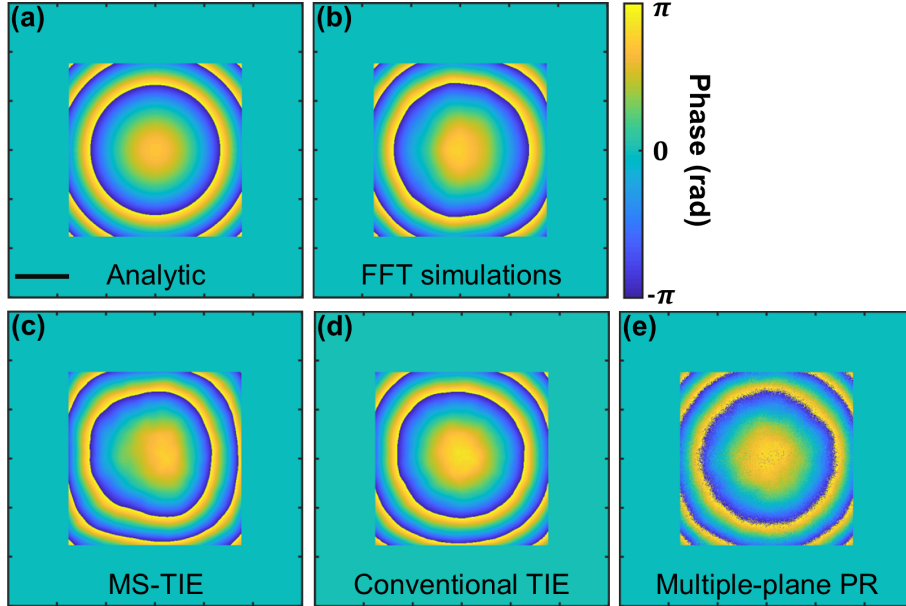


Figure 5.21: **Reconstructed phase profiles of the convex lens.** (a) Phase profile of the convex lens with focal length $f=250$ mm using the analytic equation. (b) Reconstructed phase profile from FFT-based simulations of MS-TIE. Experimentally retrieved phase profiles from (c) MS-TIE, (d) conventional TIE (C-TIE) and (e) multiple-plane phase retrieval.

Quantitatively, the root-mean-squared error (RMSE) values between the analytic and experiments were calculated by

$$\text{RMSE} = \sqrt{\frac{1}{N} \sum_{i=1}^N (\varphi_{\text{an}} - \varphi_{\text{ex}})^2}, \quad (5.13)$$

where $\text{RMSE}_{\text{MS-TIE}} = 0.7804$, $\text{RMSE}_{\text{C-TIE}} = 0.6632$, and $\text{RMSE}_{\text{MPPR}} = 0.7772$. The semblance of the MS-TIE reconstruction with the other results show the potential of the proposed

MS-TIE technique as an alternative to existing methods for non-interferometric QPI. The quantitative nature of the technique, unlike phase-contrast or “qualitative” phase imaging, allows the conversion of the restored phase into the optical thickness profile of the object as shown in Figure 5.22(a). Further comparing the two TIE methods, the line profiles at the center of the unwrapped maps are shown in Figure 5.22(b) for the (left) horizontal and (right) vertical direction. Since the FFT simulations for this sample do not show any of the artifacts observed, further characterization of the metasurface is deemed necessary to assess possible discrepancy of the fabricated metasurface to the designed, but at this point was beyond the present timeline and could not be included in this thesis. We further used the same metasurface to image other phase objects.

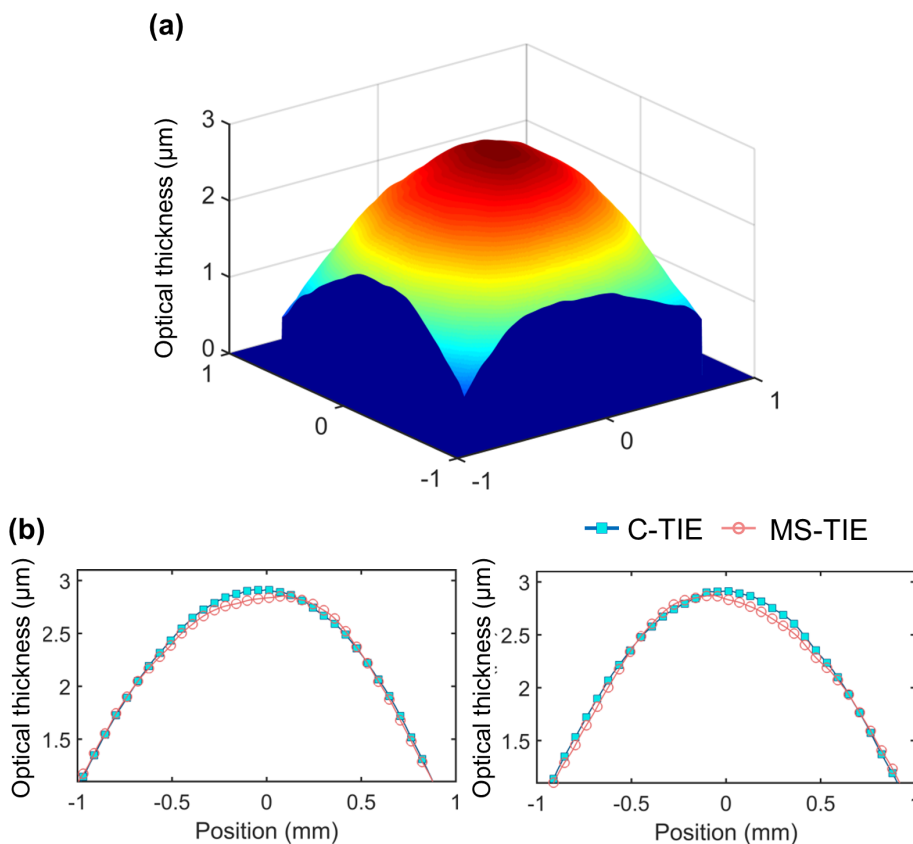


Figure 5.22: **Converted optical thickness of the lens.** (a) Horizontal (left) and vertical (right) line profiles of the optical thickness of the lens converted from MS-TIE and C-TIE. (b) Optical thickness profile from the MS-TIE reconstruction.

A concave lens ($f = 100$ mm) was used as a second technical sample. The same configuration as in the convex lens experiments was implemented. Figure 5.23 show the two intensities obtained from MS-TIE for use in the phase restoration. Figure 5.24 show the reconstruction results from MS-TIE and C-TIE, illustrating similar reconstructions between the two techniques. This implies

that regardless of the direction of the phase curvature, the MS-TIE could potentially work well as the C-TIE.

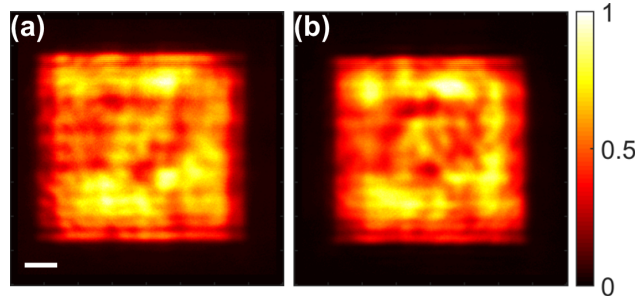


Figure 5.23: **Experimentally obtained images from MS-based TIE configuration for a concave lens technical sample.** Cropped images from the split (a) TE and (b) TM beams, respectively, from the MS-TIE. Scale bar: 0.2 mm

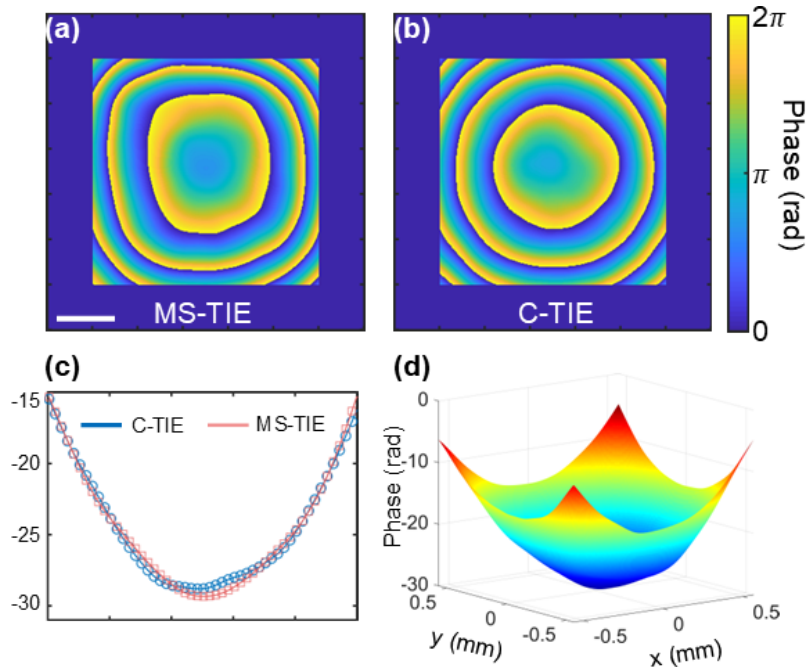


Figure 5.24: **Reconstructed phase profiles of a concave lens.** Phase profile of the concave lens reconstructed experimentally using (a) MS-TIE and (b) C-TIE. (c) Horizontal line profiles at the center of the phase maps and (d) continuous phase distribution of the MS-TIE reconstruction. Scale bar: 0.2 mm.

To further test the proposed technique, MS-TIE was used to image micro bars from a phase-only USAF resolution target. The optical setup is schematically shown in Figure 5.25, which consists of a conventional brightfield microscope whose intermediate image plane coincides with the entrance aperture of the $4f$ setup where the MS is integrated in. The illumination setup is prepared as in the previous demonstrations. The sample plane is imaged using a $10\times$ objective (Leica) and a 200 mm lens. The $4f$ has unit magnification, with $f = 50$ mm.

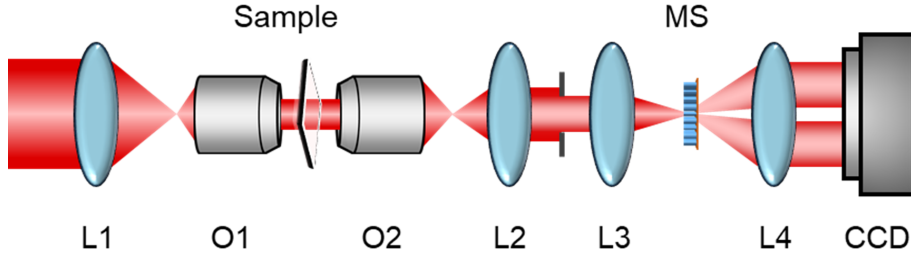


Figure 5.25: **Schematic of the optical setup for the MS-TIE experiments.** L1-L4, lenses; O1-O2, objectives; CCD, camera.

Figure 5.26 shows the raw images of three vertical bars obtained from MS-TIE. After implementing the iterative calculation, Figure 5.27 shows the reconstructed phase maps. As depicted in the figure, MS-TIE is able to discriminate the phase steps from the background, but not as uniform as the reconstruction from C-TIE. The line profile at the center of the retrieved phase profile reveals large variation in the phase values for the three bars: 0.37 rad, 0.69 rad and 1.04 rad. This is in contrast to the C-TIE: 0.76 rad, 0.76 rad and 0.86 rad. An x -dependent phase discrepancy is obvious from the MS-TIE reconstructions. After performing FFT-based simulations, the discrepancy comes mainly from the finite extent of the metasurface that is further compounded by the deviation of the metasurface phase profile from the analytic as specified in Equation 5.8. This effect is more evident for phase profiles with abrupt phase changes as in the case of the bars considered here. With our current metasurface, such an inaccuracy or nonuniformity in the reconstructed phase maps can be bypassed by placing the more relevant features along the y -direction.

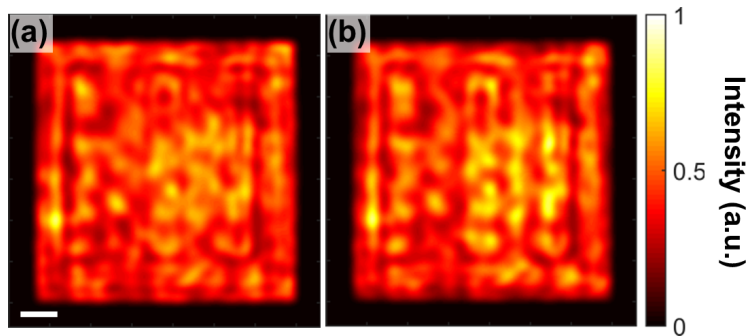


Figure 5.26: **Experimentally obtained raw images of phase-only vertical bars from MS-TIE setup.** Cropped images from the split (a) TE and (b) TM components using the MS-TIE setup. Scale bar: 20 μm

Three horizontal phase-only bars from the same USAF target were imaged using the MS-TIE setup. Figure 5.28 shows the brightfield image and the cropped MS-TIE raw intensities. Figure 5.29 compares the reconstructions from MS-TIE and C-TIE. Here, the reconstructed phase step values of the three horizontal bars have decreased variation for the MS-TIE, albeit still deviating from the

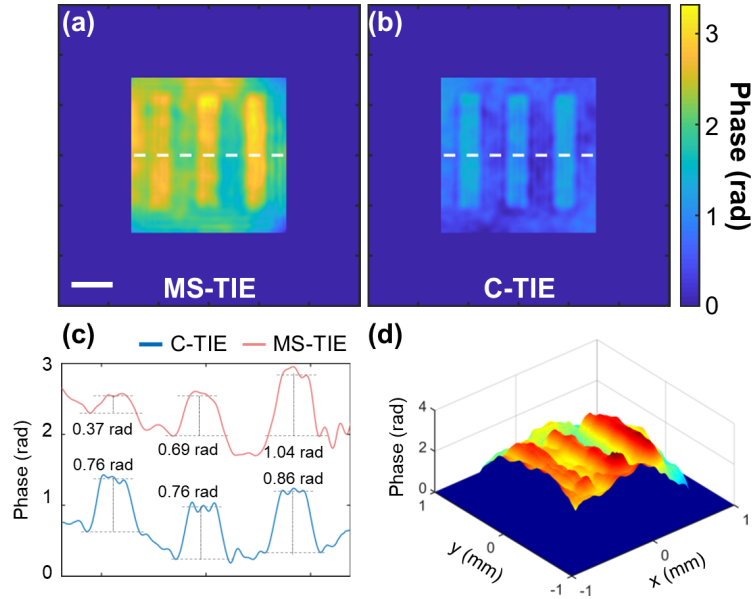


Figure 5.27: **Reconstructed phase maps of phase-only vertical bars** using (a) MS-TIE and (b) C-TIE. (c) Central line scan of the phase maps. (d) Continuous phase distribution of the MS-TIE reconstruction. Scale bar: $40 \mu\text{m}$.

values obtained using C-TIE. This indicates a limitation of the current MS optical device in not being able to retrieve abrupt phase steps and suggests a need for further optimization, for example, in terms of the introduced defocus distance and the size of the metasurface. As a first demonstration, nevertheless, these results show a promising single polarization-dependent metasurface in facilitating quantitative phase measurement.

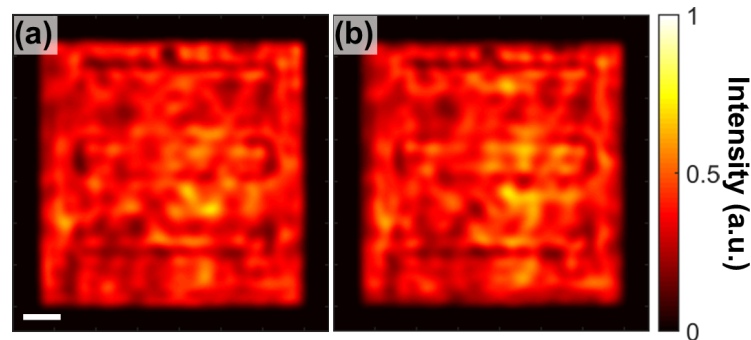


Figure 5.28: **Experimentally obtained raw images of phase-only horizontal bars from MS-TIE setup.** Cropped images from the split (a) TE and (b) TM components using the MS-TIE setup. Scale bar: $20 \mu\text{m}$.

As mentioned above, the size of the metasurface ($700 \times 700 \mu\text{m}^2$) serves as one of the main limitations of the current MS-TIE setup, and accounts for the observed “asymmetry” in the reconstructed phase maps. The effect of which becomes more evident for objects with abrupt phase variations. Eventually, the limited size also dictates the lateral resolution achievable in the setup. This, in

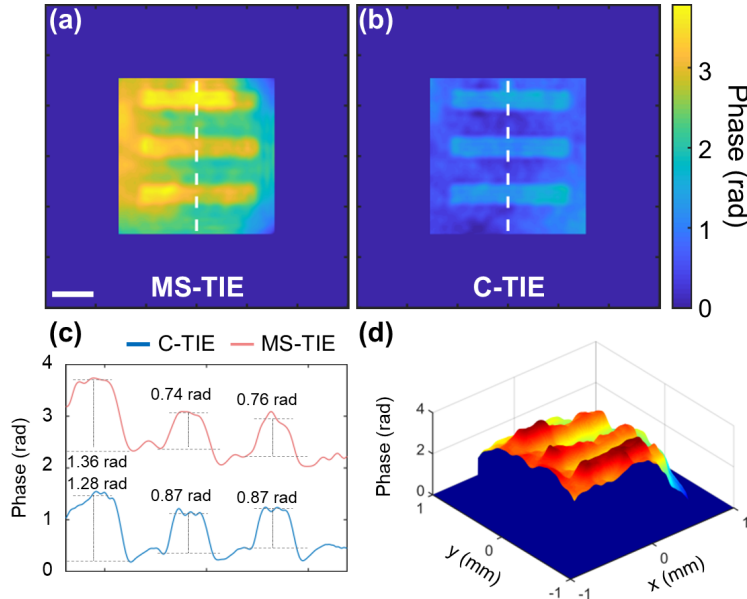


Figure 5.29: **Reconstructed phase maps of phase-only horizontal bars** using (a) MS-TIE and (b) C-TIE. (c) Central line scan of the phase maps. (d) Continuous phase distribution of the MS-TIE reconstruction. Scale bar: $40 \mu\text{m}$.

addition to the large defocus distance introduced, contributes to phase deblurring in the reconstructions. The defocus distance directly affects the estimation of the axial intensity derivative, which in turn determines the accuracy of the phase reconstruction. The work of Paganin et al. in [124] provides a criterion on how to set the defocus distance based on the object's phase variation, spatial frequency and amount of noise in the recorded image. In our case, simulations were first performed, from which, it was deemed that as an initial demonstration, the size and the defocus distance were adequate to obtain good phase reconstructions for samples that have low phase gradients (i.e. lenses). Secondly, the simultaneous recording of two images comes with the penalty in the system's effective field-of-view (FOV). The sensor area to record an image is reduced for the case of MS-TIE. While the FOV is sacrificed, the ability to simultaneously capture the intensities will allow for quantitative phase imaging of dynamic events. Lastly, an advantage of conventional setups is the tunability of the defocus distance, which is known to be object-dependent. Traditionally, changing the displacement magnitude can be easily implemented by mechanical translation of the camera. For single-shot methods, an SLM in conjunction with other bulky components (i.e. mirrors and beam splitter) can also provide such adjustment [102]. Currently, distance tuning is not available in our metasurface. Nonetheless, this does not preclude the use of fixed and optimized metasurfaces to work for diverse types of phase objects. In addition, the flourishing research on tunable metasurfaces indicates the viability of active displacement setting in the future [125–128].

5.6 Summary

In this chapter, metasurface-based optical devices were designed and fabricated to simultaneously modulate the wavefronts of incident beams with orthogonal polarizations. Independent wavefront control was achieved using structurally anisotropic meta-atoms with high refractive index. The fabricated devices include a metahologram, polarization splitters, and a multifunctional device employed for imaging. For the metahologram, successful phase imprinting manifested in the shaped intensities of the output beam. For the polarization splitters, diffraction efficiencies between 75-80% were achieved experimentally for four different angular displacements. For a 45°-polarized incidence, 50-50 splitting of the linear orthogonal components of the incident beam is expected. The overall transmission efficiencies ranged from 68% to 75%. Finally, the multifunctional device acts to split the TE and TM components of the incident beam and add a propagation phase shift onto the TM component relative to the TE polarized wave. Such a device was used to facilitate the simultaneous recording of two images for use in quantitative phase imaging via iterative calculation of the transport-of-intensity equation. Using the proposed approach, QPI of objects with continuous phase profiles was successfully demonstrated, whereas imaging of objects with abrupt phase changes also seems promising, but requires further optimization. This technique has the potential to facilitate simple, compact and rapid QPI, ideal for optical metrology and live label-free microscopy applications.

6 Conclusions

Wavefront engineering is the tailored modulation of the phase profile of an incident beam. Employed as an optical filter in a $4f$ optical configuration, wavefront-modulating elements can facilitate contrast enhancement in an imaging system, allowing access to previously inaccessible information about the incident field.

In this thesis, wavefront modulating elements based on conventional and metasurface optics were employed in standard imaging configurations to facilitate different applications: topological charge determination of orbital angular momentum-carrying beams, nonlinear optical vortex coronagraphy, and quantitative phase imaging of technical samples.

The common-path interferometer was constructed with the aid of a refractive phase element. Topological charges (both magnitude and sign) of helico-conical beams were successfully determined using the constructed interferometer. The performance of the proposed detection system, however, was limited to charge magnitudes that are less than 20 due to the increased spread in the helico-conical beam intensity, which is inherent to all beams that carry orbital angular momentum.

The nonlinear optical vortex coronagraph was facilitated by a commercial optical vortex mask based on liquid crystal polymers. Suppression of a bright source by four orders of magnitude while having minimal effect to an off-axis source was experimentally demonstrated using the proposed setup. From simulations, it is expected that an even better performance can be achieved by employing defect-free vortex masks and larger non-linear crystals. The technique provides a promising extension of masks made for single-wavelength and narrowband operation to work for other wavelengths and for broadband operation. From calculations, a more favorable sensitivity can be achieved with the proposed configuration compared with its linear counterpart.

Finally, a single-shot quantitative phase imaging setup was proposed using an all-dielectric metasurface. Three different optical devices were fabricated to demonstrate the polarization-dependent wavefront control capability of the metasurfaces. Initial experiments of the quantitative phase reconstruction successfully restored phase maps of technical samples with slowly varying phase profile. Promising results were also obtained for objects with abrupt phase jumps, but for accurate reconstructions, further optimization of the metasurface optical device is necessary. The design

proposed in this work allows for the integration of the metasurface in commercial microscopes without the need for additional optical components, which could be beneficial for dynamic quantitative phase imaging in optical microscopy.

References

- [1] F. Zernike, “How i discovered phase contrast,” *Science*, vol. 121, no. 3141, pp. 345–349, 1955.
- [2] J. W. Goodman, *Introduction to Fourier Optics - 3rd ed.* Colorado, USA: Roberts & Company Publishers, 3rd ed., 2005.
- [3] B. E. Saleh and M. C. Teich, *Fundamentals of photonics*. John Wiley & sons, 2019.
- [4] C. Maurer, A. Jesacher, S. Bernet, and M. Ritsch-Marte, “What spatial light modulators can do for optical microscopy,” *Laser and Photonics Reviews*, vol. 5, no. 1, pp. 81–101, 2011.
- [5] A. E. Willner, H. Huang, Y. Yan, Y. Ren, N. Ahmed, G. Xie, C. Bao, L. Li, Y. Cao, Z. Zhao, J. Wang, M. P. J. Lavery, M. Tur, S. Ramachandran, A. F. Molisch, N. Ashrafi, and S. Ashrafi, “Optical communications using orbital angular momentum beams,” *Advances in Optics and Photonics*, vol. 7, no. 1, pp. 66–106, 2015.
- [6] D. G. Grier, “A revolution in optical manipulation,” *Nature*, vol. 424, no. 6950, pp. 810–816, 2003.
- [7] J. R. Moffitt, Y. R. Chemla, S. B. Smith, and C. Bustamante, “Recent advances in optical tweezers,” *Annual review of biochemistry*, vol. 77, 2008.
- [8] S. Kawata, H.-B. Sun, T. Tanaka, and K. Takada, “Finer features for functional microdevices,” *Nature*, vol. 412, no. 6848, pp. 697–698, 2001.
- [9] P. Galajda and P. Ormos, “Complex micromachines produced and driven by light,” *Applied Physics Letters*, vol. 78, no. 2, pp. 249–251, 2001.
- [10] “An in-depth look at axicons.” <https://www.edmundoptics.eu/knowledge-center/application-notes/lasers/an-in-depth-look-at-axicons/>. Accessed: 2020-12-12.
- [11] A. Laskin, “Achromatic refractive beam shaping optics for broad spectrum laser applications,” *Laser Beam Shaping X*, vol. 7430, no. August 2009, p. 743003, 2009.
- [12] A. Laskin and V. Laskin, “Imaging techniques with refractive beam shaping optics,” *Laser Beam Shaping XIII*, vol. 8490, no. October 2012, p. 84900J, 2012.
- [13] J. Glückstad and D. Palima, *Generalized phase contrast : applications in optics and photonics*. Springer, 2009.
- [14] U. Umhofer, E. Jäger, and C. Bischoff, “Refractive and diffractive laser beam shaping optics,” *Laser Technik Journal*, vol. 8, no. 3, pp. 24–27, 2011.
- [15] S. Banerji, M. Meem, B. Sensale-Rodriguez, and R. Menon, “Imaging with flat optics: Metalenses or diffractive lenses?,” *Optica*, vol. 6, no. 6, 2019.
- [16] Z. Zhang, Z. You, and D. Chu, “Fundamentals of phase-only liquid crystal on silicon (LCOS) devices,” *Light: Science and Applications*, vol. 3, no. 10, pp. 1–10, 2014.
- [17] A. Bañas, S. D. Separa, E. Engay, and J. Glückstad, “Point spread function shaping using geometric analysis,” *Optics Communications*, vol. 427, pp. 522–527, 2018.
- [18] A. Banas, E. Engay, A.-I. Bunea, S. D. Separa, and J. Glückstad, “Three-dimensional light sculpting using a geometric analysis,” *Optics Communications*, vol. 431, pp. 210–215, 2019.

- [19] E. Engay, A.-I. Bunea, M. Chouliara, A. Bañas, and J. Glückstad, “Natural convection induced by an optically fabricated and actuated microtool with a thermoplasmonic disk,” *Optics letters*, vol. 43, no. 16, pp. 3870–3873, 2018.
- [20] J. Engelberg and U. Levy, “The advantages of metalenses over diffractive lenses,” *Nature Communications*, vol. 11, no. 1, pp. 9–12, 2020.
- [21] W. Cai and V. M. Shalaev, *Optical Metamaterials*, vol. 10. Springer, 2010.
- [22] V. Giannini, A. I. Fernández-Domínguez, S. C. Heck, and S. A. Maier, “Plasmonic nanoantennas: fundamentals and their use in controlling the radiative properties of nanoemitters,” *Chemical Reviews*, vol. 111, no. 6, pp. 3888–3912, 2011.
- [23] N. Yu and F. Capasso, “Flat optics with designer metasurfaces,” *Nature Materials*, vol. 13, no. 2, pp. 139–150, 2014.
- [24] M. V. Berry, “The adiabatic phase and Pancharatnam’s phase for polarized light,” *Journal of Modern Optics*, vol. 34, no. 11, pp. 1401–1407, 1987.
- [25] E. Hasman, V. Kleiner, G. Biener, and A. Niv, “Polarization dependent focusing lens by use of quantized Pancharatnam-Berry phase diffractive optics,” *Applied Physics Letters*, vol. 82, no. 3, pp. 328–330, 2003.
- [26] Z. Bomzon, V. Kleiner, and E. Hasman, “Pancharatnam–Berry phase in space-variant polarization-state manipulations with subwavelength gratings,” *Optics Letters*, vol. 26, no. 18, p. 1424, 2001.
- [27] M. Kang, T. Feng, H.-T. Wang, and J. Li, “Wave front engineering from an array of thin aperture antennas,” *Optics Express*, vol. 20, no. 14, p. 15882, 2012.
- [28] S. Choudhury, U. Guler, A. Shaltout, V. M. Shalaev, A. V. Kildishev, and A. Boltasseva, “Pancharatnam–Berry Phase Manipulating Metasurface for Visible Color Hologram Based on Low Loss Silver Thin Film,” *Advanced Optical Materials*, vol. 5, no. 10, pp. 1–6, 2017.
- [29] L. Marrucci, C. Manzo, and D. Paparo, “Optical spin-to-orbital angular momentum conversion in inhomogeneous anisotropic media,” *Physical Review Letters*, vol. 96, no. 16, pp. 1–4, 2006.
- [30] C. Pfeiffer and A. Grbic, “Metamaterial Huygens’ surfaces: Tailoring wave fronts with reflectionless sheets,” *Physical Review Letters*, vol. 110, no. 19, pp. 1–5, 2013.
- [31] G. Zheng, H. Mühlenbernd, M. Kenney, G. Li, T. Zentgraf, and S. Zhang, “Metasurface holograms reaching 80% efficiency,” *Nature Nanotechnology*, vol. 10, no. 4, pp. 308–312, 2015.
- [32] J. Zhang, M. ElKabbash, R. Wei, S. C. Singh, B. Lam, and C. Guo, “Plasmonic metasurfaces with 42.3% transmission efficiency in the visible,” *Light: Science and Applications*, vol. 8, no. 1, 2019.
- [33] Q. Zhao, J. Zhou, F. Zhang, and D. Lippens, “Mie resonance-based dielectric metamaterials,” *Materials Today*, vol. 12, no. 12, pp. 60–69, 2009.
- [34] Y. Kivshar and A. Miroshnichenko, “Meta-optics with mie resonances,” *Optics and Photonics News*, vol. 28, no. 1, pp. 24–31, 2017.
- [35] D. Lin, P. Fan, E. Hasman, and M. L. Brongersma, “Dielectric gradient metasurface optical elements,” *Science*, vol. 345, no. 6194, pp. 298–302, 2014.

- [36] R. C. Devlin, M. Khorasaninejad, W. T. Chen, J. Oh, and F. Capasso, “Broadband high-efficiency dielectric metasurfaces for the visible spectrum,” *Proceedings of the National Academy of Sciences of the United States of America*, vol. 113, no. 38, pp. 10473–10478, 2016.
- [37] A. Arbabi, Y. Horie, M. Bagheri, and A. Faraon, “Dielectric metasurfaces for complete control of phase and polarization with subwavelength spatial resolution and high transmission,” *Nature Nanotechnology*, vol. 10, no. 11, pp. 937–943, 2015.
- [38] J. P. Balthasar Mueller, N. A. Rubin, R. C. Devlin, B. Groever, and F. Capasso, “Metasurface Polarization Optics: Independent Phase Control of Arbitrary Orthogonal States of Polarization,” *Physical Review Letters*, vol. 118, no. 11, 2017.
- [39] I. Staude, A. E. Miroshnichenko, M. Decker, N. T. Fofang, S. Liu, E. Gonzales, J. Dominguez, T. S. Luk, D. N. Neshev, I. Brener, *et al.*, “Tailoring directional scattering through magnetic and electric resonances in subwavelength silicon nanodisks,” *ACS Nano*, vol. 7, no. 9, pp. 7824–7832, 2013.
- [40] M. Decker, I. Staude, M. Falkner, J. Dominguez, D. N. Neshev, I. Brener, T. Pertsch, and Y. S. Kivshar, “High-Efficiency Dielectric Huygens’ Surfaces,” *Advanced Optical Materials*, vol. 3, no. 6, pp. 813–820, 2015.
- [41] K. E. Chong, L. Wang, I. Staude, A. R. James, J. Dominguez, S. Liu, G. S. Subramania, M. Decker, D. N. Neshev, I. Brener, and Y. S. Kivshar, “Efficient Polarization-Insensitive Complex Wavefront Control Using Huygens’ Metasurfaces Based on Dielectric Resonant Meta-atoms,” *ACS Photonics*, vol. 3, no. 4, pp. 514–519, 2016.
- [42] H. Duan, Y. Hu, X. Wang, X. Luo, X. Ou, L. Li, Y. Chen, P. Yang, and S. Wang, “All-dielectric metasurfaces for polarization manipulation: Principles and emerging applications,” *Nanophotonics*, vol. 9, no. 12, pp. 3755–3780, 2020.
- [43] A. Arbabi, Y. Horie, A. J. Ball, M. Bagheri, and A. Faraon, “Subwavelength-thick lenses with high numerical apertures and large efficiency based on high-contrast transmitarrays,” *Nature Communications*, vol. 6, no. May, pp. 2–7, 2015.
- [44] S. M. Kamali, E. Arbabi, A. Arbabi, and A. Faraon, “A review of dielectric optical metasurfaces for wavefront control,” vol. 7, no. 6, pp. 1041–1068, 2018.
- [45] K. Ladavac and D. G. Grier, “Microoptomechanical pumps assembled and driven by holographic optical vortex arrays,” *Optics Express*, vol. 12, no. 6, pp. 1144–1149, 2004.
- [46] X. Li, Y. Liang, S. Zhan, J. Xu, J. Bai, and K. Wang, “Optical vortex beam direct-writing photolithography,” *Applied Physics Express*, vol. 11, no. 3, 2018.
- [47] A. M. Yao and M. J. Padgett, “Orbital angular momentum: origins, behavior and applications,” *Advances in Optics and Photonics*, vol. 3, no. 2, p. 161, 2011.
- [48] J. M. Hickmann, E. J. Fonseca, W. C. Soares, and S. Chávez-Cerda, “Unveiling a truncated optical lattice associated with a triangular aperture using light’s orbital angular momentum,” *Physical Review Letters*, vol. 105, no. 5, pp. 1–4, 2010.
- [49] C.-S. Guo, L.-L. Lu, and H.-T. Wang, “Characterizing topological charge of optical vortices by using an annular aperture,” *Optics Letters*, vol. 34, no. 23, pp. 3686–3688, 2009.
- [50] L. A. Melo, A. J. Jesus-Silva, S. Chávez-Cerda, P. H. Ribeiro, and W. C. Soares, “Direct Measurement of the Topological Charge in Elliptical Beams Using Diffraction by a Triangular Aperture,” *Scientific Reports*, vol. 8, no. 1, pp. 1–8, 2018.

- [51] H. I. Sztul and R. R. Alfano, “Double-slit interference with Laguerre-Gaussian beams,” *Optics Letters*, vol. 31, no. 7, pp. 1–3, 2006.
- [52] D. Jianji, Z. Hailong, and Z. Xinliang, “Dynamic interferometry measurement of orbital angular momentum of light,” *Optics letters*, vol. 39, no. 20, p. 7, 2014.
- [53] S. Slussarenko, V. D’Ambrosio, B. Piccirillo, L. Marrucci, and E. Santamato, “The Polarizing Sagnac Interferometer: a tool for light orbital angular momentum sorting and spin-orbit photon processing,” *Optics Express*, vol. 18, no. 26, p. 27205, 2010.
- [54] A. D’Errico, R. D’Amelio, B. Piccirillo, F. Cardano, and L. Marrucci, “Measuring the complex orbital angular momentum spectrum and spatial mode decomposition of structured light beams,” *Optica*, vol. 4, no. 11, pp. 1350–1357, 2017.
- [55] S. Zheng and J. Wang, “Measuring Orbital Angular Momentum (OAM) States of Vortex Beams with Annular Gratings,” *Scientific Reports*, vol. 7, no. January, pp. 1–9, 2017.
- [56] Z. Liu, S. Gao, W. Xiao, J. Yang, X. Huang, Y. Feng, J. Li, W. Liu, and Z. Li, “Measuring high-order optical orbital angular momentum with a hyperbolic gradually changing period pure-phase grating,” *Optics Letters*, vol. 43, no. 13, pp. 3076–3079, 2018.
- [57] C. A. Alonzo, P. J. Rodrigo, and J. Glückstad, “Helico-conical optical beams: a product of helical and conical phase fronts,” *Optics Express*, vol. 13, no. 5, pp. 1749–1760, 2005.
- [58] V. R. Daria, D. Z. Palima, and J. Glückstad, “Optical twists in phase and amplitude,” *Optics Express*, vol. 19, pp. 476–481, jan 2011.
- [59] J. Glückstad and P. C. Mogensen, “Optimal phase contrast in common-path interferometry.,” *Applied Optics*, vol. 40, pp. 268–282, jan 2001.
- [60] P. J. Rodrigo, D. Palima, and J. Glückstad, “Accurate quantitative phase imaging using generalized phase contrast,” *Optics Express*, vol. 16, no. 4, pp. 2498–2509, 2008.
- [61] M. J. Villangca, A. R. Bañas, D. Palima, and J. Glückstad, “Dark GPC: extended nodal beam areas from binary-only phase,” *Optical Engineering*, vol. 55, no. 12, p. 125102, 2016.
- [62] F. Kenny, F. Choi, J. Glückstad, and M. Booth, “Adaptive optimisation of a generalised phase contrast beam shaping system,” *Optics Communications*, vol. 342, pp. 109–114, 2015.
- [63] K. Crabtree, J. A. Davis, and I. Moreno, “Optical processing with vortex-producing lenses,” *Applied Optics*, vol. 43, no. 6, pp. 1360–1367, 2004.
- [64] S. FÜRhapter, A. Jesacher, S. Bernet, and M. Ritsch-Marte, “Spiral phase contrast imaging in microscopy,” *Optics Express*, vol. 13, no. 3, p. 689, 2005.
- [65] D. Mawet, P. Riaud, O. Absil, and J. Surdej, “Annular Groove Phase Mask Coronagraph,” *The Astrophysical Journal*, vol. 633, no. 2, pp. 1191–1200, 2005.
- [66] G. Foo, D. M. Palacios, and G. A. Swartzlander, “Optical vortex coronagraph,” *Optics Letters*, vol. 30, no. 24, pp. 3308–3310, 2005.
- [67] J. H. Lee, G. Foo, E. G. Johnson, and G. A. Swartzlander, “Experimental verification of an optical vortex coronagraph,” *Physical Review Letters*, vol. 97, no. 5, pp. 6–9, 2006.
- [68] G. A. Swartzlander, E. L. Ford, R. S. Abdul-Malik, L. M. Close, M. A. Peters, D. M. Palacios, and D. W. Wilson, “Astronomical demonstration of an optical vortex coronagraph,” *Opt. Express*, vol. 16, no. 14, pp. 10200–10207, 2008.

- [69] C. Delacroix, O. Absil, P. Forsberg, D. Mawet, V. Christiaens, M. Karlsson, A. Boccaletti, P. Baudoz, M. Kuittinen, I. Vartiainen, J. Surdej, and S. Habraken, “Laboratory demonstration of a mid-infrared AGPM vector vortex coronagraph,” *Astronomy and Astrophysics*, vol. 553, pp. 1–8, 2013.
- [70] X. Wang, Z. Nie, Y. Liang, J. Wang, T. Li, and B. Jia*, “Recent advances on optical vortex generation,” *Nanophotonics*, vol. 7, no. 9, pp. 1533–1556, 2018.
- [71] G. A. Swartzlander, Jr., “Achromatic optical vortex lens,” *Optics Letters*, vol. 31, no. 13, p. 2042, 2006.
- [72] G. Ruane, D. Mawet, A. E. Riggs, and E. Serabyn, “Scalar vortex coronagraph mask design and predicted performance,” in *SPIE Techniques and Instrumentation for Detection of Exoplanets IX*, no. September, p. 61, 2019.
- [73] E. Serabyn, E. Huby, K. Matthews, D. Mawet, O. Absil, B. Femenia, P. Wizinowich, M. Karlsson, M. Bottom, R. Campbell, B. Carlomagno, D. Defrère, C. Delacroix, P. Forsberg, C. G. Gonzalez, S. Habraken, A. Jolivet, K. Liewer, S. Lilley, P. Piron, M. Reggiani, J. Surdej, H. Tran, E. V. Catalán, and O. Wertz, “the W. M. Keck Observatory Infrared Vortex Coronagraph and a First Image of Hip 79124 B,” *The Astronomical Journal*, vol. 153, no. 1, p. 43, 2017.
- [74] G. A. Swartzlander, “The optical vortex coronagraph,” *Journal of Optics A: Pure and Applied Optics*, vol. 11, no. 9, 2009.
- [75] A. Barh, P. J. Rodrigo, L. Meng, C. Pedersen, and P. Tidemand-Lichtenberg, “Parametric upconversion imaging and its applications,” *Advances in Optics and Photonics*, vol. 11, no. 4, pp. 952–1019, 2019.
- [76] G. H. Shao, Z. J. Wu, J. H. Chen, F. Xu, and Y. Q. Lu, “Nonlinear frequency conversion of fields with orbital angular momentum using quasi-phase-matching,” *Physical Review A - Atomic, Molecular, and Optical Physics*, vol. 88, no. 6, pp. 1–7, 2013.
- [77] F. Steinlechner, N. Hermosa, V. Pruneri, and J. P. Torres, “Frequency conversion of structured light,” *Scientific Reports*, vol. 6, no. January, pp. 1–8, 2016.
- [78] S. K. Liu, C. Yang, S. L. Liu, Z. Y. Zhou, Y. Li, Y. H. Li, Z. H. Xu, G. C. Guo, and B. S. Shi, “Up-Conversion Imaging Processing with Field-of-View and Edge Enhancement,” *Physical Review Applied*, vol. 11, no. 4, p. 1, 2019.
- [79] X. Qiu, F. Li, W. Zhang, Z. Zhu, and L. Chen, “Spiral phase contrast imaging in nonlinear optics: seeing phase objects using invisible illumination,” *Optica*, vol. 5, no. 2, p. 208, 2018.
- [80] D. Mawet, E. Serabyn, K. Liewer, C. Hanot, S. McEldowney, D. Shemo, and N. O’Brien, “Optical Vectorial Vortex Coronagraphs using Liquid Crystal Polymers: theory, manufacturing and laboratory demonstration,” *Optics Express*, vol. 17, no. 3, p. 1902, 2009.
- [81] D. Mawet, E. Serabyn, K. Liewer, R. Burruss, J. Hickey, and D. Shemo, “The vector vortex coronagraph: Laboratory results and first light at palomar observatory,” *Astrophysical Journal*, vol. 709, no. 1, pp. 53–57, 2010.
- [82] E. Serabyn, C. M. Prada, P. Chen, and D. Mawet, “Vector vortex coronagraphy for exoplanet detection with spatially variant diffractive waveplates,” *Journal of the Optical Society of America B*, vol. 36, no. 5, p. D13, 2019.
- [83] V. G. Dmitriev, G. G. Gurzadyan, and D. N. Nikogosyan, *Handbook of Nonlinear Optical Crystals*. Springer-Verlag Berlin Heidelberg GmbH, 3rd ed ed., 1998.

- [84] R. L. Pedersen, L. Hogstedt, A. Barh, L. Meng, and P. Tidemand-Lichtenberg, "Characterization of the NEP of mid-infrared upconversion detectors," *IEEE Photonics Technology Letters*, vol. 31, no. 9, pp. 681–684, 2019.
- [85] P. J. De Groot, "A review of selected topics in interferometric optical metrology," *Reports on Progress in Physics*, vol. 82, no. 5, 2019.
- [86] A. G. Marrugo, F. Gao, and S. Zhang, "State-of-the-art active optical techniques for three-dimensional surface metrology: a review [Invited]," *Journal of the Optical Society of America A*, vol. 37, no. 9, p. B60, 2020.
- [87] C. Edwards, R. Zhou, S.-W. Hwang, S. J. McKeown, K. Wang, B. Bhaduri, R. Ganti, P. J. Yunker, A. G. Yodh, J. A. Rogers, L. L. Goddard, and G. Popescu, "Diffraction phase microscopy: monitoring nanoscale dynamics in materials science [Invited]," *Applied Optics*, vol. 53, no. 27, p. G33, 2014.
- [88] G. Popescu, *Quantitative phase imaging of cells and tissues*. McGraw-Hill Education, 2011.
- [89] T. Cacace, V. Bianco, and P. Ferraro, "Quantitative phase imaging trends in biomedical applications," *Optics and Lasers in Engineering*, no. May, 2020.
- [90] P. F. Almero, P. N. Gundu, and S. G. Hanson, "Phase retrieval With Speckle Illumination," *Optics Letters*, vol. 34, no. 4, pp. 521–523, 2009.
- [91] C. J. Mann, P. R. Bingham, V. C. Paquit, and K. W. Tobin, "Quantitative phase imaging by three-wavelength digital holography," vol. 16, no. 13, pp. 14591–14600, 2008.
- [92] S. Khadir, D. Andr n, R. Verre, Q. Song, S. Monneret, P. Genevet, M. K ll, and G. Baffou, "Metasurface optical characterization using quadriwave lateral shearing interferometry," *arXiv*, 2020.
- [93] M. Niu, G. Luo, X. Shu, F. Qu, S. Zhou, Y.-P. Ho, R. Zhou, and N. Zhao, "A Portable Quantitative Phase Microscope for Material Metrology and Biological Imaging," *Photonics Research*, vol. 8, no. 7, 2020.
- [94] B. Kemper and G. Von Bally, "Digital holographic microscopy for live cell applications and technical inspection," *Applied Optics*, vol. 47, no. 4, 2008.
- [95] M. R. Arnison, K. G. Larkin, C. J. Sheppard, N. I. Smith, and C. J. Cogswell, "Linear phase imaging using differential interference contrast microscopy," *Journal of Microscopy*, vol. 214, no. 1, pp. 7–12, 2004.
- [96] H. Kwon, E. Arbabi, S. M. Kamali, M. S. Faraji-Dana, and A. Faraon, "Single-shot quantitative phase gradient microscopy using a system of multifunctional metasurfaces," *Nature Photonics*, vol. 14, no. 2, pp. 109–114, 2020.
- [97] P. Bon, G. Maucort, and B. Wattellier, "Quadriwave lateral shearing interferometry for quantitative phase microscopy of living cells," *Optics Express*, vol. 17, no. 15, pp. 468–470, 2009.
- [98] R. W. Gerchberg and W. O. Saxton, "A practical algorithm for the determination of phase from image and diffraction plane pictures," *Optik*, vol. 35, pp. 237–246, 1972.
- [99] P. Almero, G. Pedrini, and W. Osten, "Complete wavefront reconstruction using sequential intensity measurements of a volume speckle field," *Applied Optics*, vol. 45, no. 34, pp. 8596–8605, 2006.

- [100] M. R. Teague, “Deterministic Phase Retrieval: a Green’s Function Solution.,” *Journal of the Optical Society of America*, vol. 73, no. 11, pp. 1434–1441, 1983.
- [101] C. Zuo, J. Li, J. Sun, Y. Fan, J. Zhang, L. Lu, R. Zhang, B. Wang, L. Huang, and Q. Chen, “Transport of intensity equation: a tutorial,” *Optics and Lasers in Engineering*, no. December 2019, 2020.
- [102] C. Zuo, Q. Chen, W. Qu, and A. Asundi, “Noninterferometric single-shot quantitative phase microscopy,” *Optics Letters*, vol. 38, no. 18, p. 3538, 2013.
- [103] P. Genevet, F. Capasso, F. Aieta, M. Khorasaninejad, and R. Devlin, “Recent advances in planar optics: from plasmonic to dielectric metasurfaces,” *Optica*, vol. 4, no. 1, p. 139, 2017.
- [104] W. T. Chen, A. Y. Zhu, J. Sisler, Z. Bharwani, and F. Capasso, “A broadband achromatic polarization-insensitive metalens consisting of anisotropic nanostructures,” *Nature communications*, vol. 10, no. 1, pp. 1–7, 2019.
- [105] J. Engelberg, C. Zhou, N. Mazurski, J. Bar-David, A. Kristensen, and U. Levy, “Near-ir wide-field-of-view huygens metalens for outdoor imaging applications,” *Nanophotonics*, vol. 9, no. 2, pp. 361–370, 2020.
- [106] W. T. Chen, A. Y. Zhu, and F. Capasso, “Flat optics with dispersion-engineered metasurfaces,” *Nature Reviews Materials*, vol. 5, no. 8, pp. 604–620, 2020.
- [107] N. M. Estakhri and A. Alu, “Wave-front transformation with gradient metasurfaces,” *Physical Review X*, vol. 6, no. 4, p. 041008, 2016.
- [108] J. Yang, D. Sell, and J. A. Fan, “Freeform Metagratings Based on Complex Light Scattering Dynamics for Extreme, High Efficiency Beam Steering,” *Annalen der Physik*, vol. 530, no. 1, pp. 1–8, 2018.
- [109] Z.-L. Deng, J. Deng, X. Zhuang, S. Wang, T. Shi, G. P. Wang, Y. Wang, J. Xu, Y. Cao, X. Wang, *et al.*, “Facile metagrating holograms with broadband and extreme angle tolerance,” *Light: Science & Applications*, vol. 7, no. 1, pp. 1–8, 2018.
- [110] Y. Ni, S. Chen, Y. Wang, Q. Tan, S. Xiao, and Y. Yang, “Metasurface for structured light projection over 120° field of view,” *Nano Letters*, vol. 20, no. 9, pp. 6719–6724, 2020.
- [111] X. Ni, A. V. Kildishev, and V. M. Shalaev, “Metasurface holograms for visible light,” *Nature communications*, vol. 4, no. 1, pp. 1–6, 2013.
- [112] H. Gao, Y. Wang, X. Fan, B. Jiao, T. Li, C. Shang, C. Zeng, L. Deng, W. Xiong, J. Xia, *et al.*, “Dynamic 3d meta-holography in visible range with large frame number and high frame rate,” *Science advances*, vol. 6, no. 28, p. eaba8595, 2020.
- [113] F. Ding, B. Chang, Q. Wei, L. Huang, and X. Guan, “Versatile Polarization Generation and Manipulation Using Dielectric Metasurfaces,” vol. 2000116, pp. 1–7, 2020.
- [114] D. Lee, J. Gwak, T. Badloe, S. Palomba, and J. Rho, “Metasurfaces-based imaging and applications: From miniaturized optical components to functional imaging platforms,” *Nanoscale Advances*, vol. 2, no. 2, pp. 605–625, 2020.
- [115] M. Khorasaninejad, W. T. Chen, R. C. Devlin, J. Oh, A. Y. Zhu, and F. Capasso, “Metalenses at visible wavelengths: Diffraction-limited focusing and subwavelength resolution imaging,” *Science*, vol. 352, no. 6290, pp. 1190–1194, 2016.

- [116] A. L. Holsteen, D. Lin, I. Kauvar, G. Wetzstein, and M. L. Brongersma, “A Light-Field Metasurface for High-Resolution Single-Particle Tracking,” *Nano Letters*, vol. 19, no. 4, pp. 2267–2271, 2019.
- [117] H. Kwon, E. Arbabi, S. M. Kamali, M. Faraji-Dana, and A. Faraon, “Computational complex optical field imaging using a designed metasurface diffuser,” *Optica*, vol. 5, no. 8, p. 924, 2018.
- [118] K. Zangeneh Kamali, L. Xu, J. Ward, K. Wang, G. Li, A. E. Miroshnichenko, D. Neshev, and M. Rahmani, “Reversible Image Contrast Manipulation with Thermally Tunable Dielectric Metasurfaces,” *Small*, vol. 15, no. 15, pp. 1–6, 2019.
- [119] N. A. Rubin, G. D’Aversa, P. Chevalier, Z. Shi, W. T. Chen, and F. Capasso, “Matrix Fourier optics enables a compact full-Stokes polarization camera,” *Science*, vol. 364, no. 6448, 2019.
- [120] P. Bouchal, L. Štrbková, Z. Dostál, R. Chmelík, and Z. Bouchal, “Geometric-Phase Microscopy for Quantitative Phase Imaging of Isotropic, Birefringent and Space-Variant Polarization Samples,” *Scientific Reports*, vol. 9, no. 1, pp. 1–11, 2019.
- [121] P. Huo, C. Zhang, W. Zhu, M. Liu, S. Zhang, S. Zhang, L. Chen, H. J. Lezec, A. Agrawal, Y. Lu, and T. Xu, “Photonic Spin-Multiplexing Metasurface for Switchable Spiral Phase Contrast Imaging,” *Nano Letters*, vol. 20, no. 4, pp. 2791–2798, 2020.
- [122] J. Zhang, Q. Chen, J. Sun, L. Tian, and C. Zuo, “On a universal solution to the transport-of-intensity equation,” *Optics Letters*, vol. 45, no. 13, pp. 3649–3652, 2020.
- [123] D. G. Voelz, *Computational Fourier Optics: A MATLAB Tutorial*. Bellingham, Washington USA: SPIE Press, 2011.
- [124] D. Paganin, A. Barty, P. McMahon, and K. Nugent, “Quantitative phase-amplitude microscopy . III .,” *Journal of Microscopy*, vol. 214, no. 1, pp. 51–61, 2004.
- [125] A. Komar, Z. Fang, J. Bohn, J. Sautter, M. Decker, A. Miroshnichenko, T. Pertsch, I. Brener, Y. S. Kivshar, I. Staude, and D. N. Neshev, “Electrically tunable all-dielectric optical metasurfaces based on liquid crystals,” *Applied Physics Letters*, vol. 110, no. 7, 2017.
- [126] C. Zou, I. Staude, and D. N. Neshev, “Tunable metasurfaces and metadevices,” *Dielectric Metamaterials*, pp. 195–222, 2020.
- [127] S. Q. Li, X. Xu, R. M. Veetil, V. Valuckas, R. Paniagua-Domínguez, and A. I. Kuznetsov, “Phase-only transmissive spatial light modulator based on tunable dielectric metasurface,” *Science*, vol. 364, no. 6445, pp. 1087–1090, 2019.
- [128] G. K. Shirmanesh, R. Sokhoyan, P. C. Wu, P. C. Wu, H. A. Atwater, and H. A. Atwater, “Electro-optically Tunable Multifunctional Metasurfaces,” *ACS Nano*, vol. 14, no. 6, pp. 6912–6920, 2020.

A Appendix A: Multiple-plane phase retrieval

A.1 Multiple-plane phase retrieval

The use of multiple data (i.e. several intensity measurements) has been shown to be a robust technique for phase measurement since more data are available for reconstruction. Multiple-plane phase retrieval utilizes multiple intensity measurements as constraints in an iterative algorithm based on the (RS) diffraction formula Section 2.2.2 [99]. Figure A.1 shows the optical setup for the (a) multiple-plane phase retrieval (MPR) technique in comparison with the (b) conventional TIE and (c) MS-based TIE. The axial propagation of the beam is sampled by displacing the camera along the propagation direction multiple times.

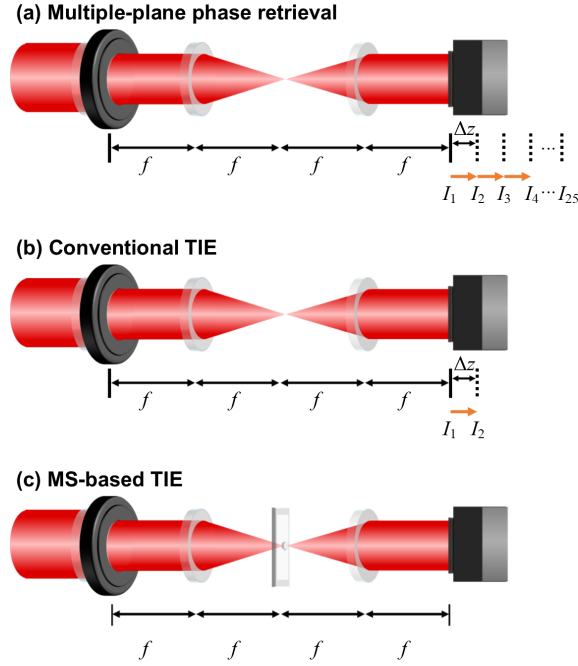


Figure A.1: **Schematic of the optical setup to obtain multiple intensities using noninterferometric methods.** (a) Multiple-plane phase retrieval, (b) conventional TIE and (C) metasurface-based TIE.

For the calculation, the algorithm starts with a guess phase φ_1 at the first measurement plane. The complex field is written as $u_1 = \sqrt{I_1}e^{i\varphi_1}$, where I_1 is the recorded image at the first recording plane. Using the RS formula, u_1 is numerically propagated to the next measurement plane to calculate u_2 , whose phase is retained while its amplitude is updated with $\sqrt{I_2}$. These steps are repeated

until the last measurement plane and comprise the forward process. The second half of the iteration is implemented by doing the same steps but in the backward direction and starting from the last measurement plane. The iterative calculation terminates when the current phase estimate approximates the previous one, as shown in Figure A.2. In our implementation, 25 intensity measurements were recorded. The first intensity measurement was taken at the image plane, while the succeeding intensities were obtained by displacing the camera by 10 mm.

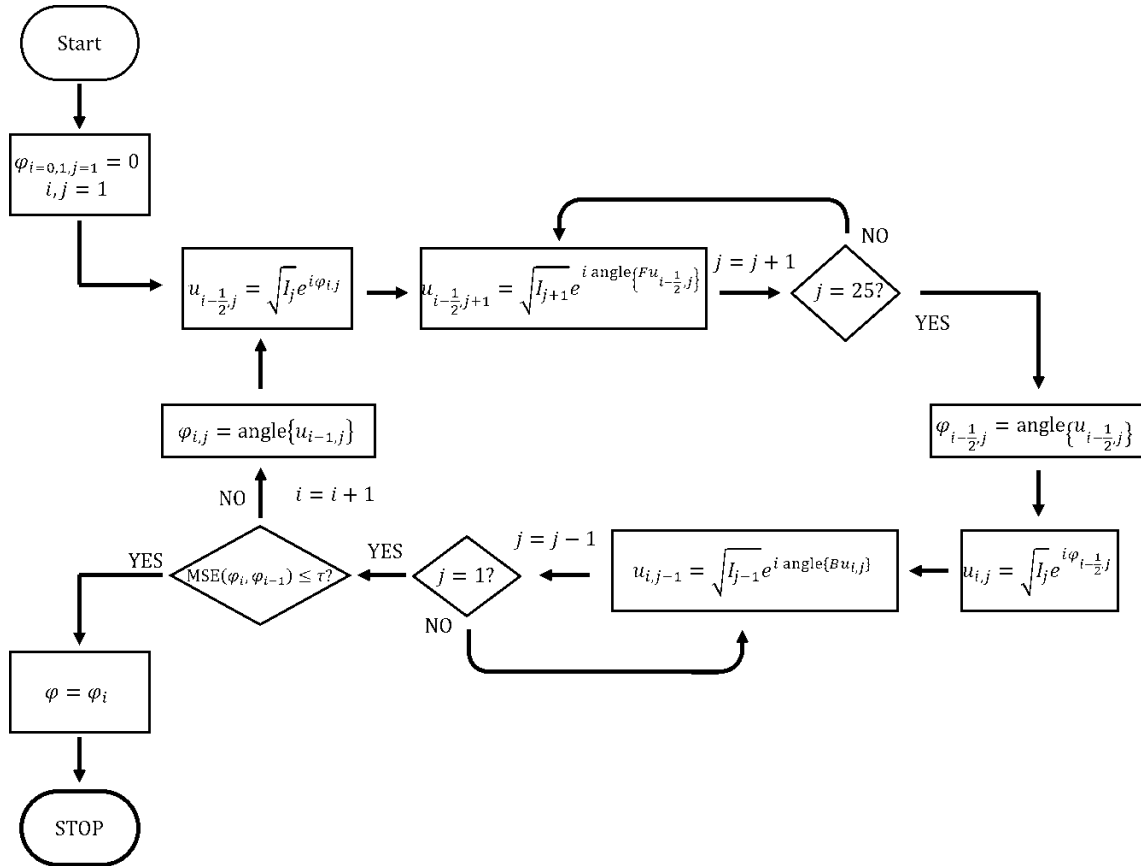


Figure A.2: Iterative phase retrieval using multiple intensity constraints.

To be published in Optics Letters:

Title: Nonlinear optical vortex coronagraph

Authors: Peter John Rodrigo, Einstom Engay

Accepted: 14 February 20

Posted 18 February 20

DOI: <https://doi.org/10.1364/OL.383311>

© 2020 Optical Society of America

Published by

OSA[®]

The Optical Society

Nonlinear optical vortex coronagraph

EINSTOM ENGAY AND PETER JOHN RODRIGO*

DTU Fotonik, Department of Photonics Engineering, Technical University of Denmark, Frederiksborgvej 399, 4000 Roskilde, Denmark

*Corresponding author: pejr@fotonik.dtu.dk

Received XX Month XXXX; revised XX Month, XXXX; accepted XX Month XXXX; posted XX Month XXXX (Doc. ID XXXXX); published XX Month XXXX

A nonlinear optical vortex coronagraph (n-OVC) based on sum-frequency generation (SFG) in a periodically poled lithium niobate (PPLN) crystal is presented. We demonstrate an n-OVC by mixing the image of an on-axis point source ($\lambda_s = 1.6 \mu\text{m}$) inside the PPLN crystal with a pump beam ($\lambda_p = 1064 \text{ nm}$) imprinted with a helical phase profile from a vector vortex mask (topological charge $l = 2$). Due to quasi-phase matching and orbital angular momentum conservation, a coronagraphic image is produced at the SFG wavelength ($\lambda_{\text{up}} \sim 630 \text{ nm}$). We validate that n-OVC is tunable to signal wavelength but only requires a vortex mask operating at the pump wavelength. The acceptance bandwidth of the SFG process provides the n-OVC a degree of achromaticity even with a monochromatic vortex mask. The n-OVC exhibits an inner working angle of $\sim \lambda_s/D$ and an experimental contrast of 10^{-4} at $3\lambda_s/D$.

© 2020 Optical Society of America

<http://dx.doi.org/10.1364/OL.99.099999>

Optical vortex coronagraphy (OVC) is a high-contrast imaging technique that allows for the direct detection of faint stellar companions [1,2]. OVC utilizes a helical phase (vortex) mask in a $4f$ imaging setup to address two of the main challenges in exoplanet detection, namely: the large flux ratio between the planet and its parent star, and their close angular proximity to each other. Along with other phase-based coronagraphic techniques, OVC inherently provides an advantage over amplitude-type coronagraphs as it allows for starlight attenuation while having minimal effect on the planetary signal even for small angular separation between the star and the planet.

The vortex masks (VM) used in OVC can either be (1) a scalar VM [2–4] or (2) a vector VM [1]. A scalar VM applies the appropriate phase profile by azimuthal variation in its optical thickness. On the other hand, a vector VM relies on polarization manipulation, which has been implemented either with spatially varying liquid-crystal polymer (LCP) half-wave plates [5–8] or with masks based on form birefringence [1,9]. However, even with the technological developments in fabrication, broadband operation remains to be one of the challenges in manufacturing vortex masks. To produce achromatic masks, serial stacking of

scalar VMs has been reported [10,11]. Such a multilayer design can be achieved more easily with vector VMs using advanced fabrication techniques [12].

The key spectral regions of interest in planetary observations are the near-infrared (NIR) and mid-infrared (MIR) domains as they allow for the determination of the composition of a planet's atmosphere. Additionally, the more favorable star-planet flux ratio [13] and the better performance of available adaptive optics in the NIR and MIR than in the visible range permit the actual implementation of OVC in ground-based and space-based telescopes. Present OVCs operating in the MIR, however, employ VMs requiring specialized fabrication process and MIR cameras with sophisticated cooling systems [9].

In this Letter, we propose a nonlinear optical vortex coronagraph (n-OVC) that has the following valuable properties: (1) spectral translation, which enables the VM to operate only at one fixed (pump) wavelength, (2) tunability to signal center wavelength, and (3) achromatic operation without the need for an achromatic VM. Furthermore, an n-OVC extended to MIR operation has the advantages of circumventing the need for both a MIR VM and a MIR camera (e.g., MCT or microbolometer array).

The schematic diagram of our proposed n-OVC is compared to that of its linear counterpart in Fig. 1. In the conventional OVC shown in Fig. 1(a), a VM acts as a Fourier filter and imparts an azimuthal phase ramp, $\exp(il\phi)$, onto the Airy pattern formed at the back focal plane of lens L_1 , where l is the integer topological charge of the VM. For an on axis point source (e.g., parent star) filtered through a narrow bandpass, the resulting field distribution in the pupil plane (using Fourier optics [14]) is given by

$$E_{\text{OVC}}(r, \theta) \propto \mathfrak{F}^{-1}\{\mathfrak{F}\{\text{circ}(2r/D)\} \cdot \exp(il\phi)\}, \quad (1)$$

where D is the entrance pupil diameter and (r, θ) are the polar coordinates. \mathfrak{F} is the Fourier transform operator while \mathfrak{F}^{-1} is its inverse. For a VM with $l = 2$, light inside the geometrical pupil area, $r < R'$, is nulled and the field profile outside is [1,2]

$$E_{\text{OVC}}(r, \theta) = E_1 \exp(i2\theta)(R'/r)^2, \quad r > R' \quad (2)$$

where E_1 is a constant and $R' = (D/2)(f_2/f_1)$ is the radius of the pupil plane image of the entrance aperture. The pupil plane profile is a dark disk of radius R' surrounded by a bright halo of light that decreases in irradiance radially outwards. In combination with a slightly undersized Lyot stop of radius $R_{\text{Lyot}} < R'$, the VM can in principle perfectly eliminate the on-axis starlight. Additional

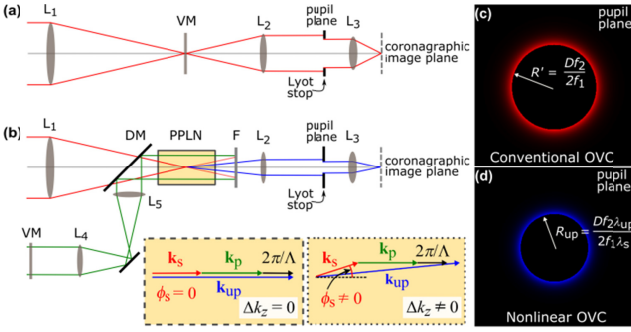


Fig. 1. (Color online) Schematic diagram comparison of two coronagraphs: (a) conventional OVC and (b) our proposed n-OVC implemented with a PPLN crystal. In n-OVC, coronagraphic and off-axis images are produced at the SFG wavelength (drawn as blue rays) instead of the signal wavelength (red rays) but the vortex mask (VM) operates at the pump wavelength (green rays). In (b), two insets (dashed and dotted boxes) illustrate two possible k -vector relationships inside the PPLN crystal for the case of a monochromatic input signal. Considering on-axis point sources and VM of charge $l = 2$, calculated irradiance profiles in the pupil plane of the OVC and the n-OVC are shown in (c) and (d), respectively. L_1 - L_5 , lenses; DM, dichroic mirror; F, spectral filters that block light except for the SFG beam.

mutually incoherent off-axis point sources, whose respective images elude the VM center, only experience negligible attenuation and deflection. Hence, an OVC enables high-contrast detection of faint companions observed in the coronagraphic image plane, i.e., in the focal plane of lens L_3 as shown in Fig. 1(a).

Our proposed n-OVC relies on a sum-frequency generation (SFG) process and its working principles are described using the theory of upconversion imaging [15]. In Fig. 1(b), a $4f$ upconversion imaging system is formed by the periodically poled lithium niobate (PPLN) crystal and the two lenses L_1 and L_2 , separated by the sum of their focal lengths f_1 and f_2 , respectively. Using paraxial and slowly varying amplitude approximations, the output field E_{up} generated in the PPLN crystal is given by [16,17]

$$\partial E_{\text{up}}/\partial z = 2i\omega_{\text{up}}^2 d_{\text{eff}} E_s E_p \exp(-i\Delta k_z z)/(k_{\text{up}} c^2), \quad (3)$$

where E_s and E_p are the signal and pump fields in the crystal, ω_{up} is the angular frequency of the field E_{up} , d_{eff} is the crystal's effective nonlinear coefficient, and c is the speed of light in vacuum. Δk_z is the longitudinal phase mismatch of the SFG process [15]: $\Delta k_z(\phi_s, \Lambda, T) = k_{\text{up}} - k_p - k_s - 2\pi/\Lambda + k_s(1 - k_s/k_{\text{up}})\phi_s^2$, where $k_j = k_j(T)$ (subscript $j = s, p$ or up denotes signal, pump and upconverted field, respectively and T is the PPLN temperature) are the collinear k -vector magnitudes inside the PPLN crystal with poling period Λ . The internal angle ϕ_s refers to the angular direction of the input signal k -vector relative to the z -axis – see insets in Fig. 1 (b). A combination of Λ and T is selected such that phase match is achieved for $\phi_s = 0$ (i.e., $\Delta k_z = 0$ and conversion efficiency η is maximized at the center of the image). η has a known profile given by $\eta_0 \text{sinc}^2(\Delta k_z(\phi_s)L/2)$ [15]. For $\phi_s \neq 0$, η deviates from the maximum value η_0 due to phase mismatch ($\Delta k_z \neq 0$), and this sets an upper limit to the pupil plane radius in which a signal can achieve high conversion efficiency.

It has been shown in previous studies that, in an SFG process, orbital angular momentum (OAM) is conserved between the input

and output fields for pump and signal fields with Rayleigh lengths longer than L [18,19]. This is also the case in our n-OVC where the upconverted field inherits the OAM of the pump field (signal OAM is zero). Taking into account all of these physical processes, the upconverted output field in the pupil plane for an on-axis narrowband point source whose image is mixed with a charge- l vortex pump in the PPLN crystal is given by

$$E_{\text{n-OVC}}(r, \theta) \propto [\mathfrak{F}^{-1}\{\mathfrak{F}\{\text{circ}(2r/D)\} \cdot \exp(i\ell\theta)\} \otimes F(r, \theta)] \cdot \text{sinc}(\Delta k_z(\phi_s)L/2), \quad (4)$$

where \otimes is the convolution operator and $\phi_s = \phi_s(r)$ scales linearly with r through simple refraction rules. Here, $F(r, \theta)$ is the Fourier transform of a function describing the PPLN aperture whose finite extent can also serve as an apodizing filter. $F(r, \theta)$ is approximated as a delta-function when the Airy profile is sufficiently contained within the crystal cross-section. For $l = 2$, $E_{\text{n-OVC}} = 0$ inside a circle of radius $r = R_{\text{up}}$. Outside the circle,

$$E_{\text{n-OVC}}(r, \theta) = E_1^{(\text{up})} \exp(i2\theta) (R_{\text{up}}/r)^2 \cdot \text{sinc}(\Delta k_z(\phi_s)L/2), \quad r > R_{\text{up}}. \quad (5)$$

$R_{\text{up}} = (D/2)(f_2/f_1)(\lambda_{\text{up}}/\lambda_s)$ is the radius of the upconverted image of the entrance pupil. The factor (f_2/f_1) is the standard (de)magnification of a $4f$ imaging setup while $(\lambda_{\text{up}}/\lambda_s)$ is due to the upconversion process. Thus, the halo irradiance pattern, proportional to the squared modulus of $E_{\text{n-OVC}}$ in Eq. (5), is similar to that of a conventional OVC but with an additional image demagnification due to the $(\lambda_{\text{up}}/\lambda_s)$ factor and a modulation by a sinc-squared envelope that depends on L and $\Delta k_z(\phi_s)$. The field in Eq. (5) may be convolved with $F(r, \theta)$ to include the effect of the crystal's finite aperture. Figures 1(c) and 1(d) compare the theoretical halo images of the linear OVC and the proposed n-OVC. The phase mismatch $\Delta k_z(\phi_s(r))$ provides a design criterion to check that the upconverted halo is within the central lobe of the sinc-squared envelope. In this way, off-axis point sources not aligned with the phase singularity at the center of the pump beam generate SFG images in the coronagraphic plane with high efficiency and narrow point-spread functions (PSF). Otherwise, the envelope function would effectively behave as a mask smaller than the Lyot stop in the pupil plane – reducing the overall conversion efficiency and increasing the IWA of the n-OVC.

To experimentally demonstrate the n-OVC, the optical setup shown in Fig. 1(b) was constructed. The PPLN crystal's length is $L = 10$ mm, its cross-section is 1×1 mm² and its period is $\Lambda = 11.8$ μm . The pump and signal wavelengths are $\lambda_p = 1064$ nm and $\lambda_s = 1575$ nm. The crystal temperature was set to $T = 130$ $^\circ\text{C}$ to satisfy collinear phase matching, $\Delta k_z(\phi_s = 0) = 0$. The focal lengths of the lenses used in the setup are $f_1 = f_5 = 60$ mm, $f_2 = 200$ mm, $f_3 = 250$ mm and $f_4 = 300$ mm. We used a VM ($l = 2$) for 1064 nm operation made of spatially varying half-wave plate (SVHWP) that are based on LCP (between two quarter wave plates). In this vortex VM, a central disorientation or defect is encountered due to failure of the LCP molecules comprising the VM to form the correct orientation near the center [5,8]. This results in an inaccurate imprinting of the vortex phase profile onto the pump and consequently the SFG beam. A central leakage in the SFG beam occurs in the PPLN but can be reduced by ensuring that the VM defect size imaged in the PPLN is well within the main lobe of the focused signal beam [5]. Fast Fourier Transform based simu-

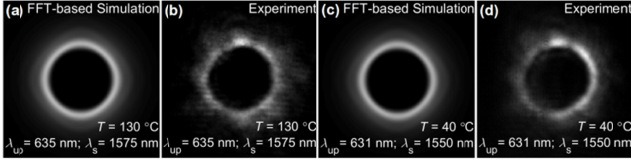


Fig. 2. Blurring effect of the finite crystal aperture on the upconverted halo intensity pattern and tunability of the n-OVC to different signal wavelengths. Numerical and experimental halo images for (a)-(b) $\lambda_s = 1575$ nm and (c)-(d) $\lambda_s = 1550$ nm. T , PPLN temperature used.

lations were implemented in MATLAB to illustrate the effect of the finite 1×1 mm² PPLN aperture and the tunability of the n-OVC to different signal wavelengths even though the VM is designed only for the pump wavelength. Parameters were chosen to match those in the experiment. A collimated Gaussian signal beam of radius $w_s = 1$ mm incident on a pupil of diameter $D = 1$ mm is used. The Gaussian pump radius is $w_0 = 1$ mm in the PPLN crystal. For $\lambda_s = 1575$ nm, the numerically and experimentally obtained halo images are shown in Figs. 2 (a)-(b). In good qualitative agreement, the numerical and experimental irradiance profiles exhibit the blurring effect due to the finite size of the crystal aperture, acting as a low-pass filtering element. The blurring can therefore be reduced by increasing the number of rings of the Airy profile that fit into the PPLN aperture. In the interest of minimizing the relative size of the defect, however, we chose to keep the central lobe of the Airy profile relatively large (i.e., Airy main lobe radius of 115 μ m). Figures 2 (c)-(d) show that the n-OVC can be adapted to work for a different signal wavelength provided that the phase match condition is satisfied. For the same λ_p and Λ but with a different signal wavelength $\lambda_s = 1550$ nm, this condition is met by setting the crystal temperature to $T = 40$ °C. The halo images observed in the upconverted irradiance validate the successful transfer of the OAM from the pump onto the SFG field. Alternatively, a PPLN crystal with a different period Λ can also be employed to tune the n-OVC to work for a different λ_s . This spectral translation property of the n-OVC allows for extending the use of monochromatic VMs (indirectly) to other wavelengths. We measured an achromaticity of about 1 nm at either 1575 nm or 1550 nm operation of the n-OVC. This matches the PPLN crystal's acceptance bandwidth given by the full-width-half-maximum of the main lobe of $\text{sinc}^2(\Delta k_z L/2)$ as a function of λ_s . The bandwidth can be increased using a shorter L . Both center wavelength λ_s and n-OVC bandwidth can be adjusted by appropriate choice of Λ , T , λ_p and nonlinear material [20]. Intriguingly, an n-OVC can effectively facilitate tunable and/or broadband operation even with a VM operating at a narrow-linewidth pump wavelength.

The performance of the n-OVC was evaluated using two common metrics: peak-to-peak (PTP) attenuation and intensity contrast. PTP attenuation is the ratio of the PSF irradiance peak of the coronagraphic image to that of the off-axis image obtained by sufficient translation of the VM. On the other hand, intensity contrast was calculated by azimuthally averaging the pixel values of the rendered coronagraphic image or PSF normalized to the peak intensity of the off-axis image. The intensity contrast was plotted as a function of angular separation in λ_s/D units. To obtain the coronagraphic image, the upconverted field transmitted through a Lyot stop of radius $R_{\text{Lyot}} = 0.8R_{\text{up}}$ is focused by lens L_3 . A series of images was recorded using a 14-bit camera for three

different exposure times to capture the side lobes of the PSF. To remove electronic noise, a corresponding dark median background (DMB) was obtained for each exposure time by capturing images while the upconverted light is blocked. The DMB was then subtracted from the raw images. For the same settings, off-axis images were also obtained for incremental translations of the VM from its optimal position. Finally, the coronagraphic and off-axis images were rendered by adding all DMB-subtracted images accounting for the camera exposure time used.

The simulated and experimental PTP attenuation plots are shown in Fig. 3 where a 6×10^{-3} level is achieved experimentally at the optimal position of the vortex mask. A considerable deviation is seen between the numerical PTP and the experimental plot that can be attributed to factors present in the experiment but excluded in the simulation such as optical aberrations, tiny misalignment and the VM central defect [5]. Several adaptive techniques have been implemented to compensate for such defect, for example, by covering the central defect with a very small stop [5,8]. One of the advantages therefore of the proposed n-OVC configuration is the freedom to choose f_4 and f_5 that allows for size reduction of the defect's image in the PPLN. In our case, a $5\times$ demagnification was implemented in the setup. From these plots, the inner working angle (IWA) which is arbitrarily defined as the 50% throughput angle is determined to be within the desired λ/D level. IWA provides one of the measures of the coronagraph's detection limit giving an indication of how close to a parent star a companion should be such that it can still be detected by the system.

Figure 4(a) shows the azimuthally averaged profiles of the rendered coronagraphic and off-axis images for an optimally aligned VM, Fig. 4(b), and a translated VM with $3.1\lambda_s/D$ angular offset, Fig. 4(c). A contrast of 10^{-3} was experimentally reached at $1.5\lambda_s/D$; 10^{-4} at $3\lambda_s/D$; as shown by dotted lines in Fig. 4(a). Similar to the PTP attenuation plots in Fig. 3, deviations are also evident in the numerical and experimental radial profiles in Fig. 4(a). A much higher contrast is possible with tophat signal pupil plane profile (i.e., starlight), 5×5 mm² PPLN crystal aperture and a defect-free VM, which is the case numerically simulated in Fig. 4(a).

To assess the sensitivity of the n-OVC employing a silicon based camera, the internal conversion efficiency η of the SFG process must be considered. Since the Rayleigh lengths of both pump and signal fields in the PPLN crystal are larger than L , we can estimate η using plane-wave approximation [15,21]:

$$\eta = P_{\text{up}}\lambda_{\text{up}}/(P_s\lambda_s) = 8\pi^2 d_{\text{eff}}^2 L^2 I_p / (\epsilon_0 c n_s n_p n_{\text{up}} \lambda_{\text{up}} \lambda_s), \quad (6)$$

where P_{up} and P_s are the upconverted and signal power, respectively, $d_{\text{eff}} = 14 \times 10^{-12}$ m/volt for MgO-doped PPLN crystal, I_p is the pump intensity, n_j is the refractive index of lithium niobate at wavelength λ_j , and ϵ_0 is the permittivity. In our n-OVC

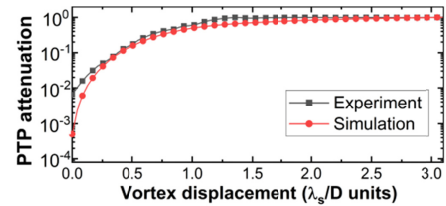


Fig. 3. (Color online) Measured and numerically simulated PTP attenuation as a function of the VM angular displacement in λ_s/D units. A Gaussian signal profile truncated by the entrance pupil is assumed.

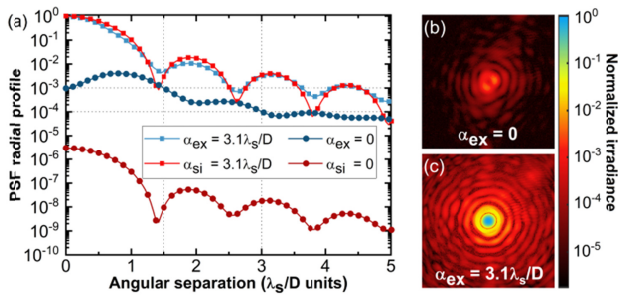


Fig. 4. (Color online) (a) Azimuthally averaged PSFs at 635 nm in the coronagraphic image plane experimentally (blue curves) and numerically (red curves; top-hat signal profile) obtained by our n-OVC for a 1575 nm point source with VM angular offset $\alpha = 3.1\lambda_s/D$ and $\alpha = 0$. Experimental (b) on-axis and (c) off-axis PSFs in logarithmic scale.

demonstration using MgO:PPLN crystal, we achieved a measured $\eta = 2 \times 10^{-5}$ due to the use of a relatively low pump power $P_p = 1$ W. This is in fair agreement with the theoretical value based on Eq. (6), i.e., $\eta = 3 \times 10^{-5}$. Internal conversion efficiency can be significantly increased by a combination of strategies including: (1) increasing the pump power P_p , (2) decreasing the pump beam radius w_0 to increase the pump power density, and (3) using a longer crystal. The first approach is straightforward and due to high transparency of the PPLN crystal (and high-quality anti-reflection coatings on end facets), pump powers in the order of 10-100 W could significantly increase η . The second strategy can be used, especially for modest pump powers of a few Watts. However, reduction in w_0 means that efficient upconversion in the PPLN crystal is going to be limited in a smaller 2D Gaussian envelope. This can cause halo blur and reduce the n-OVC discovery space or the ability to image planets with larger angular separation from their parent star. The third, approach is also straightforward since $\eta \propto L^2$, but the increase in conversion efficiency has corresponding penalties of reducing both signal acceptance bandwidth and signal acceptance angle. The former drawback has an obvious effect of degrading the broadband operation of the n-OVC, and the latter has the potential consequence of broadening the image plane PSF, thereby increasing the IWA of the coronagraph. Using a combination of these strategies, we estimate that a conversion efficiency of 0.2% is readily achievable. Even at this efficiency, an n-OVC for MIR operation based on low-noise silicon camera is already estimated to reach a sensitivity that can compete with that of a conventional MIR OVC using state-of-the-art cryogenically cooled camera, e.g., based on MCT detectors, which are hampered by the inherently high level of thermal noise [22]. In [22], it was found that, even at 6% upconversion efficiency, a PPLN-based frequency converter combined with a silicon detector can achieve a sensitivity 50 times that of a cooled MCT detector. One of the major benefits of the n-OVC is in the ability to utilize a high-quality VM operating at a relatively shorter (pump) wavelength – and, because the need for an achromatic VM is circumvented, high phase profile accuracy and superior anti-reflection coating quality are easily achieved. Secondly, MCT cameras with sophisticated cooling requirements are avoided.

In conclusion, we presented a theoretical (Fourier optics) model and the first laboratory demonstration of a nonlinear optical vortex coronagraph. The presently achieved contrast of our n-OVC is 10^{-4} at $3\lambda/D$. Simulations suggest that contrast orders of

magnitude better is possible. Utilizing OAM conservation in an SFG process, the n-OVC facilitates tunable and/or achromatic coronagraphy even with the use of a vortex mask designed for narrowband operation. The n-OVC can be extended to broadband MIR operation (e.g., L'-band [13]) and use other nonlinear crystals – potentially with signal bandwidth between 0.1 to 1 μm [20]. This is highly coveted for direct imaging of exoplanets but obviating the need for cryogenically cooled cameras and achromatic MIR VMs.

Funding. Novo Nordisk Fonden (NNF16OC0021948) for E. Engay.

Disclosures. The authors declare no conflicts of interest.

REFERENCES

1. D. Mawet, P. Riaud, O. Absil, and J. Surdej, *Astrophys. J.* **633**, 1191 (2005).
2. G. Foo, D. M. Palacios, and G. A. Swartzlander, *Opt. Lett.* **30**, 3308 (2005).
3. J. H. Lee, G. Foo, E. G. Johnson, and G. A. Swartzlander, *Phys. Rev. Lett.* **97**, 6 (2006).
4. G. A. Swartzlander, E. L. Ford, R. S. Abdul-Malik, L. M. Close, M. A. Peters, D. M. Palacios, and D. W. Wilson, *Opt. Express* **16**, 10200 (2008).
5. D. Mawet, E. Serabyn, K. Liewer, C. Hanot, S. McEldowney, D. Shemo, and N. O'Brien, *Opt. Express* **17**, 1902 (2009).
6. D. Mawet, E. Serabyn, K. Liewer, R. Burruss, J. Hickey, and D. Shemo, *Astrophys. J.* **709**, 53 (2010).
7. E. Serabyn, D. Mawet, and R. Burruss, *Nature* **464**, 1018 (2010).
8. E. Serabyn, C. M. Prada, P. Chen, and D. Mawet, *J. Opt. Soc. Am. B* **36**, D13 (2019).
9. C. Delacroix, O. Absil, P. Forsberg, D. Mawet, V. Christiaens, M. Karlsson, A. Boccaletti, P. Baudoz, M. Kuittinen, I. Vartiainen, J. Surdej, and S. Habraken, *Astron. Astrophys.* **553**, A98 (2013).
10. G. A. Swartzlander, *Opt. Lett.* **31**, 2042 (2006).
11. G. Ruane, D. Mawet, A. J. E. Riggs, and E. Serabyn, *Proc. SPIE* **11117**, 111171F (2019).
12. D. Mawet, N. Murakami, C. Delacroix, E. Serabyn, O. Absil, N. Baba, J. Baudrand, A. Boccaletti, R. Burruss, R. Chipman, P. Forsberg, S. Habraken, S. Hamaguchi, C. Hanot, A. Ise, M. Karlsson, B. Kern, J. Krist, A. Kuhnert, M. Levine, K. Liewer, S. McClain, S. McEldowney, B. Mennesson, D. Moody, H. Murakami, A. Niessner, J. Nishikawa, N. O'Brien, K. Oka, P. Park, P. Piron, L. Pueyo, P. Riaud, M. Sakamoto, M. Tamura, J. Trauger, D. Shemo, J. Surdej, N. Tabirian, W. Traub, J. Wallace, and K. Yokochi, *Proc. SPIE* **8151**, 815108 (2011).
13. E. Serabyn, E. Huby, K. Matthews, D. Mawet, O. Absil, B. Femenia, P. Wizinowich, M. Karlsson, M. Bottom, R. Campbell, B. Carlomagno, D. Defrère, C. Delacroix, P. Forsberg, C. G. Gonzalez, S. Habraken, A. Jolivet, K. Liewer, S. Lilley, P. Piron, M. Reggiani, J. Surdej, H. Tran, E. V. Catalán, and O. Wertz, *Astron. J.* **153**, 43 (2017).
14. J. W. Goodman, *Introduction to Fourier Optics, 3rd Ed.* (Roberts & Company Publishers, 2005).
15. A. Barh, P. J. Rodrigo, L. Meng, C. Pedersen, and P. Tidemand-Lichtenberg, *Adv. Opt. Photon.* **11**, 952 (2019).
16. S. K. Liu, C. Yang, S. L. Liu, Z. Y. Zhou, Y. Li, Y. H. Li, Z. H. Xu, G. C. Guo, and B. Sen Shi, *Phys. Rev. Appl.* **11**, 044013 (2019).
17. X. Qiu, F. Li, W. Zhang, Z. Zhu, and L. Chen, *Optica*, **5**, 208 (2018).
18. G. H. Shao, Z. J. Wu, J. H. Chen, F. Xu, and Y. Q. Lu, *Phys. Rev. A* **88**, 063827 (2013).
19. F. Steinlechner, N. Hermosa, V. Pruneri, and J. P. Torres, *Sci. Rep.* **6**, 21390 (2016).
20. A. Barh, C. Pedersen, and P. Tidemand-Lichtenberg, *Opt. Lett.* **42**, 1504 (2017).
21. V. G. Dmitriev, G. G. Gurzadyan, and D. N. Nikogosyan, *Handbook of Nonlinear Optical Crystals, 3rd Ed.* (Springer-Verlag, 1998).
22. R. L. Pedersen, L. Højstedt, A. Barh, L. Meng, and P. Tidemand-Lichtenberg, *IEEE Photon. Technol. Lett.* **31**, 681 (2019).

FULL REFERENCES

1. D. Mawet, P. Riaud, O. Absil, and J. Surdej, "Annular Groove Phase Mask Coronagraph," *Astrophys. J.* **633**, 1191–1200 (2005).
2. G. Foo, D. M. Palacios, and G. A. Swartzlander, "Optical vortex coronagraph," *Opt. Lett.* **30**, 3308–3310 (2005).
3. J. H. Lee, G. Foo, E. G. Johnson, and G. A. Swartzlander, "Experimental verification of an optical vortex coronagraph," *Phys. Rev. Lett.* **97**, 6–9 (2006).
4. G. A. Swartzlander, E. L. Ford, R. S. Abdul-Malik, L. M. Close, M. A. Peters, D. M. Palacios, and D. W. Wilson, "Astronomical demonstration of an optical vortex coronagraph," *Opt. Express* **16**, 10200–10207 (2008).
5. D. Mawet, E. Serabyn, K. Liewer, C. Hanot, S. McEldowney, D. Shemo, and N. O'Brien, "Optical Vectorial Vortex Coronagraphs using Liquid Crystal Polymers: theory, manufacturing and laboratory demonstration," *Opt. Express* **17**, 1902 (2009).
6. D. Mawet, E. Serabyn, K. Liewer, R. Burruss, J. Hickey, and D. Shemo, "The vector vortex coronagraph: Laboratory results and first light at Palomar observatory," *Astrophys. J.* **709**, 53–57 (2010).
7. E. Serabyn, D. Mawet, and R. Burruss, "An image of an exoplanet separated by two diffraction beamwidths from a star," *Nature* **464**, 1018–1020 (2010).
8. E. Serabyn, C. M. Prada, P. Chen, and D. Mawet, "Vector vortex coronagraphy for exoplanet detection with spatially variant diffractive waveplates," *J. Opt. Soc. Am. B* **36**, D13–D19 (2019).
9. C. Delacroix, O. Absil, P. Forsberg, D. Mawet, V. Christiaens, M. Karlsson, A. Boccaletti, P. Baudoz, M. Kuittinen, I. Vartiainen, J. Surdej, and S. Habraken, "Laboratory demonstration of a mid-infrared AGPM vector vortex coronagraph," *Astron. Astrophys.* **553**, A98 (2013).
10. G. A. Swartzlander, Jr., "Achromatic optical vortex lens," *Opt. Lett.* **31**, 2042 (2006).
11. G. Ruane, D. Mawet, A. J. E. Riggs, and E. Serabyn, "Scalar vortex coronagraph mask design and predicted performance," *Proc. SPIE* **11117**, 111171F (2019).
12. D. Mawet, N. Murakami, C. Delacroix, E. Serabyn, O. Absil, N. Baba, J. Baudrand, A. Boccaletti, R. Burruss, R. Chipman, P. Forsberg, S. Habraken, S. Hamaguchi, C. Hanot, A. Ise, M. Karlsson, B. Kern, J. Krist, A. Kuhnert, M. Levine, K. Liewer, S. McClain, S. McEldowney, B. Mennesson, D. Moody, H. Murakami, A. Niessner, J. Nishikawa, N. O'Brien, K. Oka, P. Park, P. Piron, L. Pueyo, P. Riaud, M. Sakamoto, M. Tamura, J. Trauger, D. Shemo, J. Surdej, N. Tabirian, W. Traub, J. Wallace, and K. Yokochi, "Taking the vector vortex coronagraph to the next level for ground- and space-based exoplanet imaging instruments: review of technology developments in the USA, Japan, and Europe," *Proc. SPIE* **8151**, 815108 (2011).
13. E. Serabyn, E. Huby, K. Matthews, D. Mawet, O. Absil, B. Femenia, P. Wizinowich, M. Karlsson, M. Bottom, R. Campbell, B. Carlomagno, D. Defrère, C. Delacroix, P. Forsberg, C. G. Gonzalez, S. Habraken, A. Jolivet, K. Liewer, S. Lilley, P. Piron, M. Reggiani, J. Surdej, H. Tran, E. V. Catalán, and O. Wertz, "The W. M. Keck Observatory Infrared Vortex Coronagraph and a First Image of Hip 79124 B," *Astron. J.* **153**, 43 (2017).
14. J. W. Goodman, *Introduction to Fourier Optics, 3rd Ed.* (Roberts & Company Publishers, 2005).
15. A. Barh, P. J. Rodrigo, L. Meng, C. Pedersen, and P. Tidemand-Lichtenberg, "Parametric Upconversion Imaging and its Applications : A Review," *Adv. Opt. Photon.* **11**, 952 (2019).
16. S. K. Liu, C. Yang, S. L. Liu, Z. Y. Zhou, Y. Li, Y. H. Li, Z. H. Xu, G. C. Guo, and B. Sen Shi, "Up-Conversion Imaging Processing with Field-of-View and Edge Enhancement," *Phys. Rev. Appl.* **11**, 044013 (2019).
17. X. Qiu, F. Li, W. Zhang, Z. Zhu, and L. Chen, "Spiral phase contrast imaging in nonlinear optics: seeing phase objects using invisible illumination," *Optica*, **5**, 208 (2018).
18. G. H. Shao, Z. J. Wu, J. H. Chen, F. Xu, and Y. Q. Lu, "Nonlinear frequency conversion of fields with orbital angular momentum using quasi-phase-matching," *Phys. Rev. A* **88**, 063827 (2013).
19. F. Steinlechner, N. Hermosa, V. Pruneri, and J. P. Torres, "Frequency conversion of structured light," *Sci. Rep.* **6**, 21390 (2016).
20. A. Barh, C. Pedersen, and P. Tidemand-Lichtenberg, "Ultra-broadband mid-wave-IR upconversion detection," *Opt. Lett.* **42**, 1504–1507 (2017).
21. V. G. Dmitriev, G. G. Gurzadyan, and D. N. Nikogosyan, *Handbook of Nonlinear Optical Crystals, 3rd ed.* (Springer-Verlag, 1998).
22. R. L. Pedersen, L. Høgstvedt, A. Barh, L. Meng, and P. Tidemand-Lichtenberg, "Characterization of the NEP of mid-infrared upconversion detectors," *IEEE Photon. Technol. Lett.* **31**, 681–684 (2019).



Interferometric detection of OAM-carrying Helico-conical beams

Einstom Engay^a, Andrew Bañas^{a,b}, Ada-Ioana Bunea^a, Stephen Daedalus Separa^b, Jesper Glückstad^{a,b,*}

^a DTU Fotonik, Department of Photonics Engineering, Technical University of Denmark, Ørsted Plads 343, DK-2800 kgs. Lyngby, Denmark

^b OptoRobotix ApS, DK-2000 Frederiksberg, Denmark

ARTICLE INFO

Keywords:

Diffractive optics
Physical optics
Interferometric imaging

ABSTRACT

Helico-conical beams (HCBs) are a class of orbital angular momentum (OAM)-carrying beams with spiral phase and intensity profiles. In this communication, we demonstrate the use of a common path interferometer (CPI) to phase-image incoming HCBs and directly detect their OAM-associated properties. The output intensity of the CPI is a direct mapping of the HCB's phase, hence both the topological charge value and sign manifest in the output intensity distribution. The topological charge value is calculated by fringe counting, while the helicity is determined by observing the intensity along the $\varphi = 0$ region. With our current CPI setup, we can firmly detect up to $l = \pm 20$. Higher values of l lead to a decrease in the fringe visibility, but this can in principle be improved by tailoring the parameters of the phase contrast filter (PCF) employed in the CPI. We present analytical expressions to optimize the CPI for HCB charge detection.

Beams with orbital angular momentum (OAM) have attracted much attention in recent years due to their potential applications in optical communications [1], high-resolution imaging [2] and optical trapping [3]. OAM arises from helical phased light beams with azimuthal phase dependence $\exp(il\varphi)$ [4], where the sign and value of l define the helicity and topological charge (TC) of the beam and φ is the azimuthal angle. Such beams include Laguerre–Gaussian (LG) and higher-order Bessel beams that carry an OAM equal to $l\hbar$ per photon. A striking feature of these OAM-carrying beams is the doughnut-shaped far-field intensity profile, which in a classical perspective results from the interference of the azimuthal component of the Poynting vectors.

Numerous methods have been proposed to introduce the helical phase to an incident fundamental Gaussian beam. These include employing fixed phase masks, spatial light modulators (SLMs) and metasurfaces, amongst others. Of equal importance for most applications is the detection of both the topological charge magnitude and sign of incoming unknown beams. The OAM manifests in the intensity distribution when the beam diffracts through slits and apertures [5,6], or when it is made to interfere with another beam [7]. Hence, from the diffraction or interference pattern, the OAM-content of the beam can be ascertained. Current methods for l -determination include employing amplitude diffractive apertures [8–11], interferometers [12–14] and spatial mode projections [15]. There has been a recent interest in employing phase-modulating elements because of their efficient detection of the topological charge. Pure-phase gratings have been reported to improve charge detection [16,17].

Helico-conical beams are a class of OAM-carrying beams whose phase function has a non-separable azimuthal and radial dependence [18,19],

$$\psi(r, \varphi) = l\varphi \left(K - \frac{r}{r_0} \right) \quad (1)$$

where K is between 0 and 1, and r_0 normalizes the radial coordinate r . HCBs have both twisted phase and intensity profiles in the far-field and maintain high photon concentration while still allowing higher topological charge values. By maintaining high photon densities even at higher values of l , HCBs may be suitable for applications that require large l 's [20]. Particularly, optical communication applications that could directly utilize the detected l values are candidates where using a HCB can be beneficial.

The generation of HCBs has already been demonstrated using SLMs [18,21], printed fork-type holograms [22] and plasmonic metasurfaces [23]. Far-field intensity observations have been conducted in the past using a $2f$ lens-configuration where the input HCB phase is encoded on a SLM placed behind a focusing lens. The spiral profile of the HCB-intensity can be detected by a camera positioned at the focal plane of the Fourier lens. Fig. 1 shows examples of HCB intensity profiles for $K = 0$ and for different topological charge values.

The propagation dynamics of HCBs have also been investigated using far-field intensity measurements [24,25]. Although it has been shown that the intensity-profiles laterally scale with l/r_0 [18], the reverse process of determining an unknown topological charge of the HCB from the spiral intensities can be a challenging task. This is

* Corresponding author.

E-mail address: jesper.gluckstad@fotonik.dtu.dk (J. Glückstad).

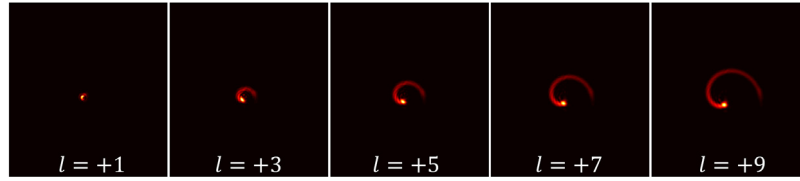


Fig. 1. Spiral far-field intensity profiles of simulated Helico-conical beams (HCBs) for $K = 0$, $l = +1, +3, +5, +7$ and $+9$. The lateral spiral profile scales linearly with the topological charge.

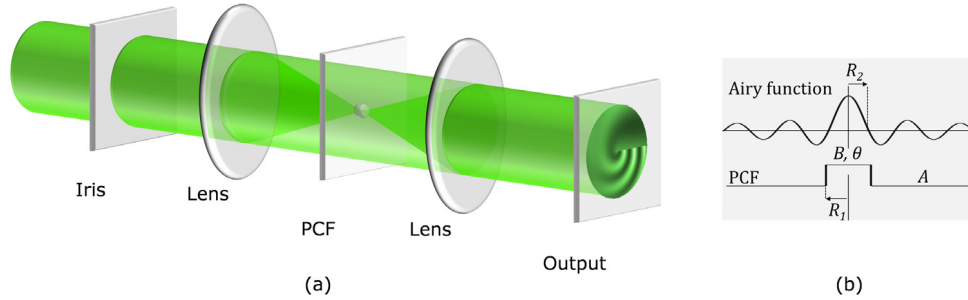


Fig. 2. (a) Schematic diagram of a $4f$ common path interferometer (CPI) with a phase contrast filter (PCF) in the optical Fourier plane. (b) PCF parameters overlaid on an Airy function, the Fourier transform of a circular input aperture. A and B are transmittance factors, θ is the phase shift introduced by the PCF, R_1 and R_2 are the radii of the PCF and Airy main lobe.

commonly encountered in optical communications, where from one end a transmitter sends out optical beams for data transmission to a receiver on the other end for detection and subsequent decoding with no prior information on the incoming beam. HCB topological charge detection from far-field intensity measurements would require all other initial parameters to be known, which is not the case in most OAM-experiments.

In this study, we employ a well-established common path interferometer (CPI) to image the phase of incoming HCBs and extract their OAM-associated properties that are otherwise difficult to obtain when observing only their far-field intensity distributions via a $2f$ lens-setup. We take advantage of the HCB's localized spatial far field intensity distribution when $K = 0$. A filtering phase element can therefore be reliably aimed at the center of the beam. The higher photon density also ensures that the effective CPI-reference wave has a comparable amplitude compared to the spatial frequency distribution of the HCB being imaged. Had we instead chosen to encode LG beams, the filtering element would coincide with the null region of their ring-shaped profile, resulting in poor contrast, especially at higher l values. As the CPI provides direct mapping of the HCB phase, the intensity output embodies the topological charge value and the helicity of the beam. Another advantage of the CPI is its relatively small footprint compared with other interferometry configurations such as the Mach-Zehnder or Michelson interferometers. To optimize HCB charge detection performance, we also analytically examine several parameters that affect the CPI's output contrast.

The CPI employed in this study is constructed around a $4f$ optical setup as shown in Fig. 2(a) [26,27]. A first Fourier transforming lens is used to separate the incoming beam into a focused light (zero-order) and an off-axis scattered light. A phase contrast filter (PCF) placed at the center of the optical Fourier plane is used to impart a θ -phase shift to the focused light, which serves as a so-called synthetic reference wave (SRW) for the interferometer. The output of the CPI is then the coherent superposition of the SRW and the scattered input field that results in the direct mapping of the HCB-phase into the CPI intensity output. The PCF's transmittance function is given by

$$H(f_x, f_y) = A \left(1 + (BA^{-1} \exp i\theta - 1) \text{circ} \left(\frac{f_r}{\Delta f_r} \right) \right) \quad (2)$$

where B and $A \in [0, 1]$ are transmittance factors associated with the focused and scattered light, respectively, $\theta \in [0, 2\pi]$ is the applied phase shift to the focused light within a circular region of radius Δf_r ,

(f_x, f_y) are the spatial frequency coordinates at the Fourier plane and $f_r = \sqrt{f_x^2 + f_y^2}$ [16,17]. The filter factors A, B and θ , as depicted in Fig. 2(b) can be adjusted accordingly to improve the visibility of the CPI and for maximum irradiance of the output. With an input HCB-phase described by the iris-truncated field $U(x, y) = U(r) = \text{circ}(r/r_0)e^{-il\varphi/r^0}$, the intensity at the CPI output becomes

$$I(r') = A^2 \left| U(r') + |\bar{\alpha}| (BA^{-1}(\exp i\theta) - 1) g(0) \right|^2 \quad (3)$$

where $|\bar{\alpha}|$ is the normalized Fourier zero-order of the input beam, defined as

$$\bar{\alpha} = |\bar{\alpha}| \exp i\phi_{\bar{\alpha}} = \frac{\int_0^{2\pi} \int_0^{r_0} U(r, \varphi) r dr d\varphi}{\int_0^{2\pi} \int_0^{r_0} \text{circ} \left(\frac{r}{r_0} \right) r dr d\varphi} \quad (4)$$

for integer values of l . The magnitude of $\bar{\alpha}$ determines the component of the beam that is filtered by the PCF. This parameter vanishes for an LG beam because of its dark center, and thus the CPI would fail to phase-image such a beam. The term describing the $4f$ -imaged object wave, $U(r')$, in Eq. (3) for $K = 0$ is given by

$$U(r') = \text{circ} \left(\frac{r'}{r_0} \right) \exp \left(-i \left(l\varphi \frac{r'}{r_0} + \phi_{\bar{\alpha}} \right) \right) \quad (5)$$

while the central value of the SRW-profile $g(0)$ is [26]

$$g(0) = g(r' = 0) \approx 1 - J_0(1.22\pi\eta) \quad (6)$$

The CPI can also be optimized by tailoring the SRW using the η parameter which is the ratio of the radius of the filtering region R_1 to the radius of the mainlobe of the Airy disc R_2 ,

$$\eta = \frac{R_1}{R_2} = \frac{r_0 R_1}{0.61\lambda f} \quad (7)$$

where R_2 is written in terms of the input aperture radius r_0 , illumination wavelength λ and focal length f . Normally, for a circular input aperture, the PCF is fabricated to match the radius of the corresponding Airy disc of the Fourier transform distribution. However, it is much more convenient and practical to use a high quality static filter and, if the application imposes, a specific size on the beam to be detected.

Fig. 3 shows the experimental setup for the CPI. The HCB is generated using the collimated Gaussian output of a 532-nm diode laser impinging on an SLM (Hamamatsu, 12.5 μm pixel pitch) which contains the

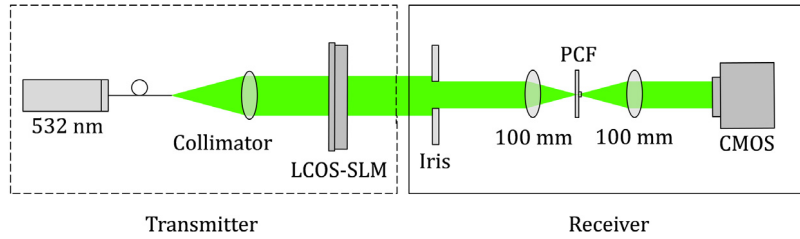


Fig. 3. Experimental setup for HCB detection. An HCB is generated using a 532-nm Gaussian beam impinging on a LCOS-SLM. The detector or receiver is composed of a CPI interferometer constructed using a 4*f* optical setup. The PCF radius is 9.8 μm.

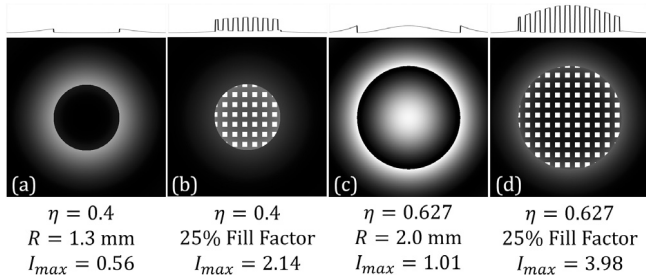


Fig. 4. Simulated CPI output for (a), (b) $\eta = 0.4$ and (c), (d) $\eta = 0.627$. The dark output in (a) is obtained when the PCF is axially aligned for a circular input aperture. $\eta = 0.627$ is chosen to achieve matched amplitude for maximum visibility. (c) is the CPI output for an input circular aperture with $\eta = 0.627$.

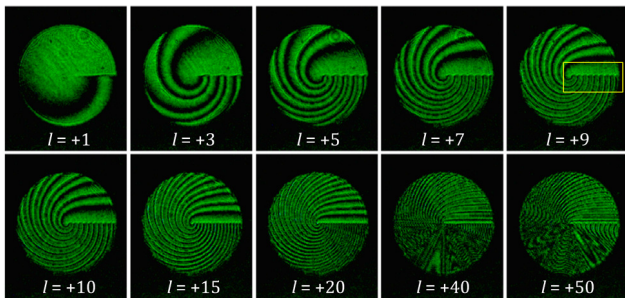


Fig. 5. Experimental HCB ($K = 0$) images from the CPI with increasing topological charge.

HCB's helical phase distribution. In actuality, the topological charge of the incoming HCB is completely unknown from the receiver. In our experiments, however, we generated HCBs with initially known topological charge to test our proposed detection scheme. The CPI is constructed using lenses with $f = 100$ mm, and its output is detected with a CMOS camera (Basler, 5.86 μm pixel size). Fig. 4 shows the CPI output for different values of η and input aperture. In the absence of an encoded phase, the axial alignment of the PCF can be calibrated so that the expected CPI-output is a dark area as shown in Fig. 4(a) [28]. With a π -phase shifting filter, this is achieved when $K = 0.5$ in Eq. (3) that corresponds to $\eta = 0.4$ and $r_0 = 1.3$ mm for a PCF radius $R_1 = 9.8$ μm. After the PCF is aligned, the input aperture radius that corresponds to optimally contrasted HCBs is $r_0 = 2.1$ mm, corresponding to $\eta = 0.627$. With this value, the Bessel function in Eq. (6) is zero, the SRW and input amplitudes are matched to consequently lead to higher maximum irradiance I_{max} and visibility $V = (I_{max} - I_{min}) / (I_{max} + I_{min})$ within the relevant region of the output intensity distribution. With the $\eta = 0.627$ condition, Fig. 4(c) shows the CPI output intensity. In theory, the central intensity value of the output when $\eta = 0.627$ is four times the input's central intensity for a 25% π -phase fill factor. Fig. 4(b) and (d) are the CPI-outputs for a checkerboard input phase pattern for $\eta = 0.4$ and $\eta = 0.627$, respectively, showing that higher maximum intensity and visibility is obtained for the latter.

Fig. 5 shows the phase-imaged HCBs for $K = 0$ and for different l 's. Visual inspection of the boxed region in the images reveals that the number of fringes directly matches the topological charge of the HCB. Given the good output visibility, it would be possible to count these fringes using image processing techniques. Scans of each interference pattern such as that in Fig. 6(a) show that the number of fringes is consistent with the charge for up to $l = 20$. It becomes a challenge, however, to determine higher l 's due to the decreased fringe visibility. This highlights the importance of the $\bar{\alpha}$ parameter in Eq. (4).

We numerically calculated the normalized zero-order of simulated HCBs and plotted it in Fig. 6(b) as a function of l . The inverse relation is verified analytically by evaluating Eq. (4) for $K = 0, l \neq 0$, leading to

$$\bar{\alpha}_{K=0} = -\frac{i}{\pi l} \tag{8}$$

Thus, from the $|\bar{\alpha}|$ in Eq. (8), the available amount of zero-order for generating a phase-shifted SRW decreases as l increases. In our current setup, the PCF is based on glass, and hence the filter parameters A and B were both ~ 1 for a near lossless phase imaging system, allowing us to simplify the expression for the intensity distribution at the output from Eq. (3) into the short form

$$I_{K=0} = 1 + \frac{4}{\pi^2 l^2} + \frac{4}{\pi l} \cos l\varphi \frac{r}{r_0} \tag{9}$$

which then leads to the following fringe visibility dependence on l :

$$V = \frac{4\pi l}{4 + \pi^2 l^2} \tag{10}$$

The expression in Eq. (9) shows the direct conversion of the HCB's phase $l\varphi/r_0$ into the CPI output intensity apart from factors that depend on l . However, as described in Eq. (10), the off-axis scattered light overpowers the SRW for higher l 's, resulting in a low fringe visibility. The simple analytic expression in Eq. (8) can lead to possible further optimization of the CPI, although this is beyond the scope of this Communication. With the use of a dynamic PCF, by using a SLM for example [29], A can be adjusted so that matched amplitude is still achieved. However, this presents a drawback in possible losses in the system and a more complex implementation. The presence of moiré fringes due to the limited resolution of the SLM and camera in this demonstration also limits the detection of HCBs with large l 's that are not addressable with the CPI parameters.

We also examined the output's dependence on the beam's helicity. Fig. 7 shows the images obtained from the CPI with $l = \pm 1, \pm 2, \pm 4, \pm 10$ and ± 15 . As described by Eq. (9), the intensity distribution of negatively charged HCB's should exhibit fringe shifting with respect to those of positively charged ones. This is indeed observed in the images acquired in our experiments. The topological charge information is also preserved in the number of fringes for negative l . Moreover, the intensity along the $\varphi = 0$ region is maximum for positive l (Fig. 7, top row) and minimum for negative l (Fig. 7, bottom row). This is expected, as described by the intensity distribution in Eq. (9), where we achieve the maximum and minimum conditions when $\varphi = 0$ for positive and negative l , respectively, independent of l and r . Hence, by observing the intensity along the $\varphi = 0$ region, we can determine the helicity of the incoming HCB.

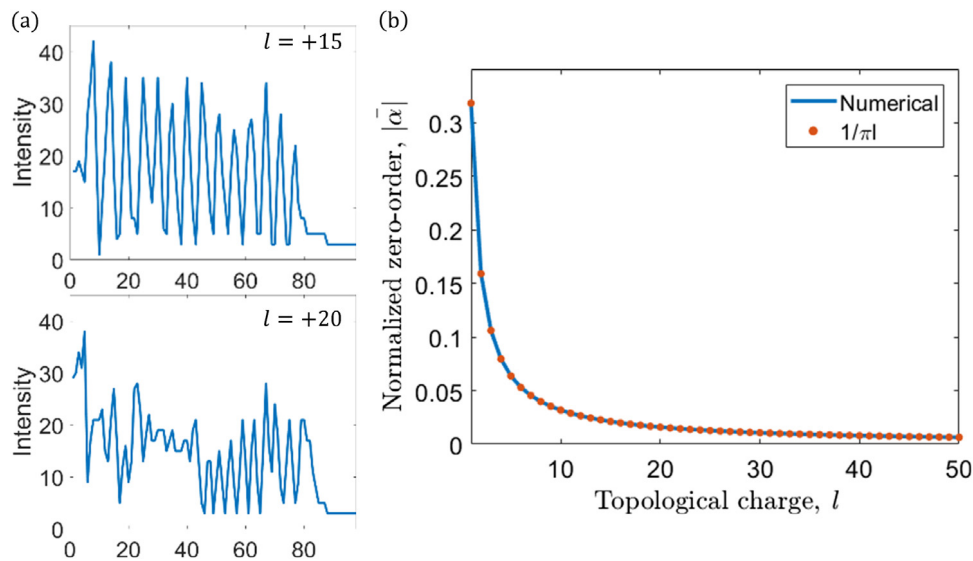


Fig. 6. (a) Intensity line scans for $l = +15$ (top), $+20$ (bottom) and (b) normalized zero-order of the HCB with increasing topological charges.

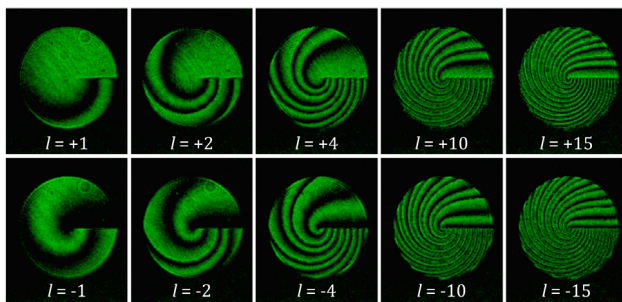


Fig. 7. (Top row) Positive and (bottom row) negatively charged HCBs ($K = 0$) acquired experimentally. A change in helicity manifests itself as a fringe shift at the output of the CPI, with maximum and minimum intensities at $\varphi = 0$ for positive and negative l , respectively.

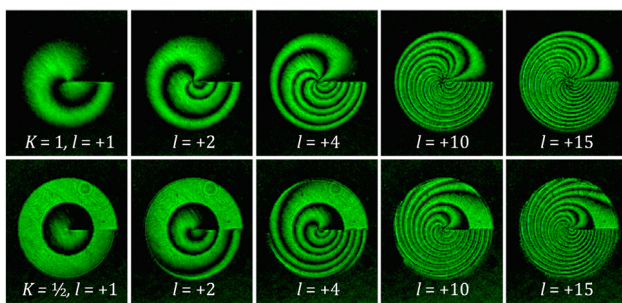


Fig. 8. Experimental CPI output for (top row) $K = 1$ and (bottom row) $K = \frac{1}{2}$.

Finally, using the same CPI-setup, we imaged HCBs with $K = 1$ and $K = \frac{1}{2}$. Fig. 8 shows the intensity distributions for select topological charges. As with the case of $K = 0$, the fringe visibility also decreases as l increases that in turn leads to the same difficulty of properly identifying the topological charge of the beam for higher orders.

In conclusion, we have demonstrated the phase imaging of OAM-carrying HCBs using a common-path interferometer that enables determination of the beam's topological charge value and its sign. The sufficient photon density around the center in the far-field intensity of HCBs facilitates the formation of a SRW that is phase-shifted by a PCF and can subsequently interfere with the scattered light of the input beam. This enables the direct mapping of the HCB-phase at the

interferometer's output intensity embodying both the charge magnitude and sign in the number and behavior of the generated interferometric fringes. Using this technique, up to $l = |20|$ can be firmly detected with our current CPI-embodiment. The limitation for higher topological charges is mainly due to the weaker fringe visibility associated with a decreasing SRW-strength for larger topological charges. This could be offset by changing the phase contrast filter parameters to achieve matched interferometric amplitudes and hence optimal interference. The phase imaging of HCBs with the use of a CPI provides a direct and robust determination of its properties. HCB properties have previously been assessed only indirectly, through the analysis of their far field intensities.

Funding

Novo Nordisk Foundation (Grand Challenge Program; NNF16OC0021948). Lundbeck Foundation (Grant number R244-2016-3941).

References

- [1] A.E. Willner, H. Huang, Y. Yan, Y. Ren, N. Ahmed, G. Xie, C. Bao, L. Li, Y. Cao, Z. Zhao, J. Wang, M.P.J. Lavery, M. Tur, S. Ramachandran, A.F. Molisch, N. Ashrafi, S. Ashrafi, Optical communications using orbital angular momentum beams, *Adv. Opt. Photon.* 7 (2015) 66–106.
- [2] C. Maurer, A. Jesacher, S. Bernet, M. Ritsch-Marte, What spatial light modulators can do for optical microscopy, *Laser Photon. Rev.* 5 (2011) 81–101.
- [3] K. Ladavac, D.G. Grier, Microoptomechanical pumps assembled and driven by holographic optical vortex arrays, *Opt. Express* 12 (2004) 1144–1149.
- [4] L. Allen, M.W. Beijersbergen, R.J.C. Spreeuw, J.P. Woerdman, Orbital angular momentum of light and the transformation of Laguerre-Gaussian laser modes, *Phys. Rev. A* 45 (1992) 8185–8189.
- [5] Q.S. Ferreira, A.J. Jesus-Silva, E.J.S. Fonseca, J.M. Hickmann, Fraunhofer diffraction of light with orbital angular momentum by a slit, *Opt. Lett.* 36 (2011) 3106–3108.
- [6] D.P. Ghai, P. Senthilkumaran, R.S. Sirohi, Single-slit diffraction of an optical beam with phase singularity, *Opt. Lasers Eng.* 47 (2009) 123–126.
- [7] M.P.J. Lavery, A. Dudley, A. Forbes, J. Courtial, M.J. Padgett, Robust interferometer for the routing of light beams carrying orbital angular momentum, *New J. Phys.* 13 (2011).
- [8] J.M. Hickmann, E.J.S. Fonseca, W.C. Soares, S. Chávez-Cerda, Unveiling a truncated optical lattice associated with a triangular aperture using light's orbital angular momentum, *Phys. Rev. Lett.* 105 (2010) 1–4.
- [9] C.-S. Guo, L.-L. Lu, H.-T. Wang, Characterizing topological charge of optical vortices by using an annular aperture, *Opt. Lett.* 34 (2009) 3686–3688.

- [10] L.A. Melo, A.J. Jesus-Silva, S. Chávez-Cerda, P.H.S. Ribeiro, W.C. Soares, Direct measurement of the topological charge in elliptical beams using diffraction by a triangular aperture, *Sci. Rep.* 8 (2018) 1–8.
- [11] D. Hebri, S. Rasouli, M. Yeganeh, Intensity-based measuring of the topological charge alteration by the diffraction of vortex beams from amplitude sinusoidal radial gratings, *J. Opt. Soc. Amer. B* 35 (2018) 724–730.
- [12] H.I. Sztul, R.R. Alfano, Double-slit interference with Laguerre-Gaussian beams, *Opt. Lett.* 31 (2006) 1–3.
- [13] D. Jianji, Z. Hailong, Z. Xinliang, Dynamic interferometry measurement of orbital angular momentum of light, *Opt. Lett.* 39 (2014) 7.
- [14] S. Slussarenko, V. D'Ambrosio, B. Piccirillo, L. Marrucci, E. Santamato, The Polarizing Sagnac Interferometer: a tool for light orbital angular momentum sorting and spin-orbit photon processing, *Opt. Express* 18 (2010) 27205–27216.
- [15] A. D'Errico, R. D'Amelio, B. Piccirillo, F. Cardano, L. Marrucci, Measuring the complex orbital angular momentum spectrum and spatial mode decomposition of structured light beams, *Optica* 4 (2017) 1350–1357.
- [16] S. Zheng, J. Wang, Measuring orbital angular momentum (OAM) states of vortex beams with annular gratings, *Sci. Rep.* 7 (2017) 40781.
- [17] Z. Liu, S. Gao, W. Xiao, J. Yang, X. Huang, Y. Feng, J. Li, W. Liu, Z. Li, Measuring high-order optical orbital angular momentum with a hyperbolic gradually changing period pure-phase grating, *Opt. Lett.* 43 (2018) 3076–3079.
- [18] C.A. Alonzo, P.J. Rodrigo, J. Glückstad, Helico-conical optical beams: a product of helical and conical phase fronts, *Opt. Express* 13 (2005) 1749–1760.
- [19] G. Overton, J. Glückstad, Phase functions are inseparable in helico-conical optical beams, *Laser Focus World* (2005).
- [20] V.R. Daria, D.Z. Palima, J. Glückstad, Optical twists in phase and amplitude, *Opt. Express* 19 (2011) 476–481.
- [21] T. Latychevskaia, H.W. Fink, Inverted Gabor holography principle for tailoring arbitrary shaped three-dimensional beams, *Sci. Rep.* 6 (2016) 26312.
- [22] N.P. Hermosa, C.O. Manaois, Phase structure of helico-conical optical beams, *Opt. Commun.* 271 (2007) 178–183.
- [23] Y. Zhang, X. Yang, J. Gao, Twisting phase and intensity of light with plasmonic metasurfaces, *Sci. Rep.* 8 (2018) 4884.
- [24] N. Bareza, N. Hermosa, Propagation dynamics of vortices in helico-conical optical beams, *Opt. Commun.* 356 (2015) 236–242.
- [25] N. Hermosa, C. Rosales-Guzmán, J.P. Torres, Helico-conical optical beams self-heal, *Opt. Lett.* 38 (2013) 383.
- [26] J. Glückstad, P.C. Mogensén, Optimal phase contrast in common-path interferometry, *Appl. Opt.* 40 (2001) 268–282.
- [27] P.J. Rodrigo, D. Palima, J. Glückstad, Accurate quantitative phase imaging using generalized phase contrast, *Opt. Express* 16 (2008) 2498–2509.
- [28] M.J. Villangca, A.R. Bañas, D. Palima, J. Glückstad, Dark GPC: extended nodal beam areas from binary-only phase, *Opt. Eng.* 55 (2016) 125102.
- [29] F. Kenny, F.S. Choi, J. Glückstad, M.J. Booth, Adaptive optimisation of a generalised phase contrast beam shaping system, *Opt. Commun.* 342 (2015) 109–114.

